

The G^0 Experiment
Backward Angle Measurements
Update

The G^0 Collaboration

California Institute of Technology, Carnegie-Mellon University, College of William and Mary, Grinnell College, Hampton University, L'Institut de Physique Nucléaire d'Orsay, Laboratoire de Physique Subatomique et de Cosmologie Grenoble, Louisiana Tech. University, New Mexico State University, Thomas Jefferson National Laboratory, TRIUMF, University of Illinois at Urbana-Champaign, University of Kentucky, University of Manitoba, University of Maryland, University of Northern British Columbia, University of Winnipeg, Virginia Tech, and Yerevan Physics Institute

June 2005

Contents

1	Summary	1
2	Physics	6
2.1	Nucleon Vector Form Factors and Strangeness Content	7
2.2	Anapole form factor	11
2.3	Other experiments: past and future	13
3	Experiment	16
3.1	Introduction and Kinematics	16
3.2	Deuterium corrections	17
3.3	Particle identification requirements	18
3.3.1	Calculation of π^- Cross Sections	19
3.3.2	Measurement of π^- Rate at Backward Angles	19
3.3.3	Pion Rates and Contaminations	20
3.3.4	Rejection of π^- Background	24
4	Apparatus	26
4.1	Detectors	26
4.1.1	FPDs	26
4.1.2	CEDs	26
4.1.3	Aerogel Cherenkov	28
4.1.4	Drift Chambers	31
4.2	Electronics	32
4.3	DAQ	41
4.4	Target	43
4.5	Infrastructure	46
5	Organization and Schedule	48

6	Expected Results and Beam Time Request	49
6.1	Expected Results	49
6.2	Beam Time Request	49
7	Appendix A: G0 Forward Angle Preprint (nucl-ex/0506021)	60
8	Appendix B: G0 Forward Angle Run Summary	61

1 Summary

This submission regarding the G^0 experiment has been prepared for consideration by the Jefferson Lab Program Advisory Committee at its PAC28 meeting. The G^0 experiment has been approved previously at five PAC meetings (as 91-017 in December 1993, 99-016 in January 1999, 00-006 in January 2000, 01-116 in July 2001 and 04-115 in July 2004); these approvals have covered the experiment commissioning, the forward angle running and approval for the first backward angle measurement ($Q^2 = 0.8 \text{ GeV}^2$, 799 MeV incident energy, scheduled to start Dec. 3, 2005). *In the present proposal we request approval to complete the set of G^0 backward angle measurements originally proposed with two runs at lower energies, including the possibility of running in a single user mode in Summer 2006.* We believe these measurements are well-motivated by the exciting results from the forward angle measurement which indicate non-zero values for both G_M^s and G_E^s over a range of momentum transfers. The scheduled and proposed backward angle measurements would complete the presently emerging picture of these two contributions to the nucleon form factors and provide a clear challenge to nucleon calculations and models for some time to come.

In the G^0 experiment, parity-violating asymmetries in elastic electron scattering from the nucleon is measured at both forward and backward angles and over a range of momentum transfers from 0.12 – 1.0 GeV^2 . The primary purpose of the experiment is to separate the s quark contributions, $G_E^s(Q^2)$ and $G_M^s(Q^2)$, to the overall charge and magnetization densities of the nucleon using these measurements. No other existing or proposed experiment will perform the separation over this range of momentum transfers.

The forward angle measurements have been completed and a paper submitted to Physical Review Letters for publication [1] (see Appendix A). There are a number of important conclusions from this work. First, the measurements are consistent with the two HAPPEX hydrogen measurements [2, 3] made in similar kinematics as shown in Fig. 1.1. Second, the hypothesis that $G_E^s + \eta G_M^s = 0$ is disfavored at about the 90% CL including all uncertainties. Third, the combination of the five experiments: SAMPLE [4], PVA4 [5], HAPPEX hydrogen [3], HAPPEX helium [6] and G^0 [1] at $Q^2 = 0.1 \text{ GeV}^2$ (Fig. 1.2) yields the values $G_E^s = -0.013 \pm 0.028$ and $G_M^s = 0.62 \pm 0.31$ at 1-sigma. To get a feeling for the scale of this result, we note that if G_M^s follows a standard dipole form factor, its value at $Q^2 = 0$ is about 0.8, or (accounting for the factor of $-1/3$ in the definition) about 60% of the isoscalar nucleon form factor (and with the opposite sign). Fourth, and most important for guiding the backward angle measurements, the G^0 results also suggest something about G_E^s . Because $\eta \sim 0.94Q^2$ for the forward G^0 kinematics, in order for the combination $G_E^s + \eta G_M^s$ to *decrease* beyond Q^2 of about 0.15, G_E^s must be negative (see Fig. 1.1). This suggests that a very interesting place to measure at backward angle is in the region where $G_E^s + \eta G_M^s \sim 0$ near $Q^2 \cong 0.23 \text{ GeV}^2$ where there would also be forward G^0 and

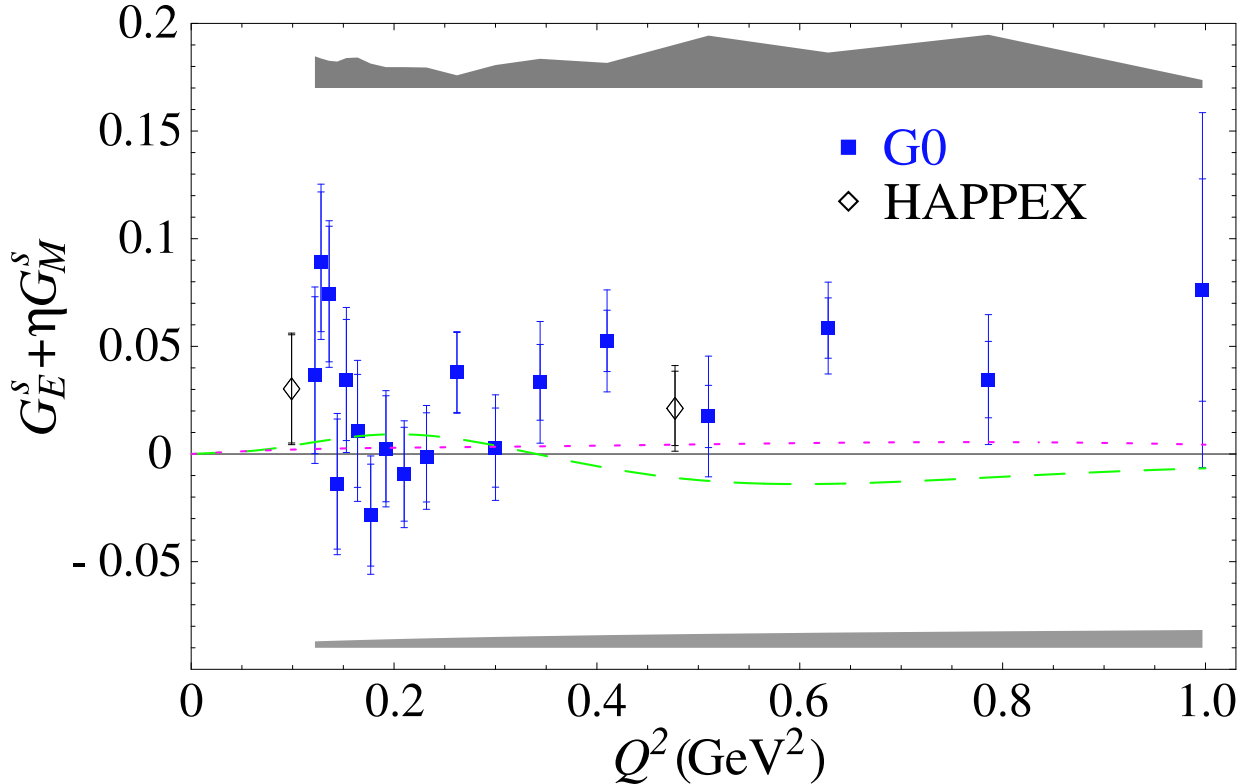


Figure 1.1: The quantity $G_E^s + \eta G_M^s$ measured in the forward angle G0 experiment. Error bars correspond to the statistical (inner) and statistical plus point-to-point systematic uncertainties added in quadrature (outer). The bands represent the global uncertainties: experimental (upper) and model (lower). The agreement with the HAPPEX hydrogen measurements is excellent. The curves correspond to different choices for the electromagnetic nucleon form factors (Kelly [8] standard). The long-dashed curve uses the form factors of Friedrich and Walcher [9] and the short-dashed curve uses the “Rosenbluth” form factors of Arrington [10] for the proton and the Kelly form factors for the neutron. The curves are interpreted as follows: e.g., for $Q^2 = 0.63 \text{ GeV}^2$, the point would move from $G_E^s + \eta G_M^s = 0.059$ to 0.072 for the Friedrich and Walcher case.

PVA4 [7] data. We propose this as the second backward angle kinematic point for the G0 experiment, with a measurement at $Q^2 = 0.477$ (the original HAPPEX Q^2) to follow.

A special purpose, superconducting toroidal spectrometer with large, azimuthally symmetric angular acceptance and an associated cryogenic target have been used for these measurements. There was excellent performance from both the experimental equipment and the various accelerator systems during the forward angle measurement (see Table 1.1 for the collaboration list). Key details regarding the forward angle measurement are included in a summary in Appendix B.

There will be a few changes in these components for running at backward angles. Most importantly, we have concluded that there are significant practical and experimental advantages to running with a standard 499 MHz bunch structure, rather than the 31 MHz

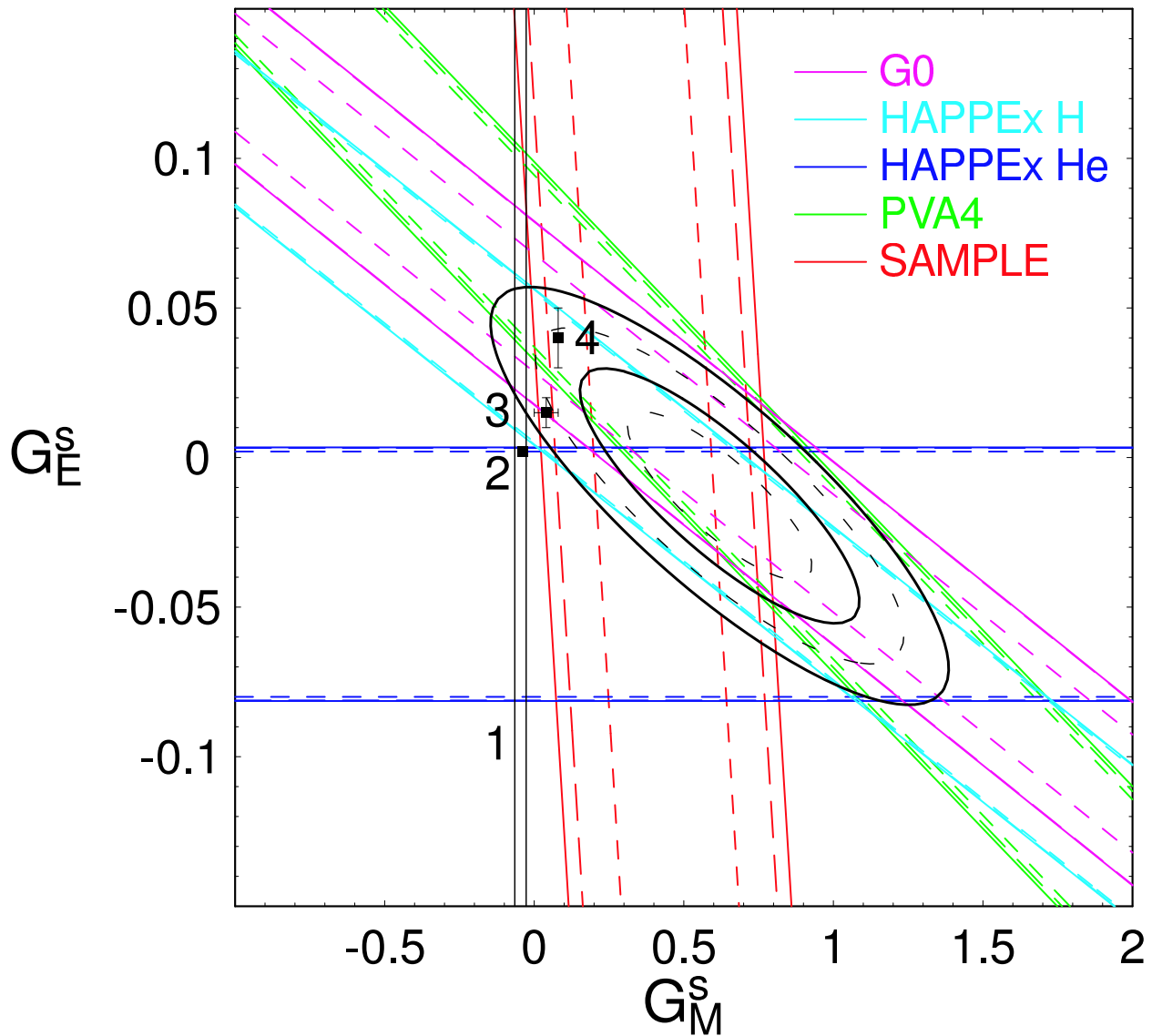


Figure 1.2: World data for $Q^2 = 0.1 \text{ GeV}^2$. The inner and outer *dashed* contours give the one- and two-sigma bounds; e.g., the projection of the dashed contour on the G_M^s axis gives the uncertainty for indeterminate G_E^s . The solid contours give the 68.3 and 95.5% CL regions (see Section 32.3.2.3 of PDG [12]). The theory points are from some relatively recent calculations: 1 (band) - Leinweber, et al [11], 2 - Lyubovitskij, et al. [13], 3 - Lewis, et al. [14] and 4 - Silva, et al. [15].

structure used for the forward angle measurement. Because the backward angle experiment does not require t.o.f., we have modified our plan for the electronics to use a standard trigger generated by our detectors, rather than using the beam pickoff method used for the forward running. This will allow us to use the 499 MHz structure and still have less dead-time than in the forward measurement (the rates in the backward measurement are much lower). In addition, we expect that use of the 499 MHz structure will allow us to run higher beam currents and reduce the statistical uncertainty in the back angle measurements that dominate our overall uncertainty in extraction of G_E^s , G_M^s and G_A^e . Based on the target boiling and overall cooling power studies performed during the forward measurement, we expect to be able to run with a beam current of at least 80 μA . Separation of elastic and inelastic electrons in the backward angle experiment requires a new set of scintillator detectors to be placed near the spectrometer exit windows (see Section 4.1.2). Running with a deuterium target necessitates particle identification measurements to discriminate between pions and electrons. For this purpose we are adding a Cherenkov detector, to be discussed in detail in Sections 3.3 and 4.1.3. We have also incorporated recording of pion events in order to measure their asymmetries. Otherwise, especially in terms of the standard false asymmetries, the forward and backward angle measurements are essentially the same (asymmetries are larger in the backward direction).

With this submission, we propose the measurements to complete the original G0 experimental program, i.e. backward angle runs at momentum transfers of $Q^2 = 0.23, 0.48 \text{ GeV}^2$. If there are ~ 12 calendar weeks (equivalent to 50 beam days at 60% efficiency) of low-energy running available in summer 2006, we propose the following strategy: if the extraction of G_A^e from the 799 MeV run ($Q^2 = 0.80 \text{ GeV}^2$, starting Dec. 2005) yields a value consistent with the Zhu, et al. [58] and a simple dipole falloff (characterized by $M_A = 1.0 \text{ GeV}^2$), we would run with the hydrogen target for the entire period (at $E = 360 \text{ MeV}$, $Q^2 = 0.23 \text{ GeV}^2$) to obtain the smallest possible uncertainty in G_M^s and G_E^s . If the extraction of G_A^e at the higher momentum transfer yields a different result, we propose running the hydrogen target for 30 beam days and the deuterium target for 20. We propose completion of this program with a run at 585 MeV ($Q^2 = 0.48 \text{ GeV}^2$) where the division of the time would again depend on the combined physics outcome of the forward and first backward angle measurements.

California Institute of Technology				
R. Carr	S. D. Covrig ^f	K. Gustafsson ^{f*}	L. Hannelius	R. D. McKeown [†]
M. J. Ramsey-Musolf*				
Carnegie-Mellon University				
A. Biselli	G. Franklin	J. Kuhn	J. Lachniet ^f	B. Quinn [†]
College of William and Mary				
D. S. Armstrong [†]	T. D. Averett	S. Bailey	J. M. Finn	K. A. Griffioen
K. Grimm	B. Moffit	S. Phillips ^f	J. Secrest ^f	A. Slaughter ^f
V. Sulkosky ^f				
Grinnell College				
D. T. Spayde [†]				
IPN Orsay				
J. Arvieux [†]	L. Bimbot	E. Boukobza ^f	H. Guler ^{f*}	J. Lenoble ^f
B. Loupias ^f	D. Marchand ^f	M. Morlet ^{f*}	J. van de Wiele ^f	
LPSC Grenoble				
G. Batigne ^f	C. Furget	B. Guillon ^f	S. Kox [†]	E. Liatard ^{f*}
F. Merchez ^f	P. Pillot ^b	G. Quemener ^f	J. Real	R. Tieulent ^{f*}
E. Voutier				
Louisiana Tech. Univ.				
T. A. Forest	K. Johnston	J. S. Kraft	M. Novovic ^f	N. Simicevic
S. Wells [†]				
New Mexico State University				
G. MacLachlan	D. McKee ^f	V. Papavassiliou [†]	S. Pate [†]	A. W. Rauf ^f
TJNAF				
J. Benesch*	P. Bosted	A. Bruell ^b	R. D. Carlini	Y. Chao*
S. Chattopadhyay*	V. Dharmawardane ^b	D. Gaskell	J. Grames*	J. Hansknecht*
M. Jones	R. Kazimi*	A. Lung	M. Poelker*	J. Roche
G. Smith [†]	W. F. Vulcan	G. Warren ^f	S. A. Wood	
TRIUMF				
C. A. Davis [†]				
University of Illinois				
D. H. Beck [†]	P. Kammel	P. M. King	M. Muether ^b	K. Nakahara ^f
R. Neveling ^f	S. Williamson [†]			
University of Kentucky				
D. Dale	A. Kolarkar	W. Korsch [†]	I. Nakagawa ^f	
University of Manitoba				
J. Birchall	W. R. Falk	M. T. Gericke ^b	L. Lee	S. A. Page
W. D. Ramsay	G. A. Rutledge	W. T. H. van Oers [†]		
University of Maryland				
E. J. Beise [†]	F. Benmokhtar ^b	H. Breuer	C. Ellis ^b	T. Horn
J. Liu ^f	P. Roos			
University of Massachusetts				
B. R. Holstein ^{†*}				
University of Northern British Columbia				
E. Korkmaz [†]	T. Porcelli			
University of Winnipeg				
J. Martin [†]				
Virginia Tech				
J. Mammei ^b	M. L. Pitt [†]	R. Suleiman ^b		
Yerevan Physics Institute				
R. Asaturyan	H. Mkrtchyan [†]	T. Navasardyan	V. Tadevosyan	

Table 1.1: Active participants in the G^0 collaboration ([†] indicates a contact person, * indicates one who does not take shifts, f indicates participation in forward angle measurements only, b indicates participation in backward angle measurements only).

2 Physics

The parity-violating interaction between electrons and nucleons involves interference between the dominant electromagnetic (γ exchange) and neutral weak (Z^0 exchange) interactions. Due to the parity-violating nature of the weak interaction, these interference effects imply the existence of small pseudoscalar observables in electron scattering experiments. Much of the discussion in this section is elaborated upon in recent reviews [16, 17, 18].

One generally measures the ratio of helicity dependent to helicity independent cross sections, or the parity-violating asymmetry:

$$A = \frac{d\sigma_R - d\sigma_L}{d\sigma_R + d\sigma_L} \quad (2.1)$$

where σ_R and σ_L are the cross sections for right- and left-handed electrons, respectively. This quantity will be proportional to a product of neutral weak couplings $v^Z \cdot a^Z$ that contains the physics of interest. Thus, measurement of the helicity dependence in elastic electron-proton scattering can be used to study the neutral weak vector form factors of the nucleon [19, 20, 21]. There is also sensitivity to the weak axial vector form factors; these are suppressed at leading order but are also of great interest and should be measured.

The parity-violating asymmetry for elastic electron-proton scattering is given by the following expression [22]:

$$A = \left[\frac{-G_F Q^2}{4\sqrt{2}\pi\alpha} \right] \frac{\varepsilon G_E^\gamma G_E^Z + \tau G_M^\gamma G_M^Z - (1 - 4\sin^2\theta_W)\varepsilon' G_M^\gamma G_A^e}{\varepsilon(G_E^\gamma)^2 + \tau(G_M^\gamma)^2} \quad (2.2)$$

$$\equiv -\frac{G_F Q^2}{4\sqrt{2}\pi\alpha} \times \frac{\mathcal{N}}{\mathcal{D}} \quad (2.3)$$

where

$$\begin{aligned} \tau &= \frac{Q^2}{4M_N^2} \\ \varepsilon &= \frac{1}{1 + 2(1 + \tau)\tan^2\frac{\theta}{2}} \\ \varepsilon' &= \sqrt{\tau(1 + \tau)(1 - \varepsilon^2)} \end{aligned} \quad (2.4)$$

are kinematic quantities, $Q^2 > 0$ is the four-momentum transfer, and θ is the laboratory electron scattering angle.

The quantities G_E^γ , G_M^γ , G_E^Z , and G_M^Z are the vector form factors of the nucleon associated with γ - and Z -exchange. The electromagnetic and weak form factors are (in lowest order) related via the flavor dependence of the fundamental Z - q couplings. The flavor structure of these form factors and the radiative corrections are considered in more detail below.

The neutral weak e - N interaction also involves an axial vector coupling G_A^e in the third term of the numerator in Eqn.(2.2). The tree-level Z -exchange process is responsible for the $1 - 4 \sin^2 \theta_W$ factor (proportional to the neutral weak *vector* charge of the electron) that appears in this expression and, as noted in [22, 23], higher order processes can contribute significantly. These include interesting anapole effects and other electroweak radiative corrections as discussed below.

It is important to note that the three terms in the numerator can be separately determined via a series of measurements. At very small scattering angles (and low momentum transfer), the G_E term has its maximum contribution due to the large value of ϵ . This is the focus of the recently completed G0, PVA4 and HAPPEX forward angle measurements. At larger scattering angles, one is sensitive to a combination of both the G_M^Z term and the G_A^e (axial) term. Although one expects the G_M^Z term to be dominant, the axial term can not be neglected, and indeed it is of great interest to study this term as well. Separation of these terms via kinematic measurements on the proton is extremely difficult. The best method to separate the magnetic and axial terms is to utilize quasielastic scattering from deuterium.

For a nucleus with Z protons and N neutrons the quasielastic asymmetry can be written in the simple form (ignoring final state interactions and other nuclear corrections):

$$A_{\text{nuc}} = -\frac{G_F Q^2}{4\sqrt{2}\pi\alpha} \times \frac{N\mathcal{N}_n + Z\mathcal{N}_p}{N\mathcal{D}_n + Z\mathcal{D}_p} \quad (2.5)$$

where \mathcal{N}_p (\mathcal{N}_n) is the numerator expression and \mathcal{D}_p (\mathcal{D}_n) the denominator (from Eqns. 2.2 and 2.3) for the proton (neutron), respectively. Effects associated with the deuteron wavefunction and different potential models have been explored in [24] and shown to be quite small. Of course, the corrections for final state interactions and exchange currents must be made to enable reliable separation of the axial and magnetic form factors and the theory of these effects is now thought to be under control. These issues have been addressed in recent work by Diaconescu, *et al.*[25] and Liu, *et al.*[26]. Experimental validation has been provided by the SAMPLE experiment in deuterium measurements at two low values of momentum transfer [27].

In order to determine G_E^s , G_M^s , and G_A^e it is necessary to perform at least 3 independent measurements at each Q^2 . The G0 program is a unique opportunity to perform a series of such measurements: the forward angle measurement on the proton, a backward angle measurement on the proton, and also a backward angle measurement of the quasielastic deuteron asymmetry.

2.1 Nucleon Vector Form Factors and Strangeness Content

The standard electroweak model couplings to the up, down, and strange quarks imply that the electromagnetic current operator has the simple familiar form

$$\hat{V}_\gamma^\mu = \frac{2}{3}\bar{u}\gamma^\mu u - \frac{1}{3}\bar{d}\gamma^\mu d - \frac{1}{3}\bar{s}\gamma^\mu s. \quad (2.6)$$

Similarly, the neutral weak vector current operator is given by the expression

$$\hat{V}_Z^\mu = (1 - \frac{8}{3} \sin^2 \theta_W) \bar{u} \gamma^\mu u + (-1 + \frac{4}{3} \sin^2 \theta_W) \bar{d} \gamma^\mu d + (-1 + \frac{4}{3} \sin^2 \theta_W) \bar{s} \gamma^\mu s. \quad (2.7)$$

Here the coefficients depend on the weak mixing angle, which is very accurately known ($\sin^2 \theta_W = 0.23120 \pm 0.00015$ [28]). The flavor structure contained in these expressions forms the basis for a program to measure the flavor composition of the vector form factors. The measurements involve matrix elements of these operators (the form factors) which will reflect their underlying flavor dependence.

The electromagnetic form factors of the nucleon arise from matrix elements of the EM current operator

$$\langle N | \hat{V}_\gamma^\mu | N \rangle \equiv \bar{u}_N \left[F_1^\gamma(q^2) \gamma^\mu + \frac{i}{2M_N} F_2^\gamma(q^2) \sigma^{\mu\nu} q_\nu \right] u_N \quad (2.8)$$

where $F_1^\gamma(q^2)$ and $F_2^\gamma(q^2)$ are the Dirac and Pauli electromagnetic form factors, which are functions of the squared momentum transfer. We will also use the Sachs form factors, which are linear combinations of the Dirac and Pauli form factors

$$\begin{aligned} G_E &= F_1 - \tau F_2 \\ G_M &= F_1 + F_2 \end{aligned} \quad (2.9)$$

where $\tau \equiv -q^2/4M_N^2 > 0$.

The quark flavor structure of these form factors can be revealed by writing the matrix elements of individual quark currents in terms of form factors:

$$\langle N | \bar{q}^j \gamma^\mu q^j | N \rangle \equiv \bar{u}_N \left[F_1^j(q^2) \gamma^\mu + \frac{i}{2M_N} F_2^j(q^2) \sigma^{\mu\nu} q_\nu \right] u_N \quad (2.10)$$

where $j = u, d$, or s ; this defines the form factors F_1^j and F_2^j . Then using definitions analogous to Eqn. (2.9), we can write

$$G_E^\gamma = \frac{2}{3} G_E^u - \frac{1}{3} G_E^d - \frac{1}{3} G_E^s \quad (2.11)$$

$$G_M^\gamma = \frac{2}{3} G_M^u - \frac{1}{3} G_M^d - \frac{1}{3} G_M^s. \quad (2.12)$$

In direct analogy to Eqn. (2.7), we have expressions for the neutral weak form factors G_E^Z and G_M^Z in terms of the different quark flavor components:

$$G_{E,M}^Z = (1 - \frac{8}{3} \sin^2 \theta_W) G_{E,M}^u + (-1 + \frac{4}{3} \sin^2 \theta_W) G_{E,M}^d + (-1 + \frac{4}{3} \sin^2 \theta_W) G_{E,M}^s. \quad (2.13)$$

Again it is important to emphasize that the form factors $G_{E,M}^{u,d,s}$ appearing in this expression are *exactly* the same as those in the electromagnetic form factors in Eqns. (2.11, 2.12).

Utilizing charge symmetry, one then can eliminate the up and down quark contributions to the neutral weak form factors using the proton and neutron electromagnetic form factors and obtain the expressions

$$G_{E,M}^{Z,p} = (1 - 4 \sin^2 \theta_W) G_{E,M}^{\gamma,p} - G_{E,M}^{\gamma,n} - G_{E,M}^s. \quad (2.14)$$

This is a key result. It shows how the neutral weak form factors are related to the electromagnetic form factors plus a contribution from the strange (electric or magnetic) form factor. Thus measurement of the neutral weak form factor will allow (after combination with the electromagnetic form factors) determination of the strange form factor of interest.

The electromagnetic form factors present in Eqns. (2.11,2.12) are very accurately known (1-2 %) for the proton in the momentum transfer region $Q^2 < 1$ (GeV/c)². The neutron form factors are not known as accurately as the proton form factors, but a good deal of progress has been made recently and more experimental results are expected soon [29]. The improving knowledge of the neutron form factors will not significantly hinder the interpretation of the neutral weak form factors.

In obtaining Eqn. (2.14), it was assumed that charge symmetry was exact. Electromagnetic and quark mass effects can cause small violations of charge symmetry and introduce corrections to this relation. The effects of charge symmetry violation on the extraction of strange form factors from neutral weak and electromagnetic form factors has been treated in some detail in [30]. In that work it is found that these corrections are very small, generally less than about 1% of the electromagnetic form factors, and have only a minor effect on the extraction of the strange form factors.

As mentioned above, there are electroweak radiative corrections to the coefficients in Eqn. (2.14) due to processes such as those shown in Figure 2.1. The above expressions for the neutral weak vector form factors $G_{p,n}^Z$ in terms of the electromagnetic form factors $G_{p,n}^\gamma$ are modified according to

$$G_{E,M}^{Z,p} = (1 - 4 \sin^2 \theta_W)(1 + R_V^p)G_{E,M}^{\gamma,p} - (1 + R_V^n)G_{E,M}^{\gamma,n} - G_{E,M}^s. \quad (2.15)$$

The correction factors have been computed [31, 23, 22] to be

$$\begin{aligned} R_V^p &= -0.045 \pm 0.033 \\ R_V^n &= -0.0118 \pm 0.0004. \end{aligned} \quad (2.16)$$

The properties of the strange form factors G_E^s and G_M^s near $Q^2 = 0$ are of particular interest in that they represent static properties of the nucleon. Thus it is customary to define the quantity

$$\mu_s \equiv G_M^s(Q^2 = 0) \quad (2.17)$$

as the strange magnetic moment of the nucleon. Since the nucleon has no net strangeness, we find $G_E^s(Q^2 = 0) = 0$. However, one can express the slope of G_E^s at $Q^2 = 0$ in the usual fashion in terms of a ‘‘strangeness radius’’ r_s

$$r_s^2 \equiv -6 \left[dG_E^s/dQ^2 \right]_{Q^2=0}. \quad (2.18)$$

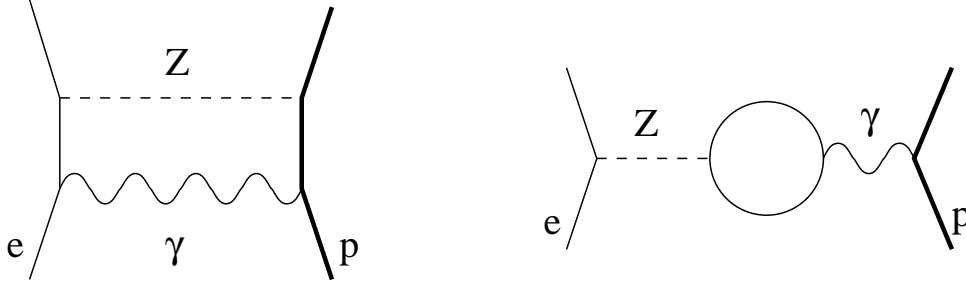


Figure 2.1: Examples of amplitudes contributing to electroweak radiative corrections (“ $\gamma - Z$ box” on the left) and anapole corrections (“ $\gamma - Z$ mixing” on the right).

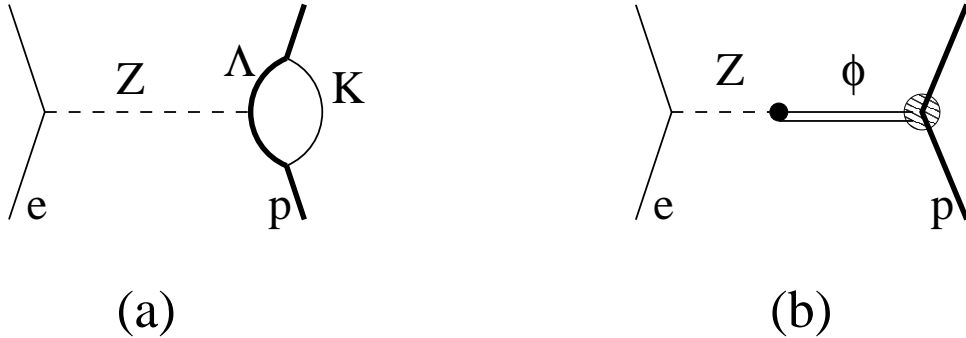


Figure 2.2: Examples of (a) loop and (b) pole diagrams used to compute strangeness effects in the nucleon.

A variety of theoretical methods have been employed in efforts to compute the form factors $G_{E,M}^s(Q^2)$ (or often just the quantities μ_s and r_s). Figure 2.2 shows two examples of physical processes that may contribute. These are generically known as “loop” effects and “pole” effects. The loop effects [32, 33, 34, 35, 36] correspond to the fluctuation of the nucleon into a K -meson and hyperon. The physical separation of the s and \bar{s} in such processes (or the production of $s\bar{s}$ in a spin singlet) leads to non-zero values of $G_{E,M}^s(Q^2)$. The pole processes [38, 39, 40] are associated with the fluctuation of the virtual boson (photon or Z) into a ϕ meson, which is predominantly an $\bar{s}s$ pair. Some attempts have been made to combine the two approaches using dispersion theoretical analyses [41]. Other models employ SU(3) extensions of the Skyrme model [42, 43, 44, 45] or the Nambu-Jona-Lasinio model. [49] Excited hyperons and strange mesons are also included in some treatments, and these contributions seem to be numerically significant. [36, 37] A detailed review of the various calculations can be found in Ref. [50].

A reasonably complete compilation of theoretical results for μ_s and r_s^2 is listed in Table 2.1. The calculated values of r_s^2 are small and there is no general agreement on the sign. However, there is evidently a trend in Table 2.1 that one should have expected $\mu_s < 0$, generally in the range $-0.8 \rightarrow 0.0$ nuclear magnetons. Notable exceptions are references [43] and [45] which analyze the set of baryon magnetic moments in the context of a SU(3) generalization of the Skyrme model Hamiltonian. The indications from the combination of the $Q^2 = 0.1$ GeV² measurements shown in Fig. 1.2 are that $\mu_s \sim +0.8$.

Table 2.1: Theoretical predictions for $\mu_s \equiv G_M^s(Q^2 = 0)$ and r_s^2 .

Type of calculation	μ_s (n.m.)	$r_s^2(\text{fm}^2)$	Reference
Poles	-0.31 ± 0.09	$0.11 \rightarrow 0.22$	[38]
Kaon Loops	$-0.31 \rightarrow -0.40$	$-0.032 \rightarrow -0.027$	[32]
Kaon Loops	-0.026	-0.01	[33]
Kaon Loops	$ \mu_s = 0.8$		[34]
SU(3) Skyrme (broken)	-0.13	-0.10	[42]
SU(3) Skyrme (symmetric)	-0.33	-0.19	[42]
SU(3) chiral hyperbag	$+0.42$		[43]
SU(3) chiral color dielectric	$-0.20 \rightarrow -0.026$	-0.003 ± 0.002	[51]
SU(3) chiral soliton	-0.45	-0.35	[44]
Poles	-0.24 ± 0.03	0.19 ± 0.03	[39]
Kaon Loops	$-0.125 \rightarrow -0.146$	$-0.022 \rightarrow -0.019$	[35]
NJL soliton	$-0.05 \rightarrow +0.25$	$-0.25 \rightarrow -0.15$	[49]
QCD equalities	-0.75 ± 0.30		[52]
Loops	$+0.035$	-0.04	[36]
Loops	-0.06	$+0.02$	[37]
Dispersion	$-0.10 \rightarrow -0.14$	$0.21 \rightarrow 0.27$	[41]
Chiral models	$-0.25, -0.09$	0.24	[53]
Poles	0.003	0.002	[40]
SU(3) Skyrme (broken)	$+0.36$		[45]
Lattice (quenched)	-0.36 ± 0.20	$-0.06 \rightarrow -0.16$	[46]
Lattice	0.04 ± 0.04	0.015 ± 0.005	[14]
Lattice (chiral)	-0.16 ± 0.18		[47]
Chiral quark	-0.04	0.002	[13]
Quark soliton	0.08 ± 0.01	0.04 ± 0.01	[15]
Lattice	-0.046 ± 0.019		[11]

2.2 Anapole form factor

As noted above, the parity-violating interaction of electrons with nucleons involves an axial vector coupling to the nucleon, G_A^e . This term in the parity-violating asymmetry contains several effects beyond the leading order Z -exchange which can only be differentiated in theoretical calculations (if at all). Nevertheless, it is important to establish that the *experimentally observable* quantities are well-defined and unambiguous.

In parity-violating electron scattering the neutral weak axial form factor corresponding to tree-level Z -exchange is multiplied by the coefficient $1 - 4 \sin^2 \theta_W \ll 1$. This suppression of the leading amplitude increases the importance of anapole effects and other electroweak radiative corrections

$$G_A^e = G_A^Z + \eta F_A + R_e \quad (2.19)$$

where

$$\eta = \frac{8\pi\sqrt{2}\alpha}{1 - 4 \sin^2 \theta_W} = 3.45, \quad (2.20)$$

$G_A^Z = G_A \tau_3 + \Delta s$, F_A is the nucleon anapole form factor (defined below), and R_e are radiative corrections. The normalization of $G_A \tau_3$ is obtained from neutron beta decay and its Q^2 dependence from charged current neutrino scattering; Δs is estimated from spin dependent deep inelastic scattering. G_A^Z is therefore completely determined by experiments independent of the present one. Typical contributions to R_e and F_A are shown in Figure 2.1. As discussed in [22, 23], the separation of F_A and R_e is actually a theoretical issue and dependent upon the choice of gauge. In calculations performed to date [31, 54] the anapole type effects associated with the “ $\gamma - Z$ mixing” amplitudes are, in fact, the dominant correction. We thus refer to the observable difference between G_A^e and G_A^Z as an anapole contribution, with the caveat that the complete set of radiative corrections must be included in any consistent quantitative theoretical treatment of G_A^e .

The anapole moment has been traditionally defined as the effective parity-violating coupling between real photons and nucleons [55]. (In practice, this quantity is only observable at finite momentum transfer associated with the parity-violating interaction between electrons and nucleons.) It appears as an additional term in Eqn. (2.8) when one includes the possibility that parity is not strictly conserved [54]:

$$\begin{aligned} \langle N | \hat{V}_\gamma^\mu | N \rangle &\equiv \bar{u}_N(p') \left\{ F_1 \gamma^\mu + \frac{i}{2M_N} F_2 \sigma^{\mu\nu} q_\nu \right. \\ &\quad \left. + F_A [G_F(q^2 \gamma^\mu - q^\nu \gamma_\nu q^\mu) \gamma^5] \right\} u(p) \end{aligned} \quad (2.21)$$

Note that our definition of F_A differs from that used in the atomic physics literature by a factor of $M_N^2 G_F$ with the result that the natural scale of F_A is of order unity. Thus, F_A could indeed provide a substantial contribution to G_A^e (see Eqn. (2.19)).

As mentioned above, aside from the leading Z exchange term (G_A^Z), the dominant calculated contribution to G_A^e arises from the “ $\gamma - Z$ mixing” diagram shown in Figure 2.1 [31, 54]. It should be noted that the evaluation of this amplitude ignores the strong interaction of the nucleon with the quark loop and so may not be numerically accurate. More recently, consideration of additional strong interaction effects associated with mesonic processes have indicated only relatively small additional corrections [58, 59, 60, 61]. It is important to note that the Q^2 dependence of the anapole form factor F_A could be different from the dipole form that is successful in fitting the tree level term G_A^Z . Maekawa and van Kolck [60] find to leading order in chiral perturbation theory that the momentum dependence of at least the isoscalar piece of the anapole form factor is softer than the dipole form (corresponding to a small radius for the anapole distribution); in this framework the isovector anapole moment is zero in leading order. In Figure 2.3, we present the difference between $G_A^e(Q^2)$, the axial form factor measured in PV electron scattering, and $G_A(Q^2)$, the corresponding quantity for neutrino scattering; the expected precision of the G0 measurements is also shown. As can be seen the combination of the $Q^2 = 0$ calculation and the SAMPLE data provide no real information about this difference in the Q^2 range of the proposed G0 separation. The study of the anapole contributions and other corrections to G_A^e is presently an active area of experimental and theoretical investigation and it is important to measure this quantity over a range of Q^2 values. [60]

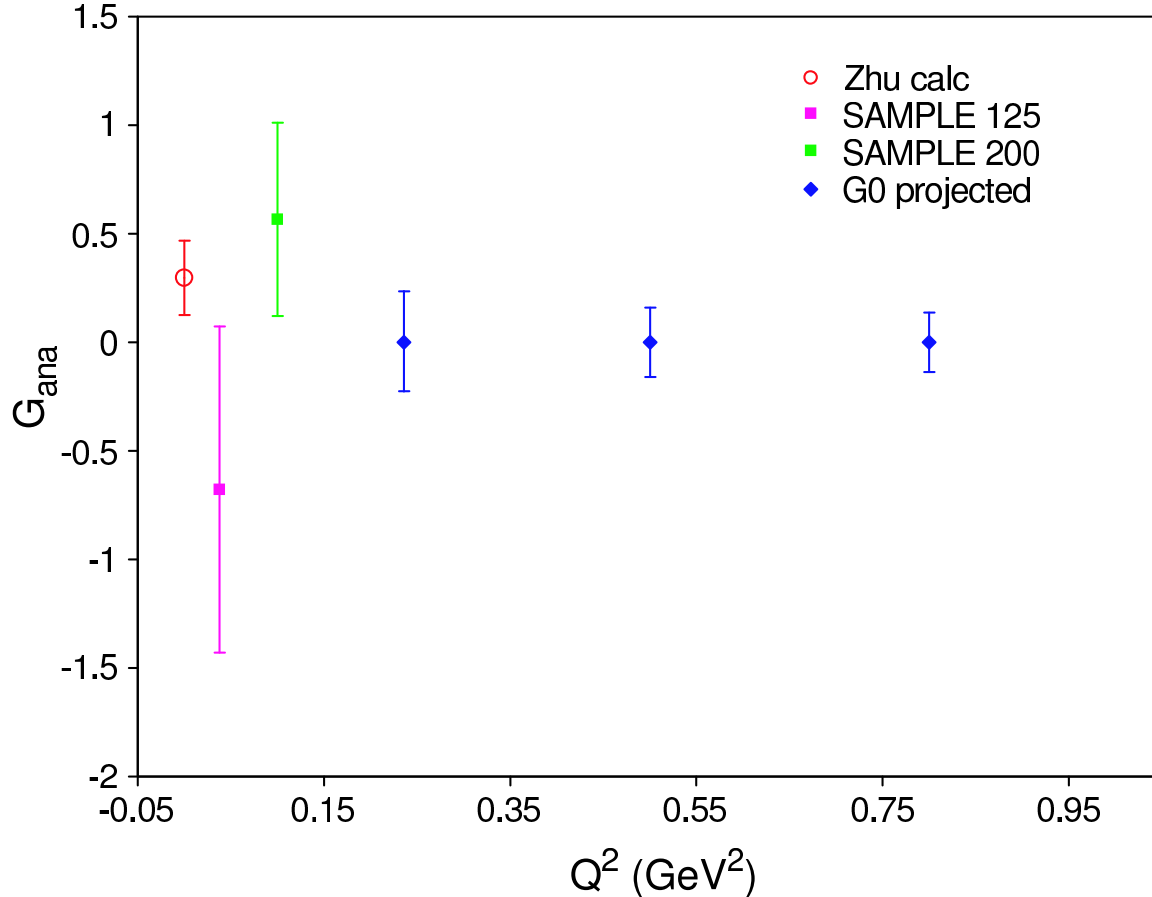


Figure 2.3: Compilation of the theoretical and experimental information on the difference between $G_A^e(T = 1)$ as measured in PV electron scattering and G_A from neutrino scattering. At present there is no theoretical calculation of the momentum transfer dependence of $G_A^e(T = 1)$.

2.3 Other experiments: past and future

The SAMPLE experiment at the Bates Linear Accelerator Center was the first to study strange form factors and the anapole contribution in parity-violating electron scattering. This experiment measures the elastic asymmetry from the proton and the quasielastic asymmetry from the deuteron at $Q^2 = 0.1$ GeV 2 [62, 63, 64, 65, 66]. In the most recent publication [67], analysis of the SAMPLE results is presented which yields a value of the strange quark contribution to the magnetic form factor

$$G_M^s(Q^2 = 0.1) = +0.37 \pm 0.20 \pm 0.26 \pm 0.07, \quad (2.22)$$

where the last uncertainty is due to uncertainties in the radiative corrections. The result for G_M^s is somewhat surprising, as its value was generally expected to be negative, based on the theoretical calculations (see Table 2.1). The values for G_A^e at both low momentum transfers measured in the experiment ($Q^2 \sim 0.03, 0.10$ GeV 2) are consistent [27] with the theoretical expectation of $G_A^e(T = 1) = -0.83 \pm 0.26$ [58]. As noted above, the Q^2

dependence of G_A^e is not easily calculated but there are indications that it is softer than a dipole form [60]. It is essential at the higher momentum transfers of interest here to measure the axial form factor to extract reliable values of G_M^s , and of course G_A^e itself is quite interesting to study experimentally.

For forward angle experiments in particular, it is convenient to express the deviation due to strange quark contributions in terms of $G_E^s + \eta G_M^s$

$$G_E^s + \eta G_M^s = \frac{4\pi\alpha\sqrt{2}\epsilon G_E^p{}^2 + \tau G_M^p{}^2}{G_F Q^2 \epsilon G_E^p (1 + R_V^{(0)})} (A_{phys} - A_{NVS}) \quad (2.23)$$

where $\eta(Q^2, E_i) = \tau G_M^p / \epsilon G_E^p$ and A_{NVS} is the no-vector-strange asymmetry (calculated with $G_E^s = G_M^s = 0$).

The HAPPEX experiments [2, 3, 6] utilized the two spectrometers in Hall A at Jefferson Lab to measure parity violation in elastic electron scattering at very forward angles. In the original measurement at $Q^2 = 0.477 \text{ GeV}^2$ the result was near that expected with the no-vector-strange (NVS) hypothesis ($G_E^s = G_M^s = 0$)

$$A_p(Q^2 = 0.477 \text{ GeV}^2, \theta_{av} = 12.3^\circ) = -14.60 \pm 0.94 \pm 0.54 \text{ ppm} . \quad (2.24)$$

or

$$\frac{G_E^s + 0.392 G_M^s}{G_M^p / \mu_p} = 0.091 \pm 0.054 \pm 0.039 . \quad (2.25)$$

as can be seen in Fig. 1.1. The new HAPPEX measurements, though not complete, support the hypothesis that $G_M^s \sim +0.5$ at low Q^2 and show a slight preference for $G_E^s < 0$. The additional running time is expected to yield uncertainties factors of two or three smaller than at present.

The PVA4 experiment at MAMI in Mainz has to date made measurements at a forward angle using an array of PbF_2 detectors. The most recent PVA4 measurement at $Q^2 = 0.1 \text{ GeV}^2$ also supports the general conclusions enumerated above (Fig. 1.2). The first PVA4 measurement [72] at $Q^2 = 0.23 \text{ GeV}^2$ determined a combination of form factors slightly different from that of the G0 forward angle experiment. The results of these two measurements are shown in Fig. 2.4. While the kinematic difference between the measurements is not sufficient for a separation of G_M^s and G_E^s , the region of overlap is certainly consistent with a $G_M^s \sim +0.5$ and $G_E^s \sim -0.05$.

Several future measurements are planned. The HAPPEX collaboration will, at the time of the PAC 28 meeting, be running to complete the $Q^2 = 0.1 \text{ GeV}^2$ measurements as indicated above. The PVA4 apparatus has been turned around, and data taking will also be beginning at backward angles (at, we believe, $Q^2 = 0.48 \text{ GeV}^2$). At Mainz, further backward angle running with both hydrogen and deuterium targets is planned.

In summary, there is now significant evidence that both G_M^s and G_E^s are non-zero. The proposed measurements will allow a separation of these form factors at two values of momentum transfer in a region where G_E^s may be sizeable and where the cancellation with ηG_M^s is significant in the forward angle measurements. There remains the opportunity

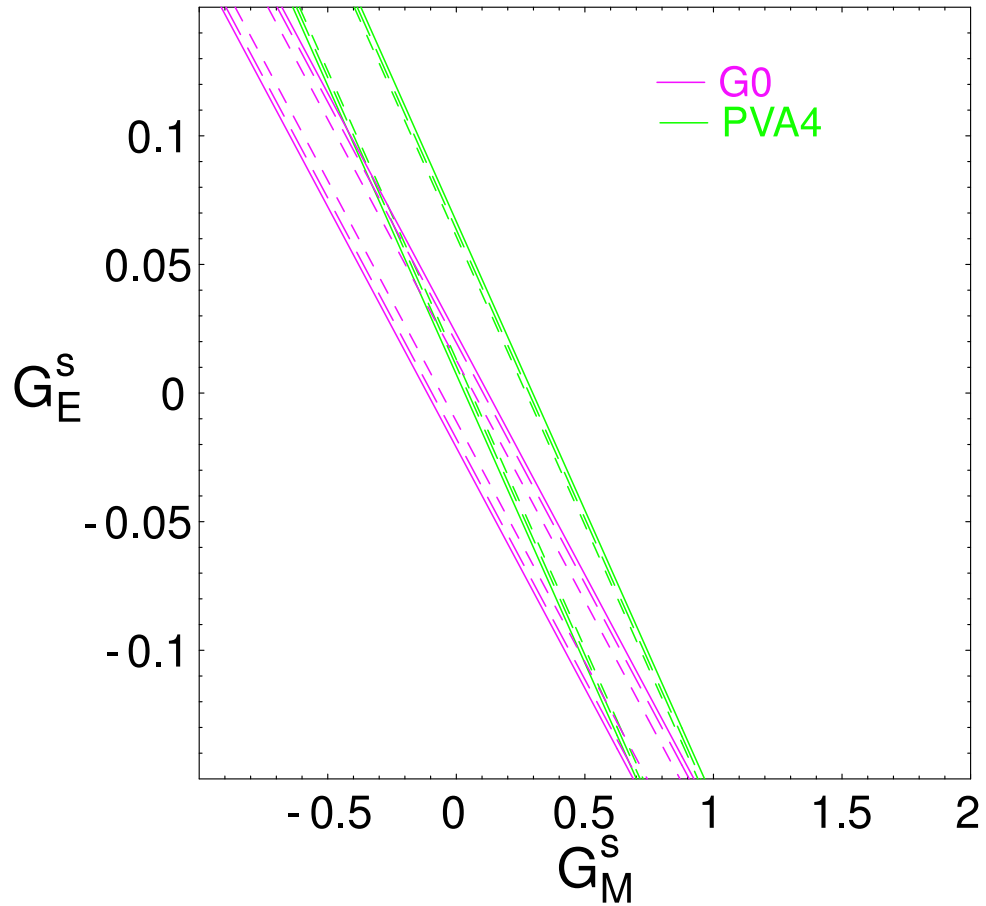


Figure 2.4: Results from the first PVA4 measurement [72] and the G0 forward angle measurement [1] at $Q^2 = 0.23 \text{ GeV}^2$.

to make a careful measurement of G_A^e at both momentum transfers, depending on the outcome of the first backward angle measurements at $Q^2 = 0.8 \text{ GeV}^2$.

3 Experiment

3.1 Introduction and Kinematics

In this experiment we propose to make measurements of the backward angle parity-violating asymmetries using both hydrogen and deuterium targets. The kinematics are chosen to approximately match the range of the forward angle running except for the very lowest momentum transfers (and beam energies) where the SAMPLE experiment has already made measurements [67, 27]. As shown in these measurements and discussed above (Section 2), measurements involving quasi-elastic scattering from deuterium are necessary to separate the vector and axial vector currents of the nucleon. The G0 experimental program therefore includes, in addition to the recently completed forward angle measurement, backward angle measurements with both targets.

We propose to make these backward angle measurements at three values of Q^2 (elastic in the case of the hydrogen target, quasi-elastic in the case of deuterium) to give a reasonable amount of information on the Q^2 variation of the three form factors G_E^s , G_M^s and G_A^e ($T = 1$). The first of these measurements, at $Q^2 = 0.8 \text{ GeV}^2$ is scheduled to begin in December 2005 and will involve both hydrogen and deuterium targets. The split of time for hydrogen and deuterium running for the subsequent measurements will be determined as discussed above. The nominal central angle for the G0 spectrometer for these measurements is 110° , thus fixing the incident energies. For reference, the kinematics, (quasi-) elastic rates (for the entire spectrometer acceptance), and nominal asymmetries for all three momentum transfers are shown in Table 3.1

Target	E (GeV)	θ ($^\circ$)	Q^2 (GeV^2)	Rate (MHz)	Asymmetry (ppm)
^1H	0.360	110	0.23	3.14	-13
^2H	0.360	110	0.23	4.66	-18
^1H	0.585	110	0.48	0.718	-32
^2H	0.585	110	0.48	1.100	-43
^1H	0.799	110	0.8	0.190	-54
^2H	0.799	110	0.8	0.274	-72

Table 3.1: Elastic and quasi-elastic kinematics, rates, and nominal asymmetries.

The new experimental aspects of this measurement (as compared to the forward angle measurements where the asymmetries are significantly smaller) are associated with the quasi-elastic scattering from deuterium. Accordingly, in the remainder of this section, we address only the corrections necessary to extract single nucleon information from the quasi-elastic scattering as well as the requirements for particle identification accruing from the quasi-free π^- production from the neutrons in the target.

3.2 Deuterium corrections

Because the third asymmetry measurement that allows separation of the three weak form factors involves a nuclear target, there are potentially nuclear corrections to be considered. These corrections fall into two categories: contributions from processes other than quasielastic scattering, such as elastic, threshold breakup and Δ production, and those that arise in quasielastic scattering but from non-nucleonic currents in the deuteron, such as meson exchange.

The experimentally measured asymmetry can be written as

$$A_D = \frac{\sigma_{QE}A_{QE} + \sigma_{el}A_{el} + \sigma_{ted}A_{ted} + \sigma_{\Delta}A_{\Delta}}{\sigma_{QE} + \sigma_{el} + \sigma_{ted} + \sigma_{\Delta}} \quad (3.1)$$

where the four terms are contributions from quasielastic scattering, elastic e - d scattering, threshold breakup, and Δ production, respectively. Nucleon resonances higher than the Δ are not considered.

The asymmetry due to elastic e - d scattering was calculated by Pollock [82] and in [22], and, neglecting the small D-state contribution to the deuteron wave function, can be summarized by the expression

$$A_{el} = \frac{G_F Q^2}{4\pi\alpha\sqrt{2}} \left[4\sin^2\theta_W + \frac{2G_M^s}{(G_M^p + G_M^n)} F_T \right], \quad (3.2)$$

where $F_T = v_T B(Q^2)/(A(Q^2) + B(Q^2)\tan^2(\theta/2))$, where $A(Q^2)$ and $B(Q^2)$ are the elastic deuteron structure functions, and v_T is the usual kinematic factor. The asymmetry for threshold breakup was also calculated in [22] and may be written as

$$A_{ted} = -\frac{G_F Q^2}{4\pi\alpha\sqrt{2}} \left[(2 - 4\sin^2\theta_W) - \frac{v_{T'}}{v_T} (4 - \sin^2\theta_W) \frac{M_N G_A^e(T=1)}{q 2G_M^{T=1}} \right] \quad (3.3)$$

where $v_{T'}$ is the standard kinematic factor. Although in each case there is some dependence on the unknown form factors G_M^s and G_A^e , both asymmetries are comparable in magnitude to A_{QE} . The effect of such events on A_D is negligible: in the worst case the elastic (threshold) cross sections are 3% (0.1%) of the integrated quasielastic cross sections.

The inelastic scattering contribution, which will arise primarily from Δ excitation, can potentially modify the measured asymmetry from that expected from quasielastic scattering alone and can likely not be neglected. The asymmetry in hydrogen is the subject of the proposal of S. Wells *et al.*, [83], where the formalism for parity violation in the N - Δ transition is documented. Following the notation of Mukhopadhyay, *et al.* [84],

$$A_{\Delta} = -\frac{G_F Q^2}{4\pi\alpha\sqrt{2}} \left[\Delta_{(1)}^{\pi} + \Delta_{(2)}^{\pi} + \Delta_{(3)}^{\pi} \right] \quad (3.4)$$

The two terms $\Delta_{(2)}^{\pi}$ and $\Delta_{(3)}^{\pi}$ combined are expected to be $\sim 0.2\Delta_{(1)}^{\pi}$, and are thus neglected for the purposes of the background calculation. The quantity $\Delta_{(1)}^{\pi} = 2(1 - 2\sin^2\theta_W) = 1.075$ [28]. In [85], A_{Δ} in a nucleus was considered. At backward angles, the dominant contribution is from quasifree Δ production, so $A_p \sim A_n \sim A_d$.

The contribution to the asymmetry from quasifree Δ production was estimated by simulating the detector acceptance for both elastically and inelastically scattered electrons in the CED and FPD arrays. These events result in two bands in FPD/CED space with very little overlap at the two lowest kinematics, somewhat more overlap at $Q^2 = 0.8$ (GeV/c)². The FPD/CED pairs corresponding to elastic scattering were then selected and each rate summed over all such pairs. The contribution from inelastic scattering is small except at the highest momentum transfer, where such events are expected to result in a reduction of the measured asymmetry in the elastic region of FPD-CED space of about 10%. It is important to note that, just as in the case of the hydrogen data, the inelastic asymmetry in deuterium will be measured simultaneously with the quasielastic scattering asymmetry over a range of Q^2 and ν , so it will be possible to make any necessary correction with measured inelastic asymmetries rather than relying on a calculation.

The second major class of corrections to be considered are corrections to the simple “static approximation” for the deuterium asymmetry:

$$A_d = \frac{\sigma_p A_p + \sigma_n A_n}{\sigma_d} \quad (3.5)$$

In this expression the deuteron is assumed to consist of a noninteracting neutron and proton at rest. Hadjimichael, *et al.* [24] have considered the effect of final state interactions on this expression. They performed their calculation with two nucleon potentials that represent the extremes of the state-of-the-art potentials. Near our kinematics, they find that the correction to the static asymmetry expression is small ($\sim 1\%$), and the variation between the two nucleon potentials used is also small ($\sim 1\%$). Two body currents (meson exchange currents) have been considered by the authors of refs [78, 25]. Schramm and Horowitz [78] considered heavy meson exchange corrections; they find that the correction to the asymmetry is less than 1% at our momentum transfer. The most recent work [25, 26] which also incorporates pion exchange currents also finds that the corrections are small.

Finally, there is the possibility of an asymmetry generated by a nuclear parity-violating component in the deuteron wavefunction. This effect has been calculated in refs [79, 80] and shown to be small compared to our expected asymmetries. For example, Hwang, *et al.* [80] used the DDH [81] parameters to characterize the parity-violating nucleon-nucleon interaction, and they find that the asymmetry is $A \sim 4 \times 10^{-7}$ at backward angles at 0.500 GeV for relative energy $E_{np} = 9$ MeV. The asymmetry falls with increasing E_{np} , so it will be even less significant at the quasielastic peak.

3.3 Particle identification requirements

Negatively charged pions have been found to produce a significant background to the elastic and quasielastic rates detected by the G^0 spectrometer at backward angles. The pions are produced mainly by photoproduction near the Δ -resonance. In the case of a hydrogen target, single π^- photoproduction is forbidden by kinematics; two pions must be produced in order to see a single π^- in the spectrometer. However, in the case of a deuterium target, single π^- photoproduction occurs due to the presence of neutrons.

This background is found to dominate over quasi-elastic rates from deuterium at backward angles. The background can be kinematically separated from elastics in the hydrogen target case, but tends to overlap with the inelastic electrons in the measurement of the parity violating asymmetry in the $N \rightarrow \Delta$ transition [83]. It is therefore desirable to have an additional particle identification detector for the backward angle experiment.

3.3.1 Calculation of π^- Cross Sections

The process of π^- photoproduction from the neutron can be simulated using photoproduction cross-sections with the appropriate Bremsstrahlung and virtual photon fluxes. These processes were used both for the deuterium itself and for (quasi-free) production from the aluminum target windows in each case.

For the virtual photon contribution to the cross section, the MAID [86] parameterization of the transverse photoproduction pion cross section was used with a virtual photon flux [87] and appropriate Jacobian factors. Fermi motion was included in the model, using Monte Carlo generation of initial state nucleon momenta, according to a nucleon momentum distribution obtained from a fit of inclusive quasi-elastic scattering data.

For the Bremsstrahlung photon contribution to the cross section, the GRAAL Monte Carlo generator was used [88]. This generator was found to be in good agreement with a model using the photoproduction cross section from MAID and the Bremsstrahlung photon spectrum of Ref. [89]. The GRAAL Monte Carlo code has the additional capability of simulating two-pion production.

These cross sections were also tested against the commonly used code of Lightbody and O'Connell (LBOC) [90]. For kinematics similar to those encountered in G^0 , the MAID and GRAAL results were found to be a factor of 3 to 4 larger than those given by the LBOC code. This was determined to be due to the older pion photoproduction cross-section parameterization used in the LBOC code, and due to bugs in the LBOC code.

3.3.2 Measurement of π^- Rate at Backward Angles

To test the pion photoproduction cross-section calculation in kinematics similar to those planned for G^0 backward-angle running, a facility development request to use the Short-Orbit Spectrometer (SOS) in Hall C was generated. During a parasitic run on October 27-29, 2000, π^- photoproduction cross sections from hydrogen, deuterium, and carbon targets were measured. Elastic and quasielastic cross-sections were also measured. For these measurements, the beam energy was 0.824 GeV, and the SOS angle was fixed at 136.5° . Rates for negatively charged particles were measured in the momentum range 150 to 400 MeV/c. The beam current averaged 20 μ A. Data for hydrogen and deuterium were taken with two different target lengths (4 and 15 cm) to test the ability of the calculations to accurately predict the fractions of the total pion rate due to virtual photons and Bremsstrahlung photons.

The results and analysis of the pion data from this run are reported in a G^0 internal note [91] and will be summarized here. The measured π^- cross sections from hydrogen are

shown in Fig. 3.1. The cross section is compared with a calculation using the GRAAL

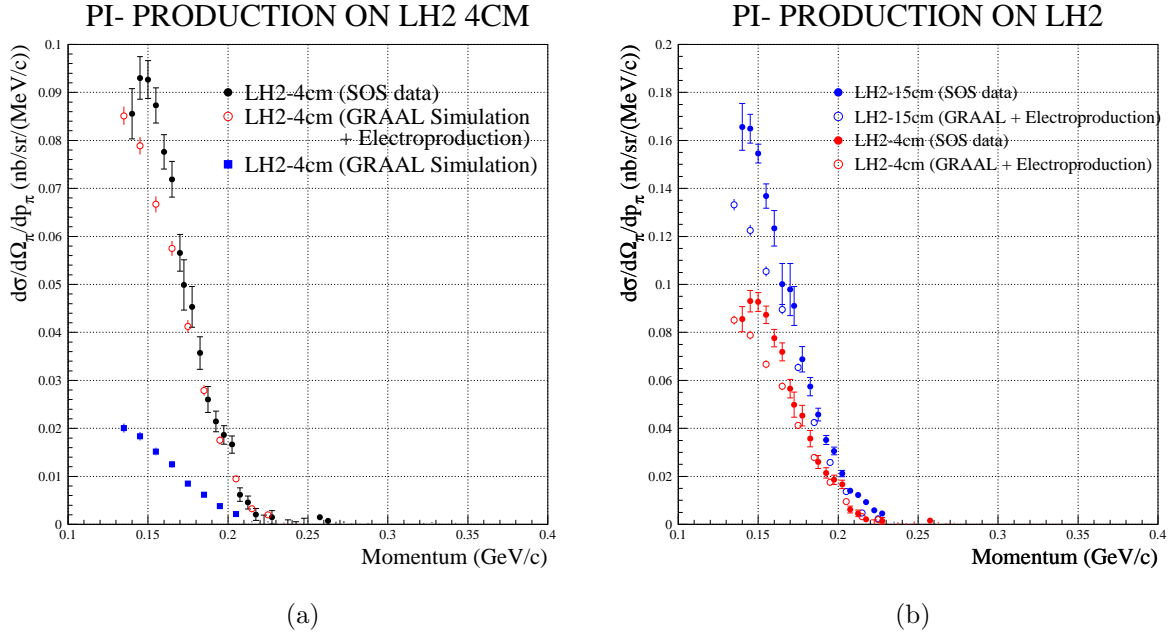


Figure 3.1: Comparison of data and simulation of π^- production from (a) 4 cm and (b) 15 cm LH_2 targets.

code. The breakdown of electroproduction and photoproduction pieces of the cross section in the simulation is also shown. The disagreement at lower momentum is believed to be due to the fact that the GRAAL code does not presently simulate virtual photons below a certain Q^2 . The G^0 spectrometer will generally select pions of higher momentum, so the agreement is sufficient to be able to use the code to generate two pion production for simulation of backgrounds in the experiment.

The measured π^- cross sections from deuterium are shown in Fig. 3.2. The cross sections are compared with the simulation using the GRAAL code for pion photoproduction and the MAID-based calculation for pion electroproduction. The cross section is dominated by single π^- production. The agreement of the data with the calculation is excellent, indicating that the cross section for the G^0 case is well understood.

The ratio of the pion rates from the 15 cm and 4 cm liquid hydrogen and liquid deuterium was found to be roughly 1.6, in agreement with arguments based on the radiation length of the target and the equivalent radiator for virtual photons at these kinematics.

3.3.3 Pion Rates and Contaminations

Pion rates for G^0 backward angle running were determined using the models of the cross section tested in the previous section, along with a GEANT-based model of the G^0 acceptance [92].

PI- PRODUCTION ON LD2

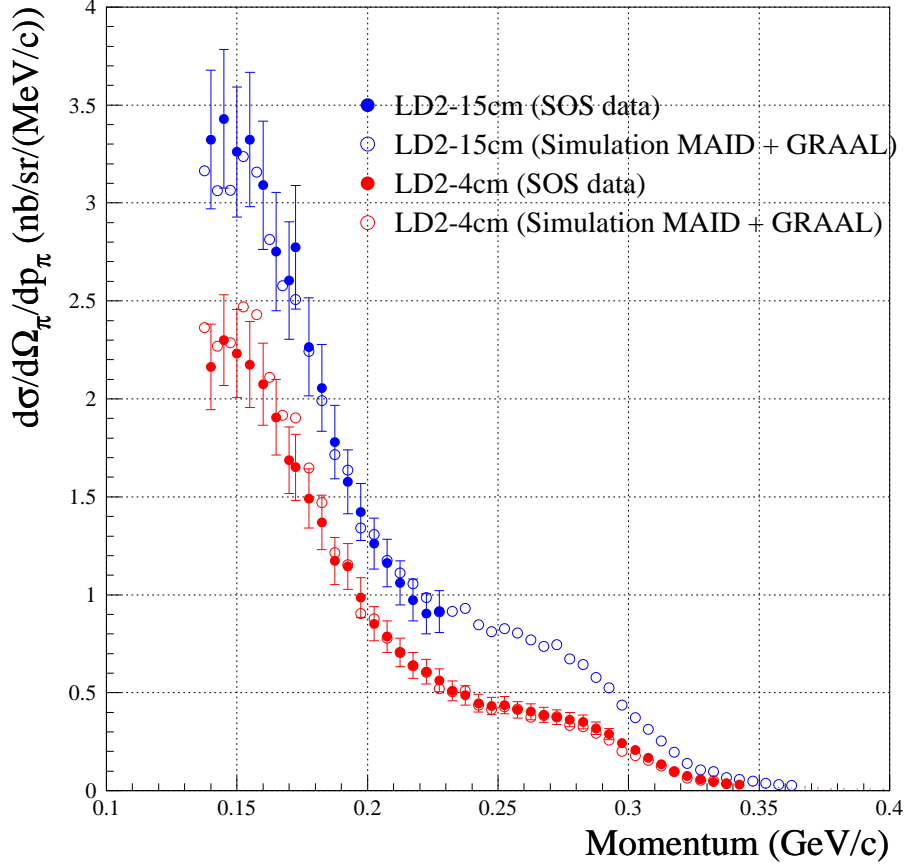


Figure 3.2: Comparison of data and simulation of π^- production from 4 cm and 15 cm LD_2 targets.

The pion rates for the liquid hydrogen target running are found to be largest relative to the elastic rate for the already approved beam energy of 0.799 GeV. The pion, elastic electron, and inelastic electron rates for 0.799 GeV are shown in Fig. 3.3. Rates are proportional to the size of the box shown for each CED and FPD combination. The rates assume a 20 cm long target and 40 μA beam current. Tracking of all secondaries was included. Muons resulting from pion decay are also included in the pion rates. At 0.799 GeV, muons present 15% of the total flux of pions and muons at the location of the CED. At 0.424 GeV, 20% of the total flux is due to muons*. The pion rates are found to be roughly 25% of the elastic rate along the locus of the elastic curve at 0.799 GeV.

The pion rates for LH_2 running are dominated by contributions from the aluminum target windows. For this simulation, only the contribution of virtual photons interacting with the target windows was included, and final state effects and Fermi motion were ignored.

*Rate calculations for the proposed beam energy of 0.360 GeV have not yet been performed but are not expected to be substantially different.

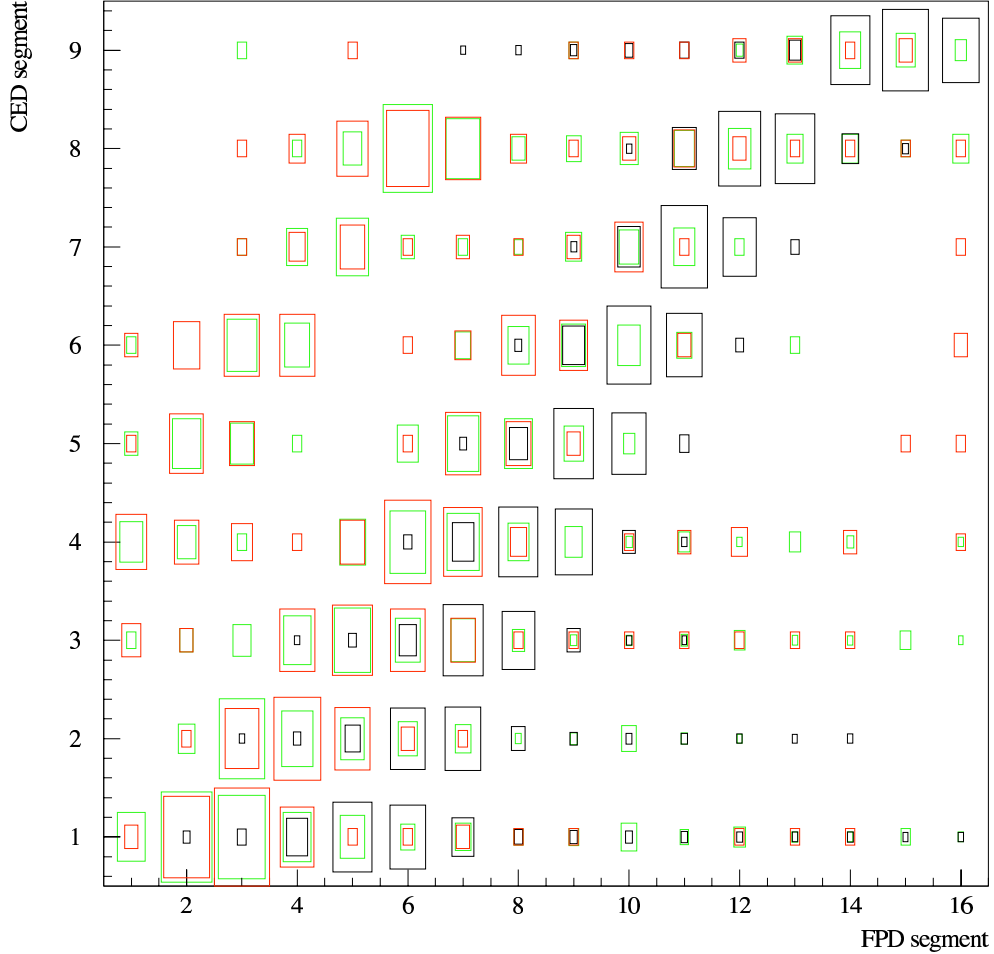
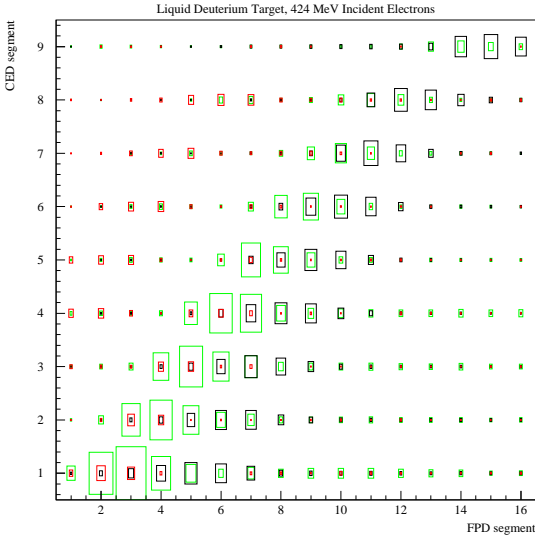


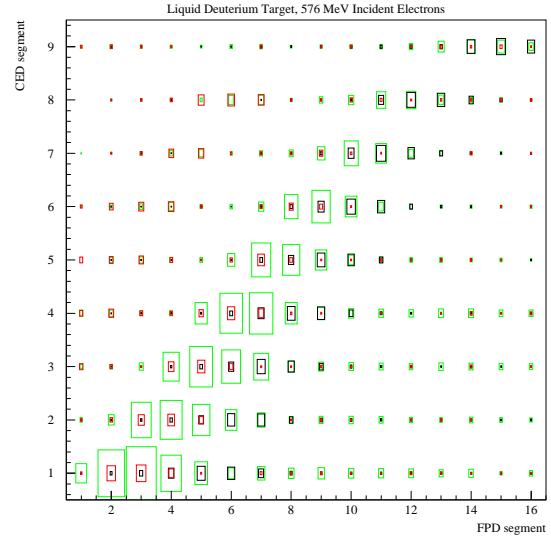
Figure 3.3: Relative CED and FPD rates for one octant of the G^0 spectrometer, LH_2 target, for beam energy 0.799 GeV. The coincidence rate is proportional to the size of the box. Elastic e^- rates are shown in black, inelastic e^- rates are shown in red and estimated π^- rates are shown in green.

Inclusion of real photons increases the pion rate by a factor of 1.5, but final state interactions should reduce the cross section by roughly 50%, so these two effects roughly cancel. The effect of Fermi smearing does not change the overall rate, but causes the pions to have more overlap kinematically with the elastic electrons. The effect of this will be discussed later.

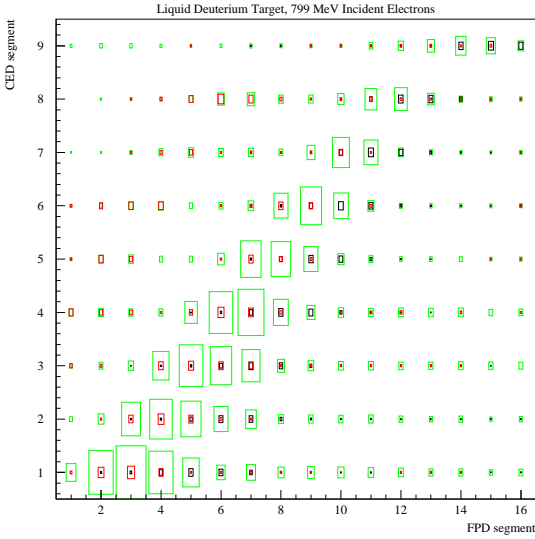
The π^- rates for LD_2 running are shown in Figs. 3.4(a), (b), and (c) for beam energies of 0.424, 0.585, and 0.799 GeV, respectively. (Rate calculations for the proposed beam energy of 0.360 GeV have not yet been performed but are not expected to be substantially different.) As expected, the negative pion rates are considerably larger for liquid deuterium. The aluminum target windows account for roughly 1% of the total rate, with the remaining 99% being roughly equally divided between contributions from virtual photon and Bremsstrahlung photon fluxes to the π^- photoproduction cross section from the LD_2 in the target itself. There is a large pion contamination in all three cases, preventing the



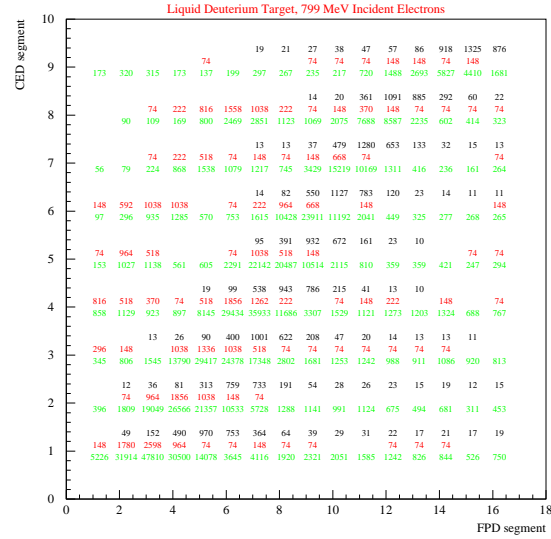
(a)



(b)



(c)



(d)

Figure 3.4: Relative CED and FPD coincidence rates for one octant of the G^0 spectrometer, LD_2 target. The coincidence rate is proportional to the size of the box. Quasi-elastic e^- rates are shown in black, inelastic e^- rates are shown in red and estimated π^- rates are shown in green. (a) 0.424 GeV, (b) 0.585 GeV, (c) 0.799 GeV. Figure (d) contains the rates for 0.799 GeV, in text form. Rate calculations for the proposed beam energy of 0.360 GeV have not yet been performed but are not expected to be substantially different.

measurement of the quasi-elastic asymmetry for the deuteron in the absence of additional particle identification (the aerogel Cherenkov detector is discussed in Section 4.1.3).

Selecting certain CED and FPD combinations allows the optimization of the elastic/inelastic separation. The same selection procedure also helps to exclude pions from the elastic sample. Table 3.2 summarizes the pion contaminations expected for the proposed kinematics, satisfying the same cuts used to separate elastic from inelastic electrons described in Section 2. As mentioned earlier, the pion contamination for the liquid hydrogen

E_{beam} (GeV)	$(\pi + \mu)/e$ ratio	
	LH ₂	LD ₂
0.424	0.013	0.39
0.585	0.042	1.6
0.799	0.25	8.4

Table 3.2: $(\pi + \mu)/e$ ratio expected for same CED and FPD combinations used in Section 2 to attempt to separate elastic from inelastic electrons. Here only elastic and quasi-elastic electrons are counted in the denominator. Calculations have not yet been performed for the proposed beam energy of 0.360 GeV, but the contamination ratios will be smaller than at 0.424 GeV.

target running is dominated by contributions from the target windows. The contribution from two-pion production in the liquid hydrogen target itself to the total pion rate is 15% at 0.799 GeV, but is negligible at lower energy. As mentioned earlier, the effect of Fermi-smearing of the kinematics of these pions was neglected. Fermi smearing of the pion kinematics has been estimated to give roughly a factor of 2 increase in the contamination, for the lowest beam energy proposed. The relative size of the effect will be smaller at higher energy, as the Fermi momentum becomes small relative to the beam energy. The estimated pion contaminations for LH₂ should therefore be accurate to the 50% level.

The pion contamination for LD₂ *was* calculated including Fermi motion. As already noted, this contamination is found to be too large to make a measurement of the quasi-elastic asymmetry in deuterium as the pion to elastic electron ratio is 8.4:1 in the worst case. A particle identification detector must provide a pion rejection of better than 100:1, to reduce the worst-case pion contamination to the level of 10%.

The pion contamination of the inelastic electron rate from LH₂ is obviously worse than for the elastic case. The proposed measurement of the parity violating asymmetry in the $N \rightarrow \Delta$ transition [83], using the LH₂ running, would therefore also benefit from additional particle identification [93].

3.3.4 Rejection of π^- Background

The kinematics of the pions and muons which need to be rejected for each proposed beam energy are shown in Table 3.3. The type of detector affording the best π/e discrimination at these energies and the simplest implementation in the current G⁰ geometry is an aerogel Cherenkov counter. The index of the aerogel should be less than $1/\beta$ (see Table 3.3), but

E_{beam} (GeV)	p_{π} range (MeV/c)	β_{π}^{max}	p_{μ} range (MeV/c)	β_{μ}^{max}
0.424	100 - 250	0.87	50 - 225	0.90
0.585	100 - 300	0.91	50 - 275	0.93
0.799	100 - 375	0.94	50 - 350	0.96

Table 3.3: Pion and muon kinematics for each spectrometer setting. Recall that muons account for less than 20% of the total pion and muon flux. The lowest proposed energy is 0.360 GeV and not the 0.424 GeV energy listed in the table.

should be as large as possible to maximize light yield. It is therefore found that $n = 1.03$ is a good choice. An aerogel Cherenkov counter should also be able to give the requisite better than 100:1 pion rejection. The construction of the Cherenkov counters for G^0 will be discussed in Section 4.1.3.

4 Apparatus

4.1 Detectors

The detector system to be used for these backward angle measurements consists of two arrays of scintillators and an aerogel Cherenkov detector for each of the eight G0 octants. The two scintillator arrays comprise: a Focal Plane Detector (FPD) array (sixteen detectors per octant each viewed from two ends), which have been used for the forward angle measurements, and a Cryostat Exit Detector (CED) array (nine detectors per octant each viewed from two ends). For backward angle electron detection, both arrays are required to determine the electron scattering angle and momentum, thereby providing an adequate separation between elastically and inelastically scattered electrons. The Cherenkov detector is required to reduce the contribution of π^- 's, particularly important during running with the deuterium target. Additionally, a set of two high resolution drift chambers will be placed in one octant during commissioning to measure backgrounds.

4.1.1 FPDs

In the forward angle measurement, back-to-back pairs of FPD scintillators are used to detect protons. In the back angle measurement 16 single FPD scintillators will be paired with CED scintillators to detect elastic and inelastic electrons as indicated below (the back element of each FPD pair will not be used in the back angle measurement). A photograph of completed North American (NA) and French FPD octants is shown in Figure 4.1; the octants are supported from a detector support (“ferris wheel”) shown in Figure 4.2. Each FPD scintillator has a curved shape roughly 60 - 120 cm in length and a width of 5 - 10 cm. The first four FPD elements are 5 mm thick; the remainder have a thickness of 1 cm. Each is connected to a pair of photomultiplier tubes via lucite lightguides. The measured yield at each phototube is of order > 75 p.e. for minimum ionizing particles. These detectors performed as expected in the forward angle G0 run.

4.1.2 CEDs

The CEDs are a critical component of the G0 backward angle running, and here we provide a summary of the progress to date on this detector package. There are nine CEDs that, together with the FPDs, define the momentum and scattering angle of the detected electrons thus allowing for separation of elastic and inelastic events. With front end electronics composed of gate arrays (see Section 4.2), we are able to record events for given pairs of CED/FPD combinations, and thereby measure asymmetries for both elastic and inelastic events.

The design and construction of the CED elements has been completed. A detailed simulation of expected light yield from these detectors was first performed, and the number of pho-



(a)



(b)

Figure 4.1: Photograph of complete sets of FPDs mounted into the FPD octant support; a) North American b) French.

toelectrons predicted was found to be more than adequate for these measurements [94, 95]. A prototype CED was constructed at TRIUMF, and tested at Louisiana Tech University using the same PMT/base assemblies to be used in the North American FPDs, and the amount of light collected was consistent with the predicted amount.

The procedure for manufacturing the correct shapes for the detectors and light guides was also developed and tested in the construction of the prototype CED. All scintillators and light guides, manufactured at TRIUMF, are now at JLab and assembly of all octants is complete.

The design and construction of the octant support structure for the CEDs is also complete. The design, a schematic of which is shown in Fig. 4.3, takes into account both the required mechanical support of the CED scintillator/light guide/PMT and base assemblies, as well as the relatively weak alignment constraints on these detectors. Also shown in this figure are the relative positions and shapes of the CEDs, light guides, and PMT's. Each octant support will be attached to the outer ring of the ferris wheel to provide the main mechanical support in the region of the CED assembly near the PMT's where the majority of the weight of these detectors resides. The positioning of the scintillators, as well as additional mechanical support, is obtained through the use of cantilevered struts extending from the main support through the region near the bend in the light guides and outside of the acceptance of the scattered electrons. This octant support design is integrated with the

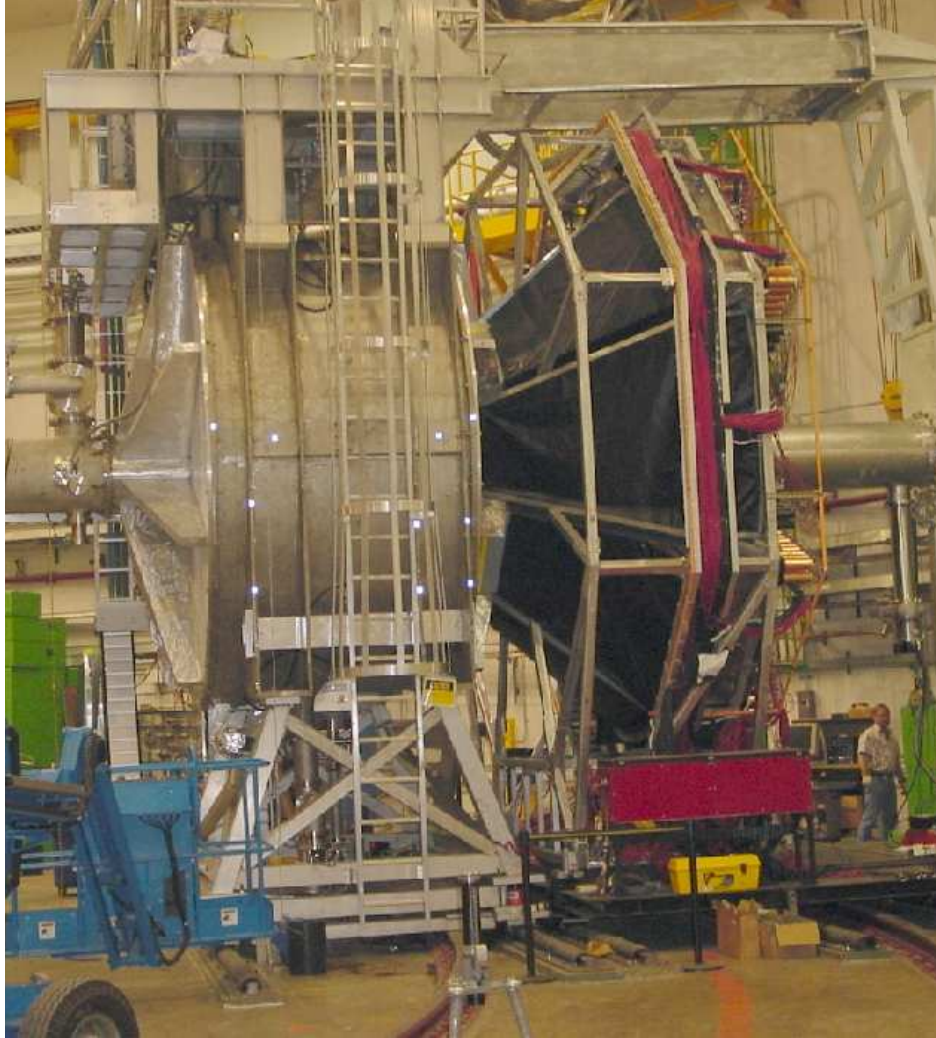


Figure 4.2: Photograph of G0 magnet and detectors in forward configuration.

support structure for the Cherenkov detectors. As part of the design process, the entire support structure was also prototyped in conjunction with developments discussed above.

4.1.3 Aerogel Cherenkov

The π^- background from $(n(e, \pi^-)e'p)$ will be reduced by introducing cuts in CED-FPD space, but not to a level sufficient to isolate quasi-elastic electrons. Therefore an aerogel Cherenkov detector has been designed to provide pion rejection across the full G0 momentum range, up to ~ 400 MeV/c for $Q^2 = 0.8$ GeV². This, of necessity, must be an eight-sectored array of individual Cherenkov detectors mounted in conjunction with the CED-FPD sectors. The Cherenkov is located between the CEDs and FPDs and its mounting is part of the overall extension of the ferris wheel discussed above. The geometry of the overall system is shown in Figure 4.4. A single Cherenkov detector is shown in more detail in Figure 4.5.

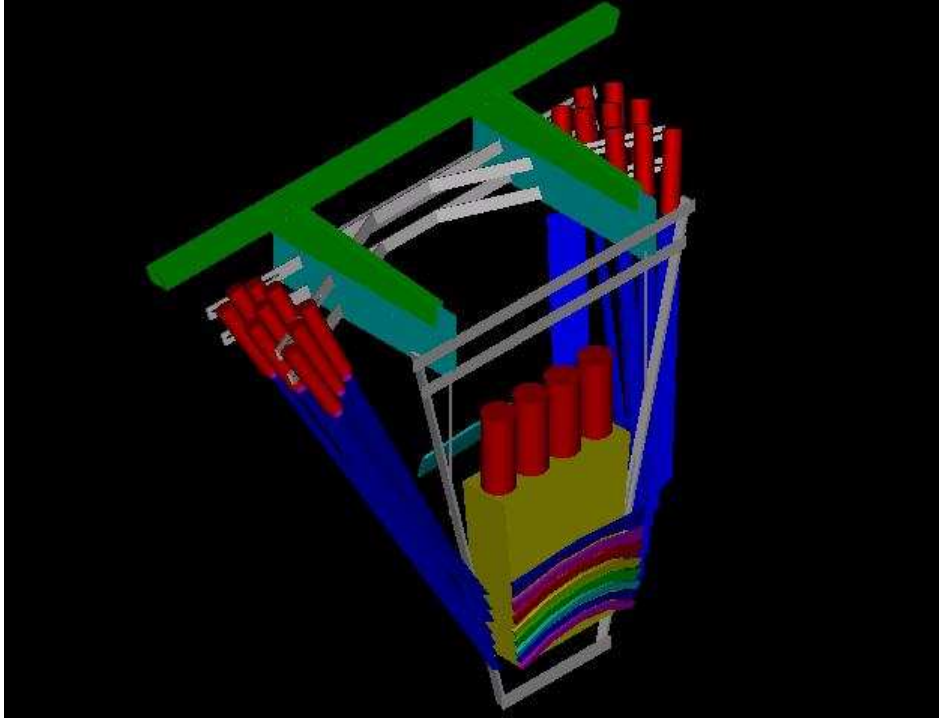


Figure 4.3: Schematic diagram of the CED octant support structure, showing the relative locations of the scintillators, light guides, and PMT's. Also shown is the relative position of a Cherenkov detector for backward-angle measurements.

Negatively charged particles entering an octant of the G0 spectrometer pass through 5 cm of aerogel. The aerogel has a proposed index of refraction $n = 1.03$, so that a particle with a speed such that $\beta > \frac{1}{1.03}$ will produce Cherenkov light. Thus, pions up to a momentum of 570 MeV/c will not produce any light. On the other hand, all primary electrons will produce light. Thus the detector will operate in *coincidence* mode and not in *veto* mode.

The light is emitted within a small angle ($\cos \theta_c = \frac{1}{1.03}$ at max.) and enters a downstream region whose walls are lined with a white diffuse reflector. The likelihood of a photon reaching one of four phototubes is related to their active area compared to the total internal area of the light box, which is a little better than 4%. Other goals in the box's design are to cover as large a fraction as possible of the G0 acceptance while keeping the timing spread as narrow as possible.

With 5 cm of clear aerogel, the electrons generate a signal of about 6 photoelectrons; whereas a 400 MeV/c pion would have a rejection factor of $\frac{1}{125}$. This latter pion signal is mostly due to δ -rays produced in the CEDs or elsewhere.

The phototubes for the Cherenkov counter for each octant are tied together to produce one summed signal. This signal is discriminated and ANDed into the trigger. Using existing sampling channels, Cherenkov ADC spectra will be used to check the calibration and pion rejection factor of each octant.

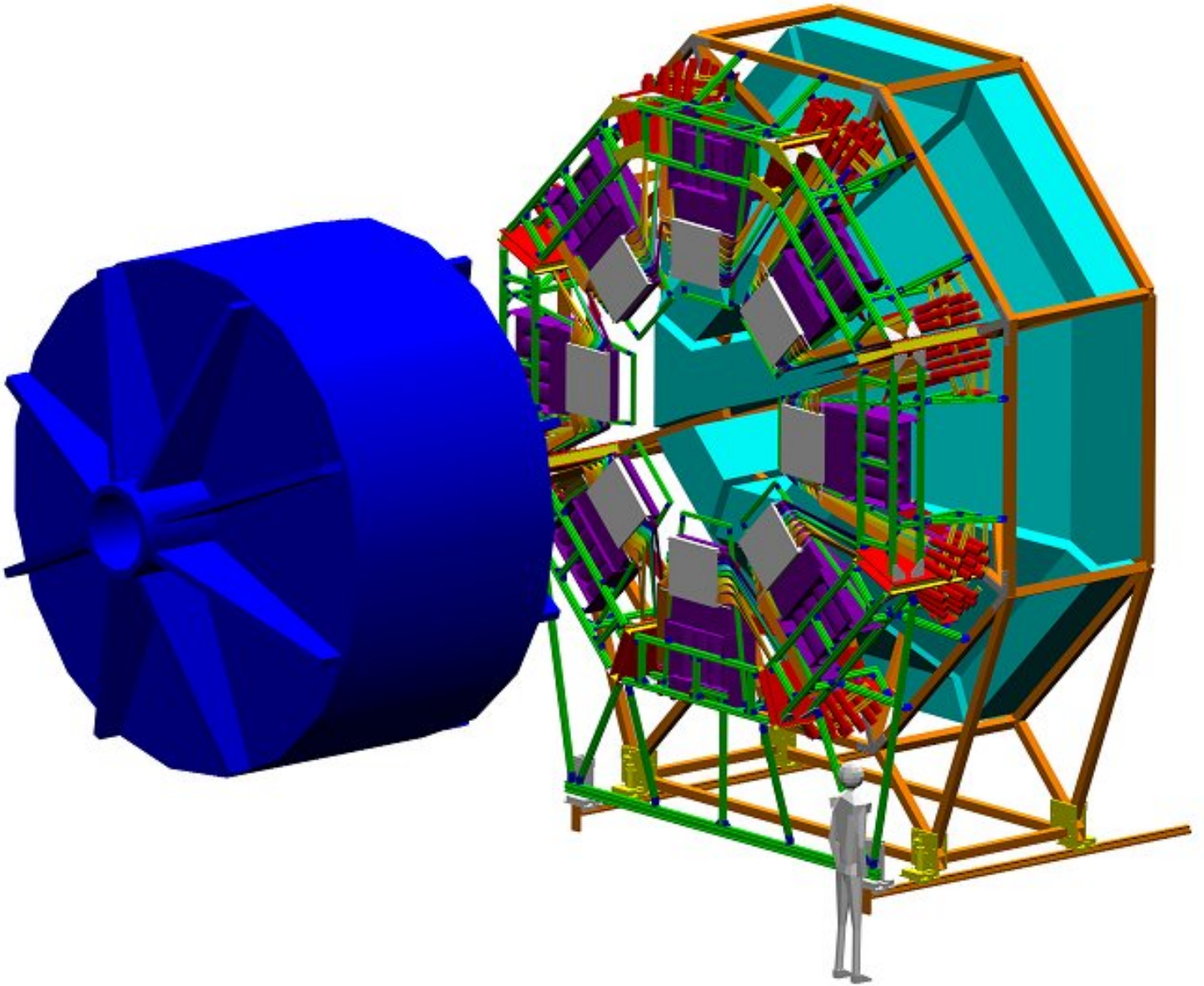


Figure 4.4: Concept drawing of the full eight-sectored G0 backward angle set-up. Each sector shows the full detector arrangement: CED, Cherenkov, and FPD. The magnet cryostat is shown in blue at left. In this view the electron beam would enter from the right.

The typical time-width of the signal from these detectors is ~ 20 ns (due mainly to collection time in the light box), during which time the radiator is ‘dead’. This is because the light can bounce around in the box for some time. The rise time of the pulse is of the order of 1 ns.

Studies with both Monte Carlo simulation and prototypes of the Cherenkov counter have been done in France and at TRIUMF. Most of the assumptions above come from tests and simulations performed by the Caltech group and Grenoble simulations [96, 97]. At Caltech,

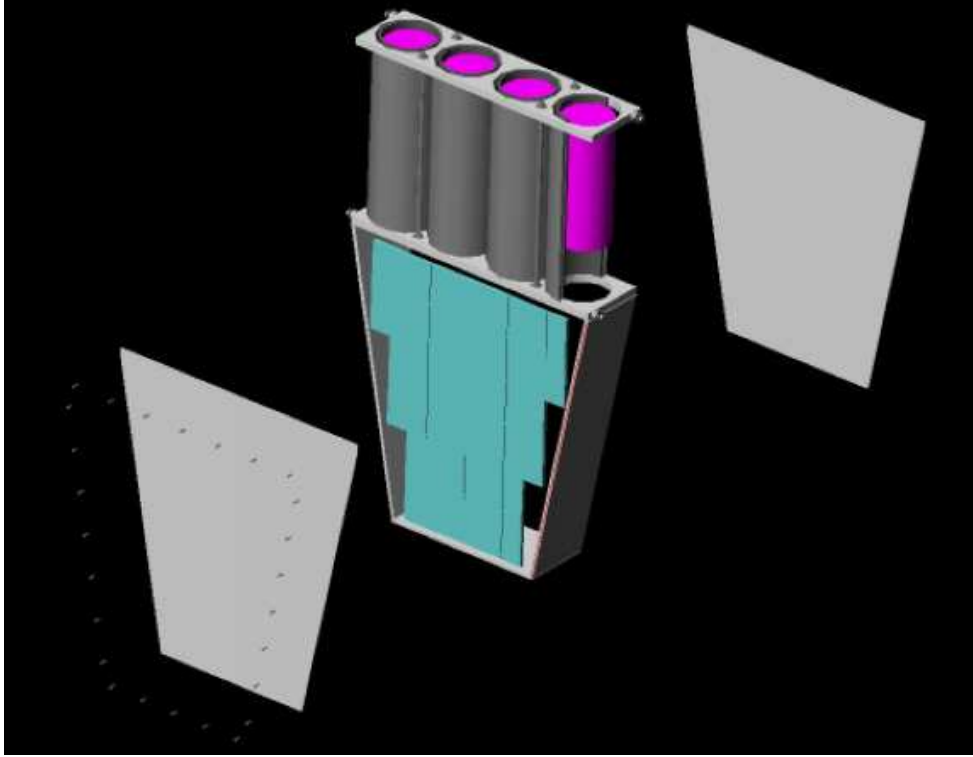


Figure 4.5: A view of the concept of a single octant light-box with aerogel Cherenkov radiator and PMT's

a small Cherenkov test counter using a single phototube was built for the purpose of testing light yield and timing calculations from Monte Carlo simulations based on Ref. [98], and was found to produce results similar to the simulation. A first test detector was built at Caltech and tested at TRIUMF using a mixed particle test beam. An example of the results from this detector is shown in Figure 4.6 where the pion rejection is shown to be sufficient for our purposes. At TRIUMF a full size prototype was constructed and tested on the M11 $\beta \sim 1$ “electron” beamline. An example of the results from this test is presented in Figure 4.7, where the number of photo-electrons is shown for three different incident beam locations relative to the tubes. The French version of the detector is essentially identical, and similar test results have been obtained there.

Both the French and NA detectors are complete and at JLab. Installation of the detectors into the support structure is ongoing during summer 2005.

4.1.4 Drift Chambers

A pair of drift chambers will be placed into one octant of the detector system during commissioning in order to perform a high resolution study of backgrounds in the back angle experiment. The two drift chambers (DC1 and DC2) used in the HKS spectrometer for experiment E01-011 have been secured for this use. A photograph (Fig. 4.9) and drawing (Fig. 4.10) of one of the chambers is provided. These chambers, with specifications listed

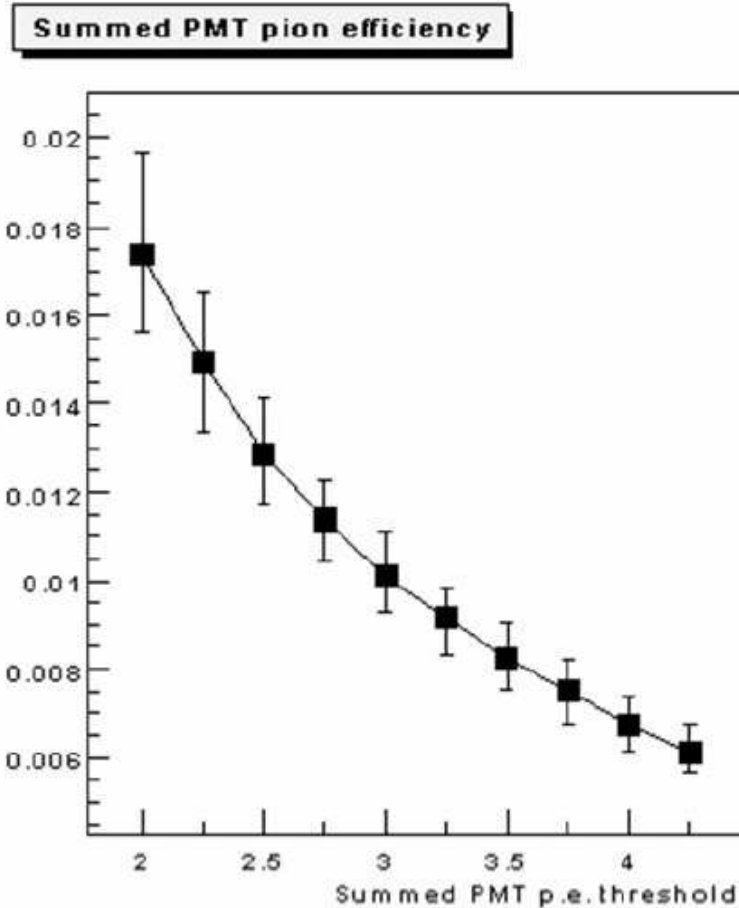


Figure 4.6: NA test Cherenkov results for pion rejection using the TRIUMF test beam.

in Table 4.1, will provide positional and angular tracking of particles. The events in the chamber will be recorded by VME F1 TDC logic modules which are also being used by the HKS experiment. These F1 TDCs are multi-hit TDCs with 1 microsecond full scale range. The G0 trigger will be used as a common stop signal for the chamber electronics and a scintillating detector will be placed in front of the chamber to serve as a timing reference.

A Monte Carlo simulation of the chamber response has been performed using GEANT (see Fig. 4.11); a 10 fold increase in resolution for elastic/inelastic separation and background measurement is expected over the standard setup. This will provide an opportunity to measure backgrounds and coincidence response during the commissioning phase of the experiment. The detectors will be removed during standard running to allow for higher beam currents, but could be reinstalled if additional studies are necessary.

4.2 Electronics

As in the case of the forward angle measurements the four French octants will be instrumented using electronics developed at IPN-Orsay (DMCH-16X boards, based on flash-TDC

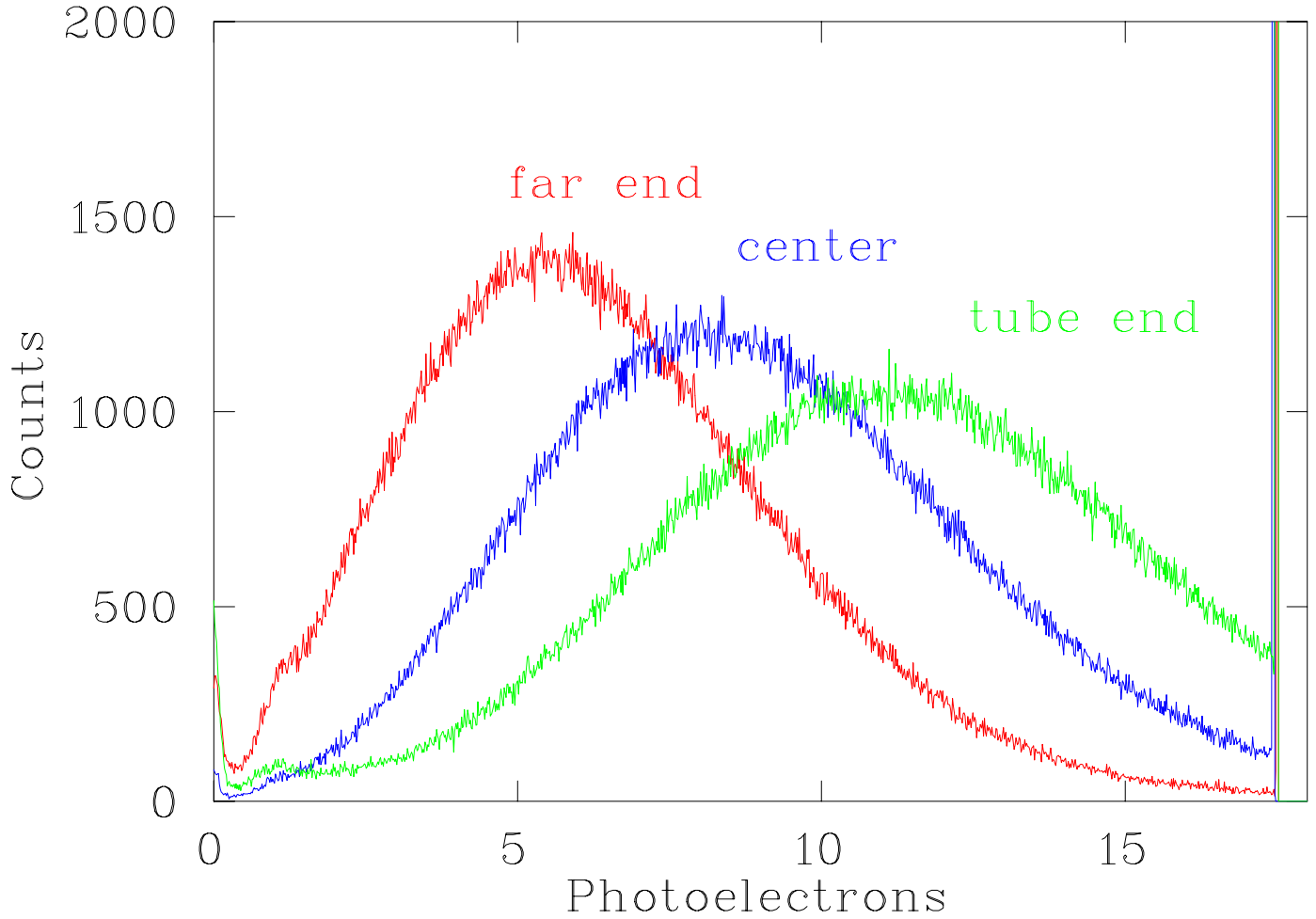


Figure 4.7: NA full-sized prototype Cherenkov results using the TRIUMF test beam.

Table 4.1: HKS Drift Chamber Specifications

Geometrical parameters	
Dimensions (L×W×T)	59.25" × 22.75" × 3"
Active Region	48.2" × 12"
Wire Plane Configuration	U, U', X, X', V, V'
Position and Angular Resolution	
Position(X)	162 μm (rms)
Position(Y)	163 μm (rms)
Angular	~ 2.5 mrad
Operational Parameters	
Operational HV	1970 V
Threshold	3.0 V
Gas content	Argon/Ethane 50:50 mixture
Gas Pressure	~ 16 psi



Figure 4.8: Photograph of the first production French Cherenkov detector.

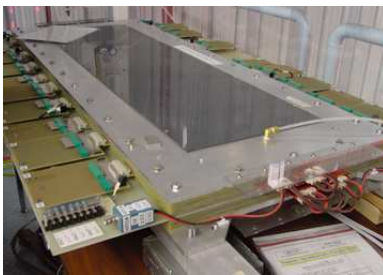


Figure 4.9: HKS Driftchamber Photograph in Cleanroom

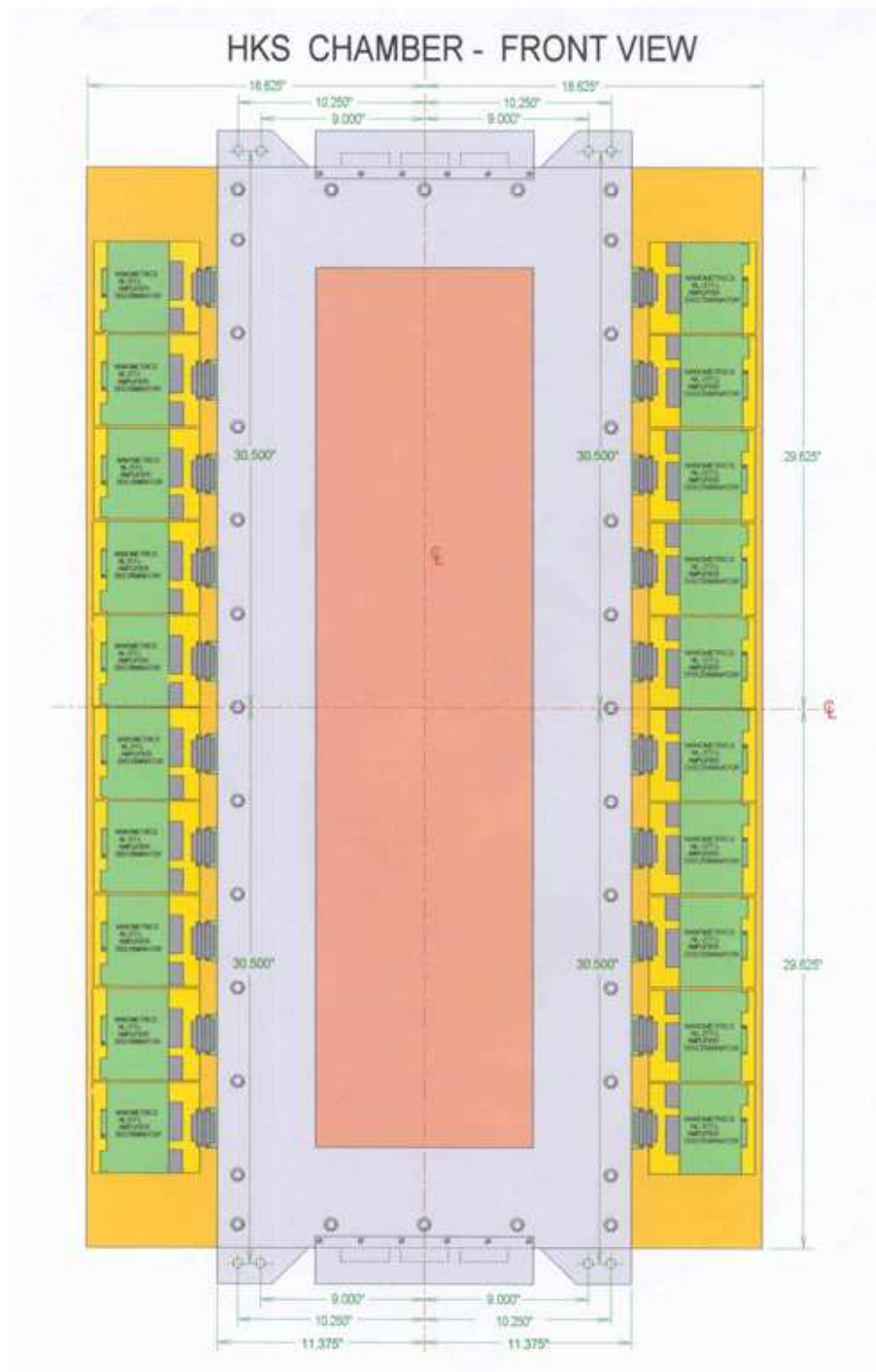


Figure 4.10: HKS Drift chamber technical drawing

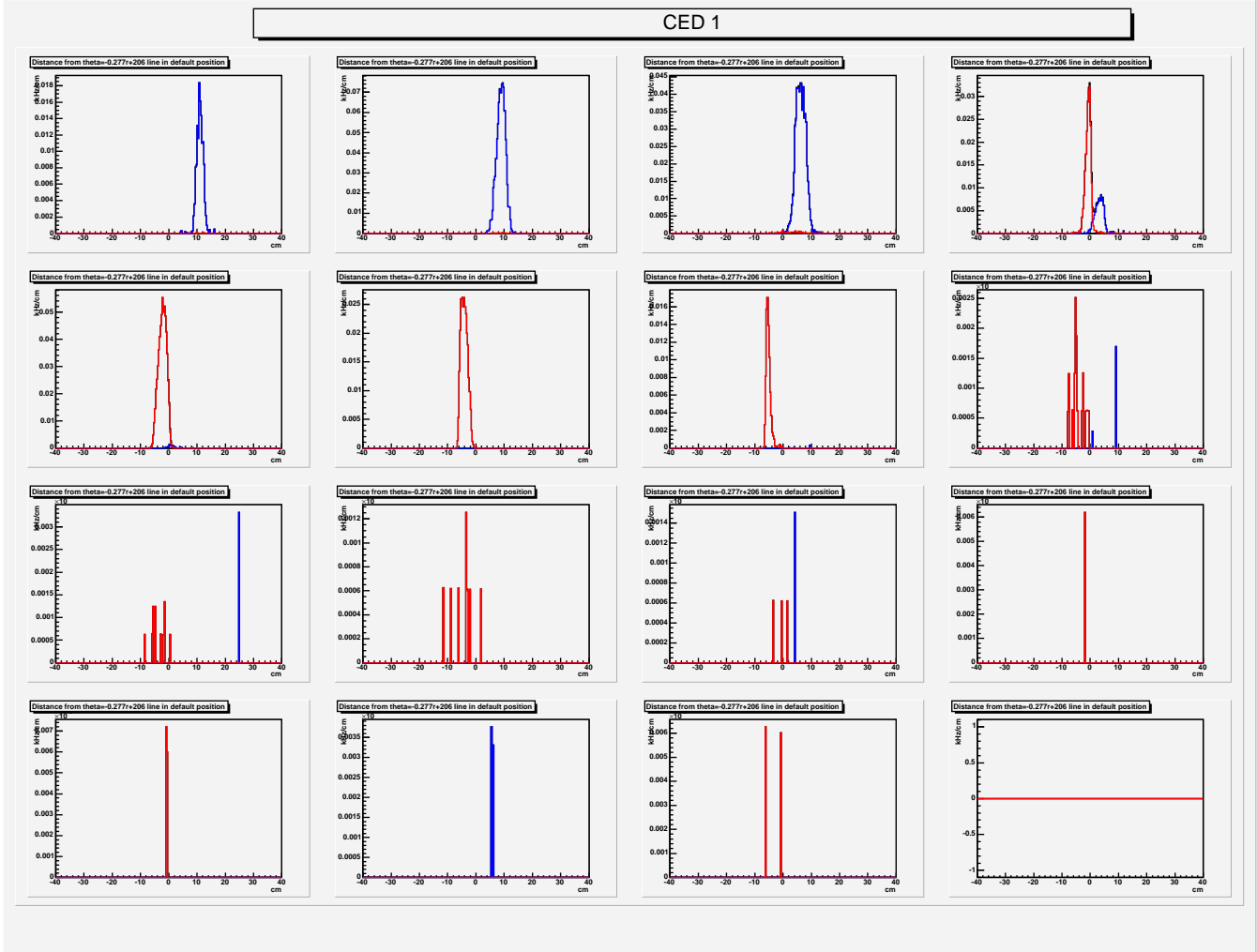


Figure 4.11: Plot of simulated drift chamber yield vs theta for CED 1. Each separate plot represents one FPD (1-16) coincident with CED1. The typical width of the shown peaks is 26 mrad. The red lines correspond to elastic electrons, while the blue lines correspond to inelastic electrons.

and DSP technology), while the North American octants will be instrumented with the relevant parts of the original Latching Time Digitizer (LTD) design. In particular, the DSP histogramming and scaler recording of events, respectively, of the two systems will be utilized. Additionally, all the PMT/base assemblies and associated power supplies used for the backing scintillator array for the FPDs will be used for the CEDs, and all of the instrumentation for the backing array (e.g., analog splitters, constant fraction discriminators, mean timers, and ADC and TDC channels for the monitoring electronics) is also available for the CED array.

The philosophy of the backward-angle electronics design is based in large part on the fact that the electrons being detected ($E_{scattered} \geq 200$ MeV) are all moving with approximately the same velocity, and therefore have a well defined flight time for each CED and each FPD. This is shown in Figures 4.12 and 4.13, where we plot the flight time from the target

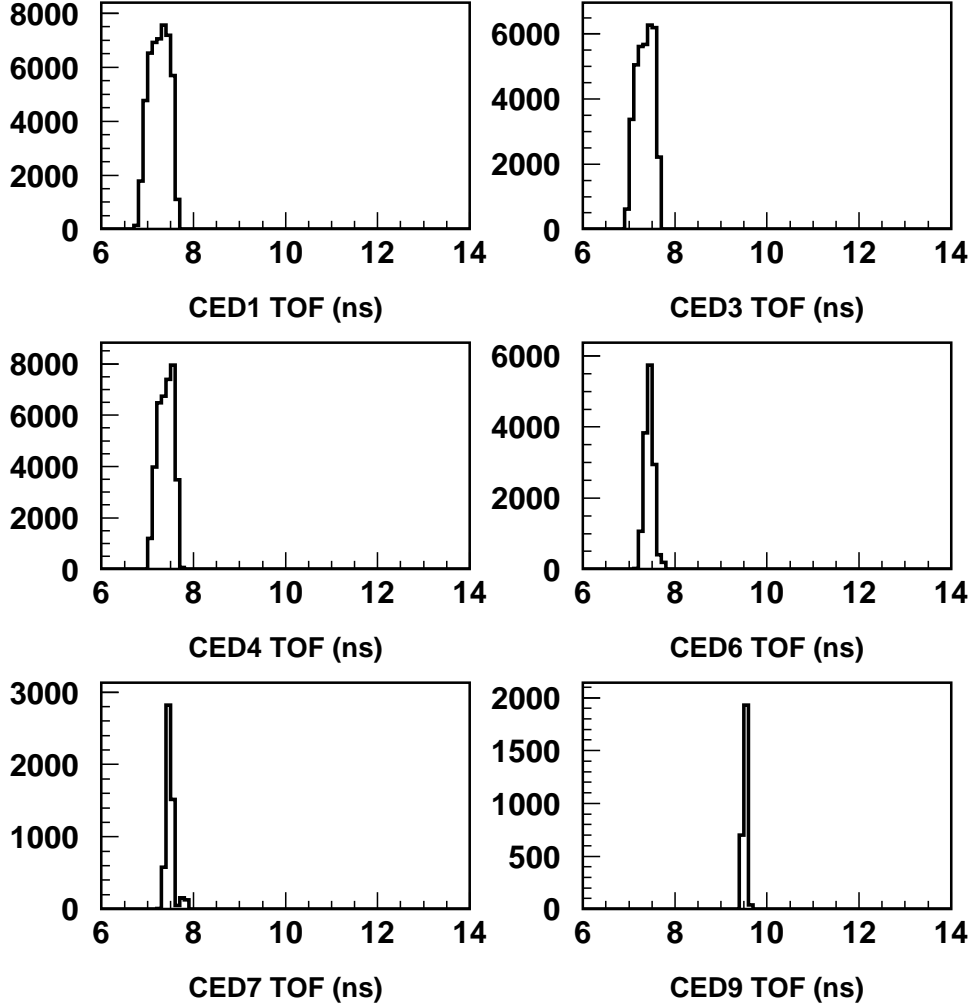


Figure 4.12: Flight times for electrons from the target to selected CEDs.

to selected CEDs and FPDs, respectively. There is a relatively tight time correlation between any CED/FPD pair. Consequently, the use of fast Programmable Logic Devices (PLDs) can provide hardware coincidences which can significantly reduce time uncorrelated backgrounds.

We have been able to use this relatively tight timing to make an important change to the front end of the electronics as compared with the original backward angle proposal. In order to take advantage of the more straightforward accelerator operation* and the possibility of higher beam currents, the standard 499 MHz pulse structure will be adopted for the backward angle measurements. Therefore, instead of using our beam pickoff signal as the primary electronics trigger, the mean-timer outputs of the CEDs for a given octant will be ORed together and ANDed with the ORed outputs of the FPDs for the same octant. The maximum total real rates per octant are shown in Table 4.2. Even with background rates

*The key operational difference for the accelerator is the reduced bunch charge allowing the prebuncher to be run at lower fields, etc.

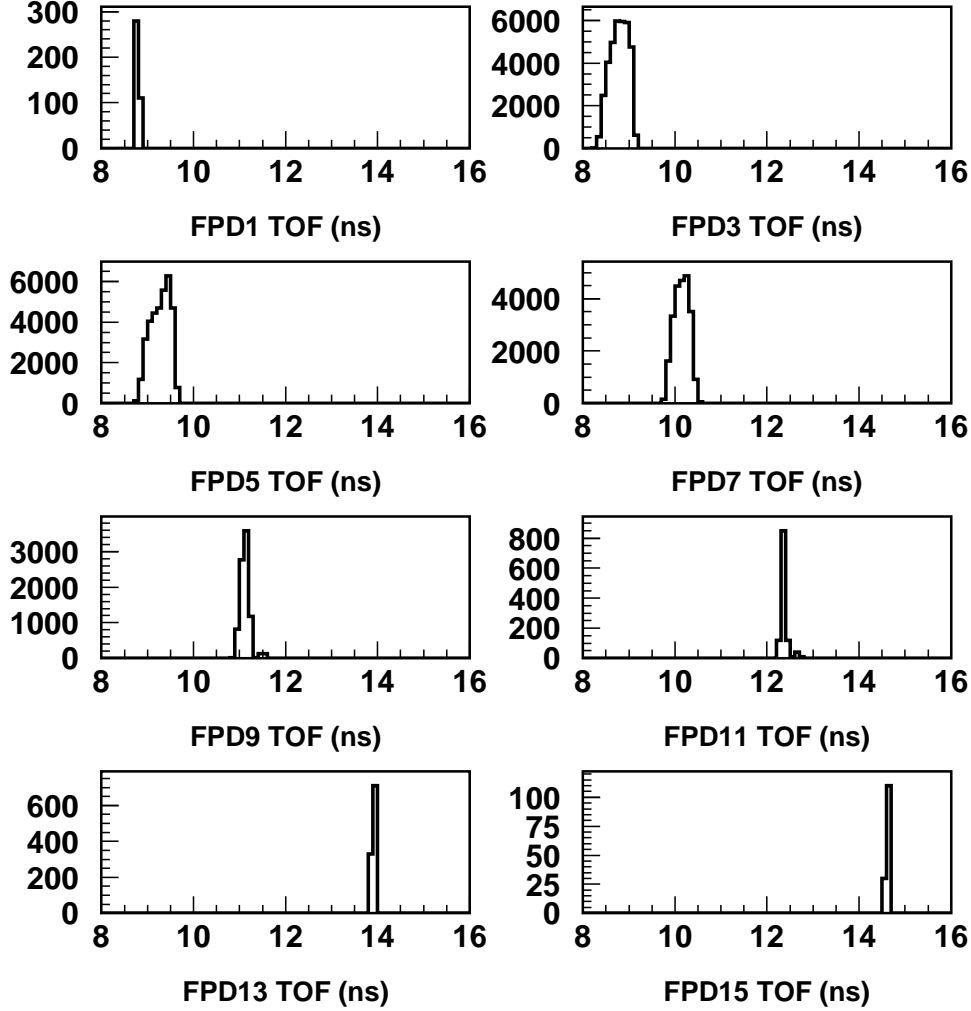


Figure 4.13: Flight times for electrons from the target to selected FPDs.

in each CED and FPD of 500 kHz (maximum of background rates observed in forward angle run), the random coincidence rate per octant is only about 500 kHz (assuming 20 ns gates). Therefore with a total maximum trigger rate of order 1.7 MHz, the deadtime at the trigger level will only be 3%. Commercial electronics will be used to generate these trigger signals.

Target	E (GeV)	Rate (MHz)
^2H	0.424	1.18
^2H	0.585	0.58
^2H	0.799	0.39

Table 4.2: Approximate real rates *per octant* for LD₂ running including elastic electrons, inelastic electrons, pions and muons. Rate calculations for the proposed beam energy of 0.360 GeV have not yet been performed, but they are not expected to be substantially different.

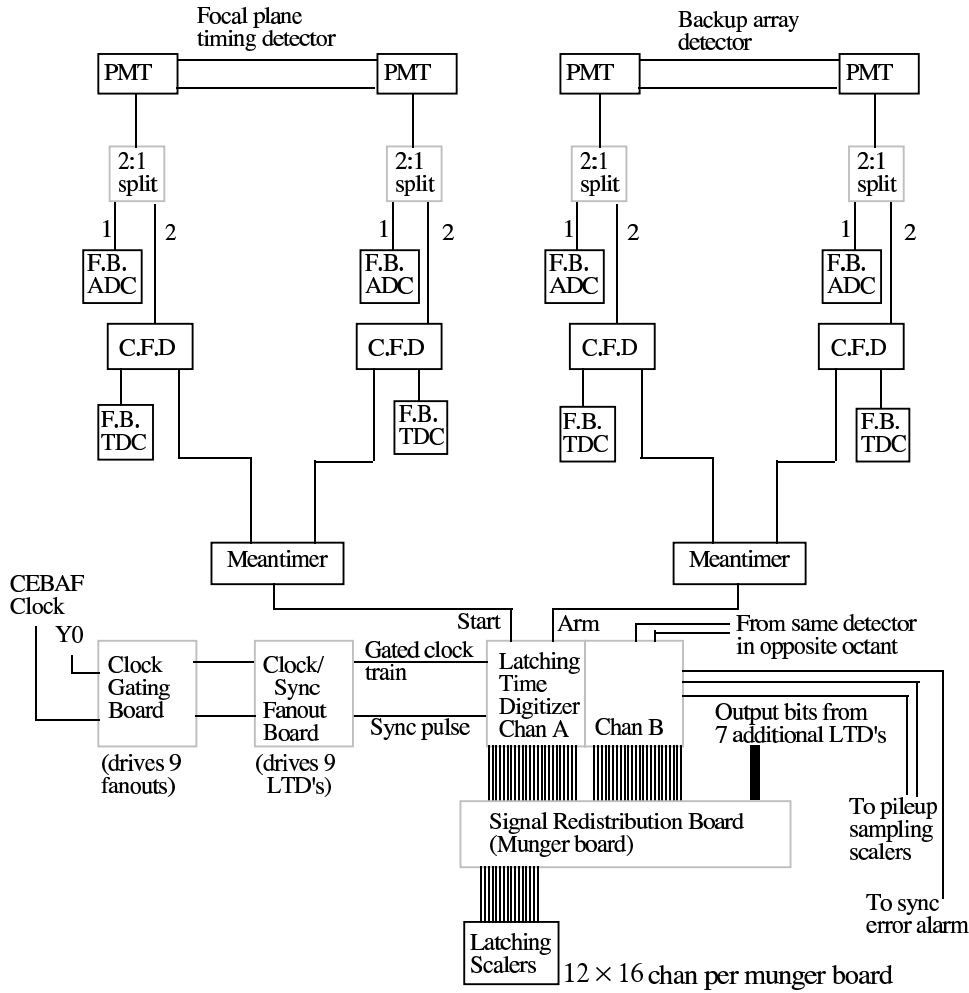


Figure 4.14: Electronics block diagram for the forward-angle running mode for the North American octants.

The North American electronics chain for forward-angle measurements is shown schematically in Figure 4.14. For the backward-angle measurements, the PMT's for the FPD backing detector array will be attached to the CEDs, and the LTD's and "munger" redistribution boards will be replaced by custom logic circuitry developed at Louisiana Tech. Thus, the input to this new logic circuitry is the output of the mean timers for both the FPDs and CEDs, a discriminated signal from the Cherenkov detector, and the main trigger signal as described above. The output of this new circuitry is sent to the latching scalers to count the number of coincidences between detectors in the CED array and those in the FPD array.

Construction and testing of the coincidence logic circuitry for the North American octants is complete. It involves the use of PLDs mentioned above, programmed to implement all the logic associated with the CED-FPD coincidences; the handling of "multiple hit" events (where more than one CED or more than one FPD fires for a given trigger); and dead time monitoring. The trigger pulse can provide a sufficiently small time window to enable

the CED-FPD coincidences at the correct time of electron arrival at these detectors. The logic signal from the Cherenkov detector, which signifies that it was in fact an electron which fired both the CED and FPD involved in the coincidence, will be used to enable a latch which allows the coincidence information to be sent to the scaler modules. Additional counting of CED and FPD singles rates, with various combinations of multiple hit logic and Cherenkov signals included, will be used for an estimate of the front end electronics dead time.

In the final configuration, a total of five boards will be needed per octant: one to handle the coincidence logic encoding; one to handle the multiple hit, Cherenkov, and dead time information; and three to handle TTL-ECL conversion to provide the appropriate level required by the latching scalars. All of the boards are housed in a custom VME chassis which provides the necessary power and common ground to each.

Nearly identical logic and overall philosophy will be used for the French electronics. For one octant, the front end instrumentation (discrimination and mean-timing) will be handled by two DMCH-16X boards. The meantimed outputs, available on the front panel, will be sent to a CED-FPD coincidence module (designed by the Grenoble group). A schematic of the French electronics chain for the backward angle measurements is shown in Figure 4.15.

The coincidence board contains all PLDs and scalars needed for the counting of individual coincidences between each CED and each FPD. As in the North American design, the CED-FPD coincidences will be allowed during a short time window initiated by the trigger, and the Cherenkov counter will provide an enable signal for the counting. Also as in the North American design, additional counting associated with the singles rates in the CEDs and FPDs will be used for the estimate of the number of multiple hit events and for deadtime monitoring. In addition to the singles counting available in the coincidence board, the DMCH-16X modules also provide the time of flight information for the individual CEDs and FPDs, which can be used for an accurate estimate of the number of lost events due to the deadtime of the front end electronics.

One CED-FPD coincidence module will be able to handle two octants. For the four french octants, the VXI crate will therefore support eight DMCH-16X and two CED-FPD coincidence modules.

A significant improvement in the electronics, relating to pion backgrounds, has been made since our last proposal. For both the French and NA electronics, CED-FPD rates will be counted in coincidence and in anti-coincidence with the aerogel Cherenkov counter signals. Those combinations in coincidence with the Cherenkov counter would signify scattered electrons, while anti-coincidence would signify pion background. This increased capability will allow the extraction of parity-violating asymmetries for the pion backgrounds simultaneously with the elastic electron signal. Thus pion backgrounds will not only be suppressed in the Cherenkov coincidence requirement, but will be characterized in detail. The pion signal itself is of interest, relating to potentially large asymmetries in photoproduction of pions on the Delta resonance [99, 100].

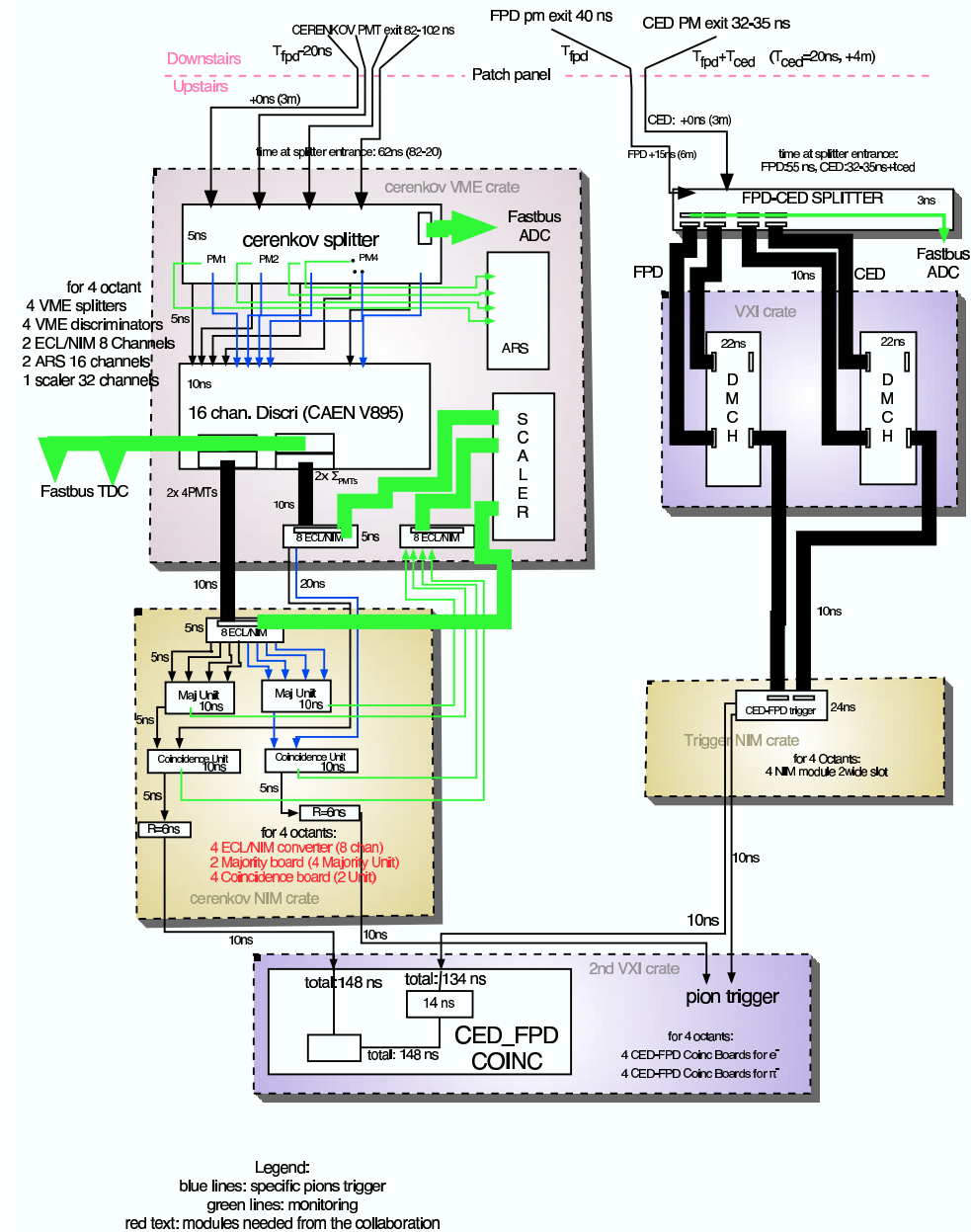


Figure 4.15: Electronics block diagram for the backward-angle running mode for the French octants.

4.3 DAQ

The data acquisition requirements for the backward-angle running configuration are almost identical to those for forward-angle running. Only small differences in the data stream will be present for both the North American and French octants.

Generally, the data stream will consist of two different types of events: high statistics data counting all particles detected within each $\frac{1}{30}$ s macropulse period and read out at 30 Hz after being latched during a $\sim 200 \mu\text{s}$ interval during which time the helicity Pockels

cell may change polarity; and low statistics monitoring data including ADC and TDC spectra for each PMT on each detector read out at ~ 1 kHz. This is true for both forward and backward running configurations. There will in fact be less data arising from the monitoring electronics in the backward-angle running than in the forward-angle mode, simply because there are only 9 CEDs instrumented per octant (corresponding to 18 ADC and TDC spectra per octant) in contrast to 16 FPD backing detectors instrumented per octant in the forward-angle configuration. The small differences arising between the two running modes occur in the high statistics data only for the French octants, with no difference in the data streams for these events for the North American octants between the forward and backward running modes. To understand these differences, we review the data obtained for both types of instrumentation, and for both running configurations.

In the North American octants, the LTD boards discussed in the previous section are designed to separate the data obtained from each FPD for the forward-angle running into time bins within the 32 ns period between successive beam bursts. High speed scalers will then be used to store the time spectra. For the backward-angle running, no time encoding is necessary because all backward scattered electrons are moving with approximately the same speed, and it is impossible to separate elastically scattered electrons based on time of flight information. Thus, of the available scaler channels that were used for time bin counting during the forward-angle running, some will be used to count the number of coincidences between each CED and each FPD, and the remaining scaler channels will be used to count singles rates in each CED and FPD, with various constraints of multiple hits and Cherenkov detector firing. Different CED-FPD combinations correspond to different electron momentum, which allows an identification of the elastically and inelastically scattered electrons independently.

In the French octants, the high statistics data for the forward-angle measurements are sorted into time of flight histograms directly on the DMCH-16X boards through the use of flash TDC's and DSP's. These histograms are then sent into the data stream during the data read out every $\frac{1}{30}$ s through the VXI crate backplane. For the backward-angle measurement, the main information will come from scalers containing the CED-FPD coincidences and CED and FPD singles rates with multiple hit and Cherenkov constraints. The number of scalers needed is about the same as in the North American scheme.

Although there will be very little change in the data acquisition software for the backward angle running, there will be some change required to the analysis software. In the forward mode, the primary analysis involves construction of time-of-flight histograms from the North American scaler electronics or from the Orsay TDC data. Asymmetries are calculated for each detector from identification of the proton timing peak in the TOF spectrum. Since in the backward mode, in both the North American and French octants, the primary means of identifying events will now be scalers counting yields in each FPD/CED pair, asymmetries for each FPD/CED pair will be calculated from the scaler values. The processed data will thus be a two dimensional array of asymmetry values in FPD/CED space. Elastic and inelastic regions in FPD/CED space will be identified from the scaler yields.

4.4 Target

The backward angle running of the G0 experiment will utilize a slightly modified configuration of the liquid hydrogen target that has been used successfully for the forward angle measurements. It is important to note that unlike the spectrometer which is rotated for the backward angle measurement, the target system remains on the upstream side just as it was in the forward measurement. The baseline requirements for the G0 target remain (1) target length of 20 cm, (2) dissipation of heat deposited by 40 μA of electron beam current and (3) operation without introducing uncorrected false asymmetries at a level $> 5\%$ of the overall uncertainty in the measurement ($\Delta A \approx 10^{-8}$ over the entire run for any individual source of false asymmetry). The modifications required for backward angle running are:

- extension of the target support to longitudinally center the target in the magnet in the backward angle orientation (this extension pipe already exists),
- the port for the target service lines needs to be redesigned to accommodate the space constraints associated with the detector support structure,
- connection of gas panel to D₂ supply tank during LD2 runs.

The liquid hydrogen target cell is connected to a cryogenic loop to recirculate and cool the liquid. The hydrogen will be cooled through heat exchange with compressed helium gas. The liquid hydrogen is thus maintained at 20 K and 25 psia (through connection with the ballast tank). When full, the target cryogenic loop plus target cell and manifold will contain 6.6 liters of liquid hydrogen.

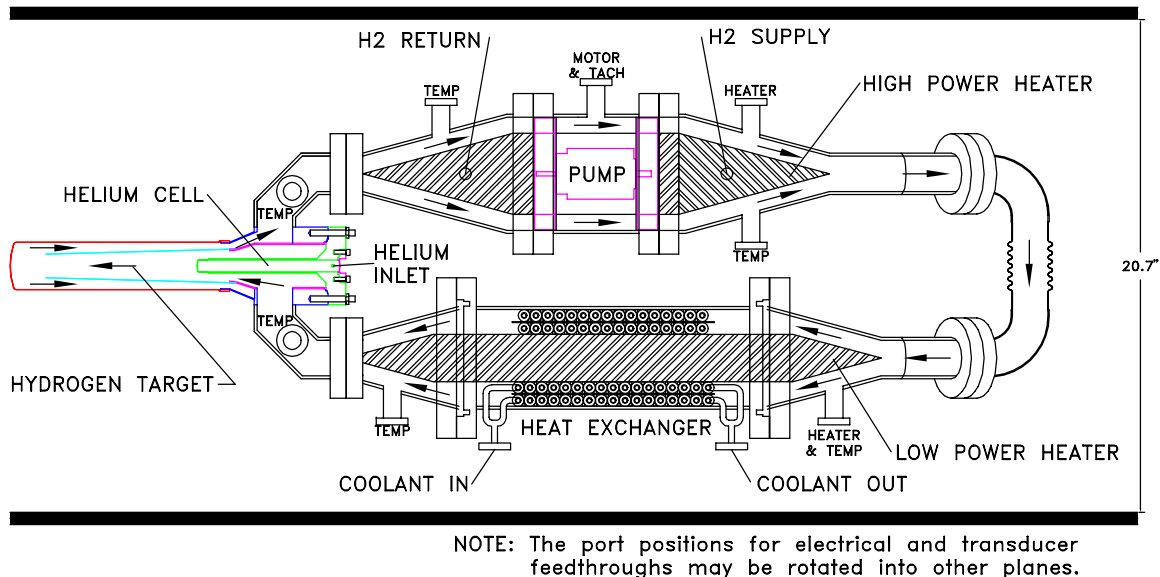


Figure 4.16: Overview of the G0 liquid hydrogen cryotarget. Beam is incident from the right in this view. Exiting scattered electrons of interest emerge at $108^\circ \pm 8^\circ$ with respect to the beam from the hydrogen liquid downstream (left in the figure) of the helium cell.

Figure 4.16 is a scale diagram showing the cryotarget centered within the liquid nitrogen shield of the superconducting magnet. The main components of the cryoloop are a pump for circulating the target fluid, a heat exchanger, the target cell, and a manifold to direct the fluid flow down the center of the target cell and back near the cell walls. The arrows in the figure indicate the direction of fluid flow in the loop.

The helium cell positioned adjacent to and just upstream of the liquid hydrogen cell serves three purposes

- it effectively extends the entrance of the hydrogen cell beyond the manifold so that exiting particles only traverse hydrogen and thin cell walls,
- it insures that the exiting particles encounter a region that is symmetric about the beam axis, and
- it eliminates (to first order) variations in the target thickness with beam position by matching the radius of curvature of the entrance and exit windows of the hydrogen cell.

Thus the target–beam interaction region is designed to be axially symmetric and independent of beam position.

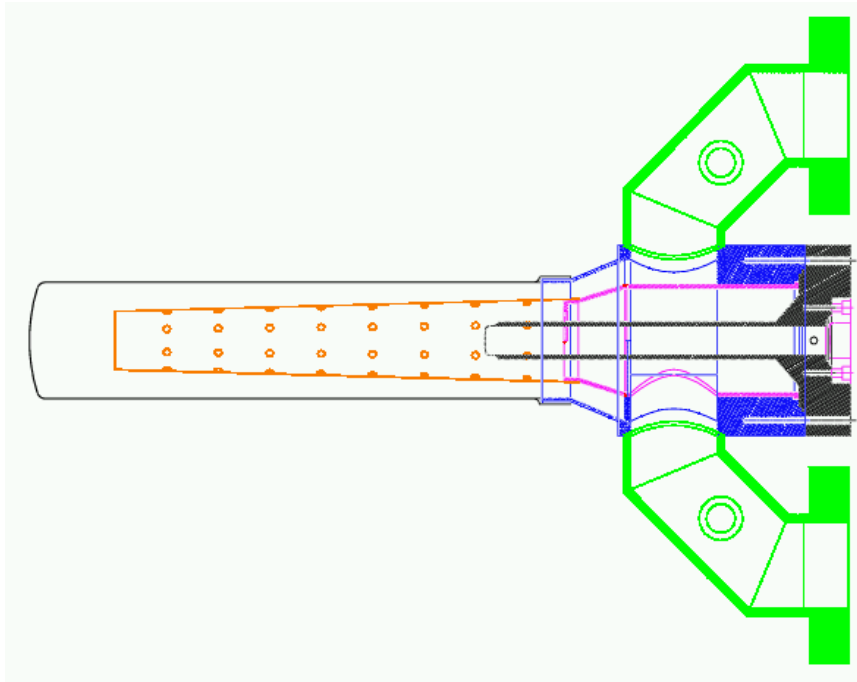


Figure 4.17: Detailed view of the G0 hydrogen target cell, helium cell and manifold. The effective hydrogen target length is 20 cm and the diameter of the outer shell of the target cell is 5 cm. In this view, hydrogen liquid enters in the lower manifold pipe and exits in the upper manifold pipe.

Figure 4.17 shows the details of the target cell and manifold. When the pump is running, the liquid hydrogen flows longitudinally in the same direction as the beam through the inner flow cone and returns through the annulus between the inner cone and the wall of the hydrogen cell. The distance between the exit window of the helium cell and the exit

window of the hydrogen target cell is 20 cm. The holes in the inner cone are essential to prevent collapse of the cone due to Bernoulli pressure; they form an eight-fold symmetric pattern and are aligned with the G0 magnet coils so they are out of the spectrometer acceptance.

The hydrogen target cell consists of a 5 cm diameter tube with a rounded endcap, machined from a solid cylinder of 7075 aluminum. We fabricate the cell by machining the end of the cylinder flat, then pressing it in a form to make the rounded endcap. The radius of curvature of the center of the endcap is 7.6 cm. The outer side wall and endcap are 7.0 ± 0.5 mils thick. To verify that the target cell can withstand the pressure that builds up during target boiloff, each cell is hydrostatically tested to 100 psid before being soldered to the manifold. This is a factor of 2.4 safety margin over the pressure that we calculate the cell would be subjected to in a catastrophic vacuum failure.

The cryogenic loop contains two heaters, one low power and one high power, to regulate the temperature of the liquid hydrogen. These heaters are identical in function to those used in the Hall C liquid hydrogen target. The high power heater will operate at up to 1000 W maximum power with its main function being to compensate for significant reductions in the beam current. The low power internal heater will be used to make relatively small adjustments to the fluid temperature and will be controlled automatically with a commercial temperature controller in a feedback loop with the temperature sensor on the upstream side of the target cell.

The loop contains a vaneaxial pump capable of displacing 4.8 l/s of liquid hydrogen. This corresponds to a mass flow rate of 333 g/s and gives a velocity in the target region of ~ 7 m/s. The pump motor is inside the cryoloop, similar to the design used in the Hall C cryotargets.

It is important to minimize density fluctuations because they introduce statistical fluctuations into the asymmetry that mask the parity violating asymmetry, requiring a longer running time to achieve the same experimental precision. To reduce resistance and maximize the circulating flow rate in the cryogenic loop we have incorporated flow diverter cones at transitions between elements of different diameters.

We expect to be able to run the backward angle measurement at $80 \mu\text{A}$, in part because we will be using the standard 499 MHz pulse structure and in part because of the better-than-expected target performance during the forward angle run. This will help us to reduce the overall uncertainties in extracting the form factors whose uncertainties were dominated by the backward angle statistical precision. We have determined from the forward measurement that the total power handling capability will be more than sufficient for this purpose. In addition, we estimate that the contribution of target density fluctuations to the detector asymmetry widths due to the increased power density will be less than 500 ppm even for an $80 \mu\text{A}$ beam current, as compared with the minimum statistical width of about 5000 ppm.

4.5 Infrastructure

Since the back-angle configuration has been planned for since the beginning of the G^0 project, many of the infrastructure and installation aspects have already been thought out or implemented. The main change is that the SMS must be moved downstream of the ferris wheel, and the SMS/ferris wheel structure must be rotated 180° . SMS rails to accommodate this configuration change have already been installed in the hall. The ferris wheel platform has been built to accommodate a corresponding (smaller) downstream shift in the ferris wheel location. These rotations were made in August-September 2004.

At the time of the configuration change, the lead/polyboron beamline shielding cylinder was removed from the ferris wheel. It is not needed in the back-angle experiment. Lead shielding will also be removed from the SMS downstream head. The ferris wheel has been rotated and the CED/Cherenkov assemblies will be added. The target service module will mate with the upstream flange of the ferris wheel, moving the target center about 3 m downstream relative to the forward-angle configuration.

New beamline spool pieces will be required. The downstream beam dump shielding will have to be relocated closer to the dump tunnel entrance. Techniques for placing shielding blocks in this location, outside the nominal crane radius, have already been developed and are in use.

The Møller polarimeter will need to be changed to accommodate the lower energies used in this experiment. A similar change was made successfully in the spring 2001 G_E^n experiment to accommodate Møller measurements at 0.884 GeV by moving the Møller Q1 about 6" upstream. Møller operation at 0.360 GeV will require a further upstream move; optics calculations for this configuration have been completed.

We do not expect significant changes in cryogenic services or cabling. The cabling will probably be re-routed overhead to accommodate a somewhat longer distance to the magnet and detectors. The cryogenic services for the target will have to be supported in a somewhat different way because they are now some distance from the magnet to which they used to be affixed, but no significant problems are foreseen.

The collaboration has done extensive simulations of the backgrounds generated in the beampipe near the target region. The goal is to reduce the backgrounds to a level to insure that the anode currents in the CED and FPD photomultiplier tubes are kept below $40 \mu\text{A}$ at the full operating beam current of $80 \mu\text{A}$. These simulations led to the design of a cylindrical lead shielding insert that will be incorporated downstream of the target. Also, some additional shielding at the upstream side of the superconducting magnet cryostat will be added.

The requirements on helicity-correlated beam properties for the back-angle running are somewhat less stringent than those that were already achieved for the forward angle running. This is due to two facts. The sensitivities to beam motion in the backward mode are estimated to be comparable to or smaller than the sensitivities in the forward mode. The smallest measured asymmetries in the backward mode are expected to be about -18 ppm, compared to -2 ppm for the forward angle running. So false asymmetries have a smaller

fractional contribution to the backangle running. Therefore, the helicity-correlated beam properties already achieved during forward angle running (see Table 8.1) are more than sufficient for back angle running. It is worth remembering, though, that achieving those specifications required regular calibration and tuning of the various feedback circuits. So the collaboration supports and is participating in the continued efforts of the accelerator division to improve the “adiabatic damping” properties of the accelerator tune. This will allow for the helicity-correlated position differences to be reduced “naturally” and take some of the performance load off of the feedback circuits.

5 Organization and Schedule

As indicated above, the new construction for the backward angle measurements, including the CEDs, Cherenkov detectors, CED/FPD coincidence electronics, and target modifications, has been completed. Assembly and testing of all components is being finalized. The spectrometer turnaround has been completed. Installation is expected to begin in early September in preparation for the start of running in December. These activities are being funded within the envelope of the original G0 project, with important additional support for the Cherenkov construction from the French (CNRS) and Canadian (NSERC) funding agencies.

6 Expected Results and Beam Time Request

6.1 Expected Results

This section presents the expected results from the complete program of proposed G0 running - forward and backward hydrogen/deuterium measurements.

For the backward measurements, we have investigated in general the optimum split of time between hydrogen and deuterium running at each momentum transfer point. We show the results of this study in Figure 6.1 for the originally proposed 0.3 GeV^2 point (replaced by the presently proposed point at $Q^2 = 0.23 \text{ GeV}^2$); the other momentum transfer points show a similar dependence. We conclude that an even split of running time between hydrogen and deuterium is a reasonable compromise. The even split of time for the hydrogen and deuterium running balances the uncertainties in G_E^s and G_M^s (which are minimized with about 60% of the running time on hydrogen) against those in $G_A^e(T = 1)$, which are minimized at a small fraction of hydrogen running. This is the plan for the first measurement at $Q^2 = 0.8 \text{ GeV}^2$ to begin in December 2005; the split in subsequent measurements will depend on the results for G_A^e at this momentum transfer as discussed above.

In our error estimates, we make two different beam time assumptions. For the $Q^2 = 0.23 \text{ GeV}^2$ point, we assume 50 days, all on hydrogen as explained in the Summary. For $Q^2 = 0.48 \text{ GeV}^2$, we assume 30 days of running time for each of the hydrogen and deuterium targets. In all cases we take the beam current to be $80 \mu\text{A}$ with 75% polarization. The assumptions we make about the uncertainties in the form factors and other quantities that go into the asymmetry calculation are summarized in Table 6.1. The results for the two proposed values of Q^2 are shown in Figs. 6.2 and 6.3. The expected errors on the separated form factors are summarized in Table 6.2. Figure 6.4 shows the overall uncertainties in G_E^s and G_M^s relative to the overall proton form factors G_E^p and G_M^p . Figure 6.5 (also included as Figure 2.3) shows the uncertainties expected in $G_A^e(T = 1)$ relative to the calculation of Zhu, *et al.* [58].

6.2 Beam Time Request

At this time, we request that the PAC approve 50 beam days (or about 84 calendar days) for the measurement at $Q^2 = 0.23 \text{ GeV}^2$. We further request that the PAC approve an additional 60 beam days for the hydrogen and deuterium measurements at $Q^2 = 0.48 \text{ GeV}^2$ to complete the original G0 program.

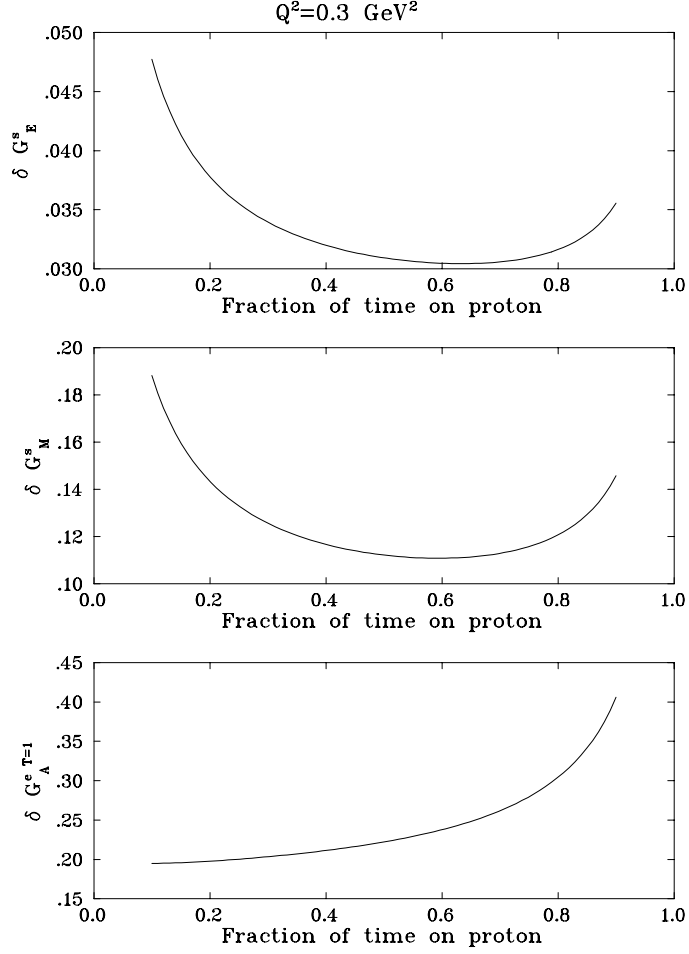


Figure 6.1: Total errors on the separated form factors at $Q^2 = 0.3 \text{ GeV}^2$ as a function of the fraction of the backward angle running time on hydrogen. The proposed measurement will be performed at $Q^2 = 0.23 \text{ GeV}^2$.

Quantity	Uncertainty
$\Delta G_E^p / G_E^p$	0.25-1.25%
$\Delta G_M^p / G_M^p$	1%
$\Delta G_E^n / G_E^n$	5-7.5%
$\Delta G_M^n / G_M^n$	1%
$\Delta P_b / P_b$	2%
$\Delta Q^2 / Q^2$	1%
$\Delta G_A^e(T=0)$.11
ΔR_V^p	.033
ΔR_V^n	.0004

Table 6.1: Uncertainties assumed for the quantities in the asymmetry expression. The electromagnetic form factor uncertainties are based on those of Kelly [8].

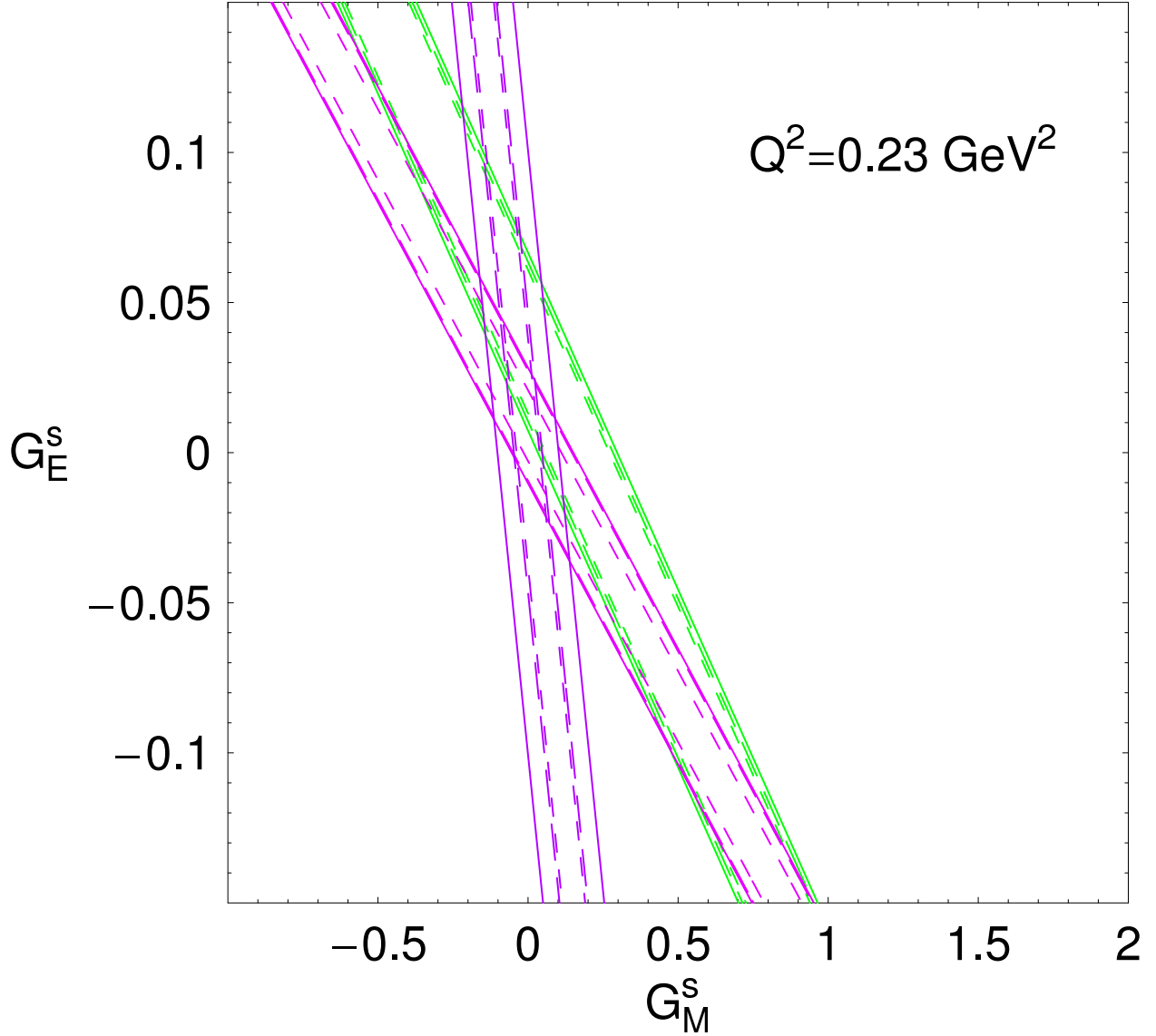


Figure 6.2: Data at $Q^2 = 0.23 \text{ GeV}^2$: magenta G0 forward angle [1], green PVA4 [7] and purple G0 backward angle projected. Uncertainties: short dashed - statistical, long dashed - statistical plus systematic, solid - statistical plus systematic plus model. The projected G0 backward angle band is drawn centered on the point $G_M^s = G_E^s = 0$.

$Q^2 \text{ (GeV}^2\text{)}$	ΔG_E^s	ΔG_M^s	$\Delta G_A^e(T=1)$
0.23	0.026	0.098	—
0.48	0.048	0.058	0.158
0.8	0.051	0.040	0.133

Table 6.2: Expected errors on the separated form factors. These include all statistical and systematic errors. The point at $Q^2 = 0.8 \text{ GeV}^2$ is already approved.

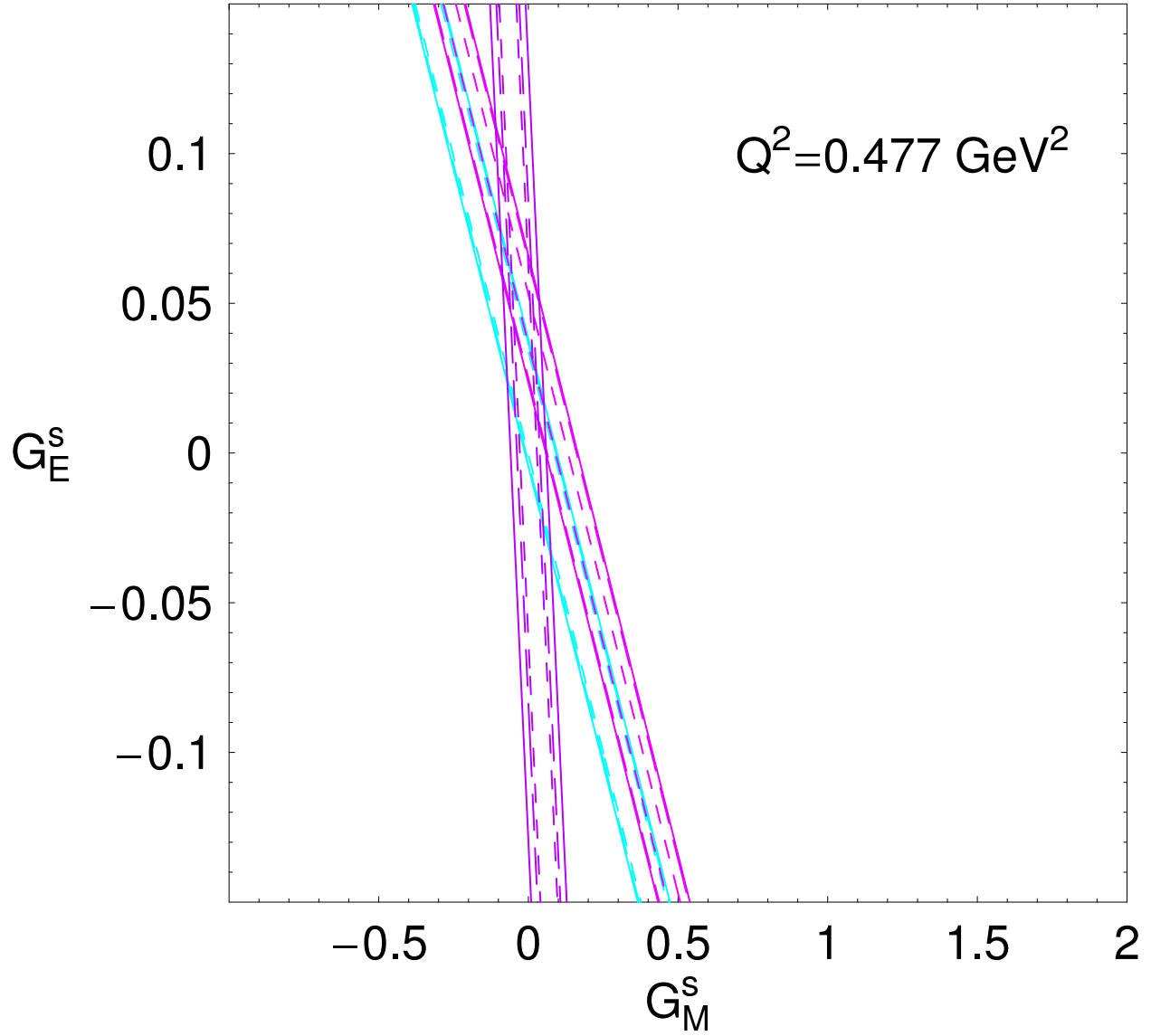


Figure 6.3: Data at $Q^2 = 0.477 \text{ GeV}^2$: magenta G0 forward angle [1], cyan HAPPEX [2] and purple G0 backward angle projected. Uncertainties: short dashed - statistical, long dashed - statistical plus systematic, solid - statistical plus systematic plus model. The projected G0 backward angle band is drawn centered on the point $G_M^s = G_E^s = 0$.

Quantity	0.23 GeV ²	0.48 GeV ²
A_f	.018	.042
A_b	.008	.014
A_d	—	.007
G_E^p	.002	.003
G_M^p	.002	.002
G_E^n	.004	.004
G_M^n	.000	.001
Q^2	.006	.008
P_e	.008	.013
<i>others</i>	.005	.004
total	.026	.048

Table 6.3: Contributions to the error on G_E^s . The entries for Q^2 and P_e include the errors for all three measurements(f, b, d) added in quadrature. The “others” entry includes $G_A^e(T = 0), R_V^p, R_V^n$. For the $Q^2 = 0.23$ GeV² point, it is assumed that all the running is on hydrogen and the error on on $G_A^e(T = 1)$ is taken to be ± 0.20 , which contributes an error to G_E^s of ± 0.011 .

Quantity	0.23 GeV ²	0.48 GeV ²
A_f	.018	.007
A_b	.043	.035
A_d	—	.023
G_E^p	.007	.000
G_M^p	.008	.004
G_E^n	.000	.001
G_M^n	.011	.004
Q^2	.022	.018
P_e	.029	.032
<i>others</i>	.027	.011
total	.098	.058

Table 6.4: Contributions to the error on G_M^s . The entries for Q^2 and P_e include the errors for all three measurements(f, b, d) added in quadrature. The “others” entry includes $G_A^e(T = 0), R_V^p, R_V^n$. For the $Q^2 = 0.23$ GeV² point, it is assumed that all the running is on hydrogen and the error on on $G_A^e(T = 1)$ is taken to be ± 0.20 , which contributes an error to G_M^s of ± 0.072 .

Quantity	0.48 GeV ²
A_f	.055
A_b	.011
A_d	.094
G_E^p	.007
G_M^p	.009
G_E^n	.006
G_M^n	.011
Q^2	.056
P_e	.096
<i>others</i>	.010
total	.158

Table 6.5: Contributions to the error on $G_A^e(T = 1)$. The entries for Q^2 and P_e include the errors for all three measurements (f, b, d) added in quadrature. The “others” entry includes $G_A^e(T = 0), R_V^p, R_V^n$.

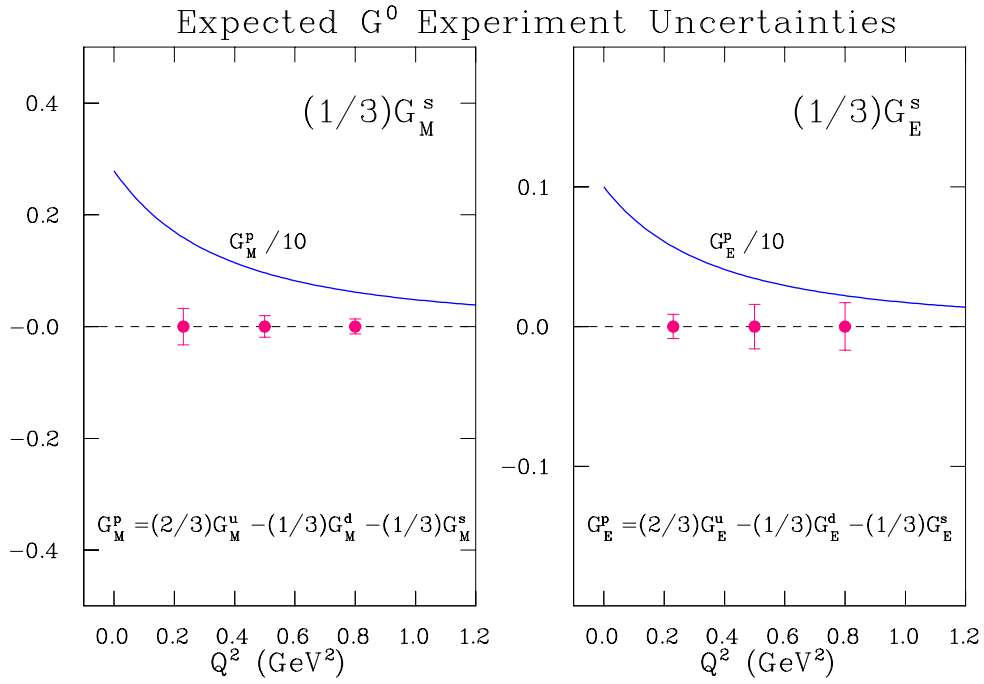


Figure 6.4: Expected errors on the contribution of the strange form factors to the electric and magnetic proton form factors.

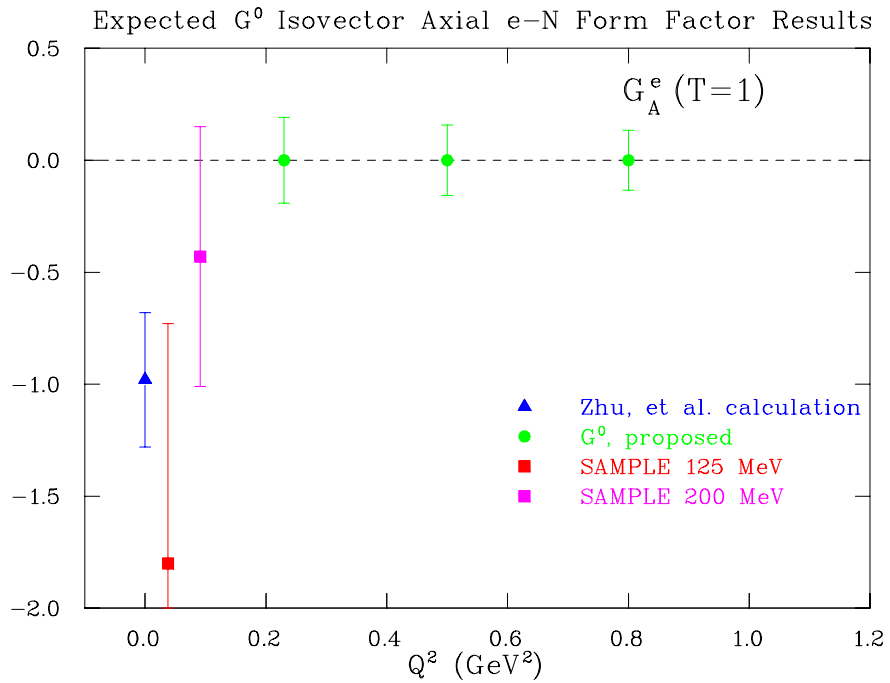


Figure 6.5: Expected errors on the isovector axial e-N form factor. (Note: The point at the lowest $Q^2 = 0.23 \text{ GeV}^2$ is the error that would be obtained with 700 hours (30 days) of running on deuterium at the lowest beam energy of 0.360 GeV. The currently proposed plan calls for no deuterium running at the lowest beam energy, so this data point would not be obtained in that plan.)

References

- [1] D. Armstrong et al. (G0 Collaboration), submitted to Phys. Rev. Lett., arXiv nucl-ex/0506021.
- [2] K. A. Aniol *et al.* (HAPPEX Collaboration), *Phys. Rev. Lett.* **82**, 1096 (1999), and K. A. Aniol *et al.* (HAPPEX Collaboration), *Phys. Rev. C* **69**, 065501 (2004).
- [3] K. A. Aniol, *et al.* (HAPPEX Collaboration), submitted to Phys. Rev. Lett., arXiv nucl-ex/0506011.
- [4] D. T. Spayde, *et al.* (SAMPLE Collaboration), *Phys. Lett. B* **583**, 79 (2004).
- [5] F. E. Maas, *et al.* (PVA4 Collaboration), *Phys. Rev. Lett.* **94**, 152001 (2005).
- [6] K. A. Aniol, *et al.* (HAPPEX Collaboration), submitted to Phys. Rev. Lett., arXiv nucl-ex/0506010.
- [7] F. E. Maas, *et al.* (PVA4 Collaboration), *Phys. Rev. Lett.* **93**, 022002 (2004).
- [8] J. J. Kelly, *Phys. Rev. C* **70**, 068202 (2004).
- [9] J. Friedrich and T. Walcher, *Eur. Phys. J. A* **17**, 607 (2003).
- [10] J. Arrington, *Phys. Rev. C* **69**, 022201 (2004).
- [11] D. Leinweber, *et al.*, *Phys. Rev. Lett.* **94**, 212001 (2005).
- [12] S. Eidelman, *et al.*, *Phys. Lett. B* **592**, 1 (2004).
- [13] V. E. Lyubovitskij, *et al.*, *Phys. Rev. C* **66**, 055204 (2002).
- [14] R. Lewis, *et al.* *Phys. Rev. D* **67**, 013003 (2003).
- [15] A. Silva, *et al.* *Phys. Rev. D* **65**, 014016 (2001).
- [16] K. S. Kumar and P. A. Souder, *Prog. Part. Nucl. Phys.*, **45**, S333(2000).
- [17] D. H Beck and R. D. McKeown, *Ann. Rev. Nucl. Part. Sci.* **51** 189 (2001).
- [18] E. J. Beise, M. L. Pitt and D. P. Spayde, *Prog. Part. Nucl. Phys.*, **54**, 289 (2005).
- [19] D. Kaplan and A. Manohar, *Nucl. Phys. B* **310**, 527 (1988).
- [20] R. D. McKeown, *Phys. Lett.* **B219**, 140 (1989).
- [21] D. H Beck, *Phys. Rev.* **D39**, 3248 (1989).
- [22] M. J. Musolf, *et al.*, *Phys. Rep.* **239** 1 (1994).
- [23] M. J. Musolf and B. R. Holstein, *Phys. Lett.* **B242**, 461 (1990).
- [24] E. Hadjimichael, G. I. Poulis, and T. W. Donnelly, *Phys. Rev.* **C45**, 2666 (1992).
- [25] L. Diaconescu, R. Schiavilla, and U. van Kolck, *Phys. Rev.* **C6304**, 4007 (2001).
- [26] C. Liu, G. Prezeau and M. Ramsey-Musolf, *Phys. Rev.* **C67** 035501 (2003).
- [27] T. Ito, *et al.*, *Phys. Rev. Lett.* **92** 102003 (2004).
- [28] Particle Data Group, *Euro. Phys. J.* **C54**, 1 (2000).
- [29] H. Gao, *Int. J. Mod. Phys. E* **12**, 1 (2003).
- [30] G. A. Miller, *Phys. Rev.* **C57**, 1492 (1998).

- [31] W. J. Marciano and A. Sirlin, *Phys. Rev.* **D27**, 552 (1983); W. J. Marciano and A. Sirlin, *Phys. Rev.* **D29**, 75 (1984).
- [32] M. J. Musolf and M. Burkardt, *Z. Phys.* C61, 433 (1994).
- [33] W. Koepf, E. M. Henley, and S. J. Pollock, *Phys. Lett.* B288 11 (1992).
- [34] B. R. Holstein in *Proceedings of the Caltech Workshop on Parity Violation in Electron Scattering*, E. J. Beise and R. D. McKeown, Eds., World Scientific, 27 (1990).
- [35] H. Ito, *Phys. Rev.* C52, R1750 (1995).
- [36] P. Geiger and N. Isgur, *Phys. Rev.* **D55**, 299 (1997).
- [37] L. Hannelius and D.-O. Riska, *Phys. Rev.* **C62**, 045204 (2000); L. Hannelius, D.-O. Riska, and L.-Y. Glozman, *Nucl. Phys.* **A665**, 353 (2000).
- [38] R. L. Jaffe, *Phys. Lett.* B229, 275 (1989).
- [39] H.-W. Hammer, U.-G. Meissner, and D. Drechsel, *Phys. Lett.* B367, 323 (1996).
- [40] U.-G. Meissner *et al.*, preprint hep-ph/9701296.
- [41] M. J. Musolf, H.-W. Hammer, and D. Drechsel, *Phys. Rev.* **D55** 2741 (1997).
- [42] N. W. Park, J. Schechter, and H. Weigel, *Phys. Rev.* D43, 869 (1991).
- [43] S. Hong and B. Park, *Nucl. Phys.* A561, 525 (1993).
- [44] C. V. Christov, *et al.*, *Prog. Part. Nucl. Phys.* 37, 1 (1996).
- [45] S-T. Hong, B-Y. Park, and D-P. Min, preprint nucl-th/9706008.
- [46] S. J. Dong, K. F. Liu, and A. G. Williams, *Phys. Rev. D* **58**, 074504 (1998).
- [47] D. B. Leinweber and A. W. Thomas, *Phys. Rev. D* **62**, 074505 (2000).
- [48] D. B. Leinweber, *et al.*, JLAB-THY-04-8.
- [49] H. Weigel, *et al.*, *Phys. Lett.* B353, 20 (1995).
- [50] D. H. Beck and B. R. Holstein, *Int. J. Mod. Phys.* **E10** 1 (2001).
- [51] S. C. Phatak and Sarira Sahu, *Phys. Lett.* **B321** 11 (1994).
- [52] D. Leinweber, *Phys. Rev.* D53, 5115 (1996).
- [53] M. J. Ramsey-Musolf and H. Ito, *Phys. Rev.* **C55**, 3066 (1997).
- [54] M. J. Musolf, Ph.D. thesis, Princeton University, unpublished.
- [55] I. Zel'dovich, *JETP Lett.* **33**, 1531 (1957).
- [56] W. C. Haxton, E. M. Henley, and M. J. Musolf, *Phys. Rev. Lett.* **63**, 949 (1989); W. Haxton, *Science* **275**, 1753 (1997).
- [57] C. S. Wood *et al.*, *Science* **275**, 1759 (1997).
- [58] S.-L. Zhu, *et al.*, *Phys. Rev.* **D62**, 033008 (2000).
- [59] D.-O. Riska, *Nucl. Phys.* **A678**, 79 (2000).
- [60] C. M. Maekawa and U. van Kolck, *Phys. Lett.* **B478**, 73 (2000).
- [61] C. M. Maekawa, J. S. Viegas, and U. van Kolck, *Phys. Lett.* **B488**, 167 (2000).
- [62] B. A. Mueller *et al.*, *Phys. Rev. Lett.* 78, 3824 (1997).
- [63] B. A. Mueller, Ph.D. thesis, California Institute of Technology, unpublished.
- [64] T. A. Forest, Ph.D. thesis, University of Illinois at Urbana-Champaign, unpublished.
- [65] D. P. Spayde, Ph. D. thesis, University of Maryland, unpublished.
- [66] D. T. Spayde *et al.*, *Phys. Rev. Lett.* **84**, 1106 (2000).
- [67] D. Spayde, *et al.*, *Phys. Lett.* **B58** 79 (2004).

- [68] T. R. Hemmert, U.-G. Meissner, and S. Steininger, Phys. Lett. **B437** 184 (1998).
- [69] MIT-Bates Lab experiment 00-04, T. Ito, spokesperson.
- [70] K.A. Aniol et al. (HAPPEX Collaboration), Phys. Rev. Lett. **82**, 1096 (1999).
- [71] K. A. Aniol, et al. (HAPPEX Collaboration), nucl-ex/00060002.
- [72] F. Maas, *et al.*, submitted to Phys. Rev. Lett. arXiv nucl-ex/0401019.
- [73] Jefferson Lab experiment 99-115, K. Kumar and D. Lhuillier, spokespersons.
- [74] Jefferson Lab experiment 00-003, R. Michaels, P. Souder and R. Urciuoli, spokespersons.
- [75] Jefferson Lab experiment 00-114, D. Armstrong, spokesperson.
- [76] Jefferson Lab experiment 91-004, E. Beise, spokesperson
- [77] Mainz experiment PVA4, D. von Harrach, spokesperson; F. Maas, contact person.
- [78] S. Schramm and C. Horowitz, Phys. Rev. **C49**, 2777 (1994).
- [79] Kuster and Arenhövel, Nucl Phys. **A626**, 911 (1997).
- [80] W.Y.P. Hwang, E.M. Henley, and G.A. Miller, Ann. Phys. **137**, 378 (1981).
- [81] B. Desplanque, J.F. Donoghue, and B.R. Holstein, Ann. Phys. **124**, 449 (1980).
- [82] S. Pollock, Phys. Rev. **D42**, 3010 (1990).
- [83] S. Wells, JLab experiment E04-101.
- [84] N. Mukhopadhyay, *et al.*, Nucl. Phys. **A633**, 481 (1998).
- [85] P. Amore *et al.*, Los Alamos preprint nucl-ex/0007072.
- [86] D. Drechsel, O. Hanstein, S.S. Kamalov and L. Tiator, Nucl. Phys. **A645** (1999) 145.
- [87] L. Tiator and L. E. Wright, Nucl. Phys. **A379** (1982) 407.
- [88] R. Tieulent and J-S. Réal, *Test of a Photoproduction Generator Using the SOS data of December 1999*, G⁰ Technical Report G0-00-019 (July 12, 2000).
- [89] J. L. Matthews and R. O. Owens, Nucl. Instrum. Meth. **111** (1973) 157.
- [90] J. W. Lightbody Jr. and J. S. O'Connell, Computers in Physics. **May/June** (1988) 57.
- [91] R. Tieulent, P. King, A. Lung, J. Martin, M. Pitt, J-S. Réal, J. Roche, Gr. Smith, Gw. Smith, and V. Tadevosyan, *Experimental Background Contributions to the G⁰ Backward Angle Measurements*, G⁰ Technical Report G0-01-012 (April 21, 2001).
- [92] E. Rollinde, *G0GEANT Manual (DRAFT)*, G⁰ Technical Report G0-99-035 (June, 1999).
- [93] S. P. Wells, N. Simicevic, K. Johnston, and T. A. Forest, and The G⁰ Collaboration, *PAC20 Proposal: Measurement of the Parity Violating Asymmetry in the N- $\dot{\gamma}$ DELTA Transition (Originally E97-104)*
- [94] S.P. Wells, G0-99-008, LATECH-CAPS-99-03b (1999).
- [95] C. Murphy, S.P. Wells, and N. Simicevic, G0-99-051, LATECH-CAPS-99-11a (1999).
- [96] G. Quémener and S. Kox, *Aerogel Cherenkov Counter Design for the G0 Spectrometer*, G⁰ Technical Report G0-00-052 (December 13, 2000).

- [97] J. W. Martin, *Aerogel Cherenkov Counter Design*, G⁰ Technical Report G0-00-054 (June 12, 2000).
- [98] D. Higinbotham, Nucl. Instrum. and Meth. **A414** (1998) 332.
- [99] S.-L. Zhu *et al.*, Phys. Rev. Lett. **87** (2001) 201802.
- [100] J. W. Martin, June 2004 G0 internal documents G0-01-043 and G0-04-065.

7 Appendix A: G0 Forward Angle Preprint (nucl-ex/0506021)

Strange Quark Contributions to Parity-Violating Asymmetries in the Forward G0 Electron-Proton Scattering Experiment

D. S. Armstrong,¹ J. Arvieux,² R. Asaturyan,³ T. Averett,¹ S. L. Bailey,¹ G. Batigne,⁴ D. H. Beck,⁵ E. J. Beise,⁶ J. Benesch,⁷ L. Bimbot,² J. Birchall,⁸ A. Biselli,⁹ P. Bosted,⁷ E. Boukobza,^{2,7} H. Breuer,⁶ R. Carlini,⁷ R. Carr,¹⁰ N. Chant,⁶ Y.-C. Chao,⁷ S. Chattopadhyay,⁷ R. Clark,⁹ S. Covrig,¹⁰ A. Cowley,⁶ D. Dale,¹¹ C. Davis,¹² W. Falk,⁸ J. M. Finn,¹ T. Forest,¹³ G. Franklin,⁹ C. Furget,⁴ D. Gaskell,⁷ J. Grames,⁷ K. A. Griffioen,¹ K. Grimm,^{1,4} B. Guillon,⁴ H. Guler,² L. Hannelius,¹⁰ R. Hasty,⁵ A. Hawthorne Allen,¹⁴ T. Horn,⁶ K. Johnston,¹³ M. Jones,⁷ P. Kammel,⁵ R. Kazimi,⁷ P. M. King,^{6,5} A. Kolarkar,¹¹ E. Korkmaz,¹⁵ W. Korsch,¹¹ S. Kox,⁴ J. Kuhn,⁹ J. Lachniet,⁹ L. Lee,⁸ J. Lenoble,² E. Liatard,⁴ J. Liu,⁶ B. Loupias,^{2,7} A. Lung,⁷ G. A. MacLachlan,¹⁶ D. Marchand,² J. W. Martin,^{10,17} K. W. McFarlane,¹⁸ D. W. McKee,¹⁶ R. D. McKeown,¹⁰ F. Merchez,⁴ H. Mkrtchyan,³ B. Moffit,¹ M. Morlet,² I. Nakagawa,¹¹ K. Nakahara,⁵ M. Nakos,¹⁶ R. Neveling,⁵ S. Niccolai,² S. Ong,² S. Page,⁸ V. Papavassiliou,¹⁶ S. F. Pate,¹⁶ S. K. Phillips,¹ M. L. Pitt,¹⁴ M. Poelker,⁷ T. A. Porcelli,^{15,8} G. Quémener,⁴ B. Quinn,⁹ W. D. Ramsay,⁸ A. W. Rauf,⁸ J.-S. Real,⁴ J. Roche,^{7,1} P. Roos,⁶ G. A. Rutledge,⁸ J. Secrest,¹ N. Simicevic,¹³ G. R. Smith,⁷ D. T. Spayde,^{5,19} S. Stepanyan,³ M. Stutzman,⁷ V. Sulkosky,¹ V. Tadevosyan,³ R. Tieulent,⁴ J. van de Wiele,² W. van Oers,⁸ E. Voutier,⁴ W. Vulcan,⁷ G. Warren,⁷ S. P. Wells,¹³ S. E. Williamson,⁵ S. A. Wood,⁷ C. Yan,⁷ J. Yun,¹⁴ and V. Zeps¹¹

(G0 Collaboration)

¹*Department of Physics, College of William and Mary, Williamsburg, VA 23187 USA*

²*Institut de Physique Nucléaire d'Orsay, Université Paris-Sud, F-91406 Orsay Cedex FRANCE*

³*Yerevan Physics Institute, Yerevan 375036 ARMENIA*

⁴*Laboratoire de Physique Subatomique et de Cosmologie, F-38026 Grenoble Cedex FRANCE*

⁵*Loomis Laboratory of Physics, University of Illinois, Urbana, IL 61801 USA*

⁶*Physics Department, University of Maryland, College Park, MD 20472 USA*

⁷*Thomas Jefferson National Accelerator Facility, Newport News, VA 23606 USA*

⁸*Department of Physics, University of Manitoba, Winnipeg, MB R3T 2N2 CANADA*

⁹*Department of Physics, Carnegie Mellon University, Pittsburgh, PA 15213 USA*

¹⁰*Kellogg Radiation Laboratory, California Institute of Technology, Pasadena, CA 91125 USA*

¹¹*Department of Physics and Astronomy, University of Kentucky, Lexington, KY 40506 USA*

¹²*TRIUMF, Vancouver, BC V6T 2A3 CANADA*

¹³*Department of Physics, Louisiana Tech University, Ruston, LA 71272 USA*

¹⁴*Department of Physics, Virginia Tech, Blacksburg, VA 24061 USA*

¹⁵*Department of Physics, University of Northern British Columbia, Prince George, BC V2N 4Z9 CANADA*

¹⁶*Physics Department, New Mexico State University, Las Cruces, NM 88003 USA*

¹⁷*Department of Physics, University of Winnipeg, Winnipeg, MB R3B 2E9 CANADA*

¹⁸*Department of Physics, Hampton University, Hampton, VA 23668 USA*

¹⁹*Department of Physics, Grinnell College, Grinnell, IA 50112 USA*

(Dated: June 17, 2005)

We have measured parity-violating asymmetries in elastic electron-proton scattering over the range of momentum transfers $0.12 \leq Q^2 \leq 1.0 \text{ GeV}^2$. These asymmetries, arising from interference of the electromagnetic and neutral weak interactions, are sensitive to strange quark contributions to the currents of the proton. The measurements were made at JLab using a toroidal spectrometer to detect the recoiling protons from a liquid hydrogen target. The results indicate non-zero, Q^2 dependent, strange quark contributions and provide new information beyond that obtained in previous experiments.

PACS numbers: 11.30.Re, 13.60.-r, 14.20.Dh, 25.30.Bf

At short distance scales, bound systems of quarks have relatively simple properties and QCD is successfully described by perturbation theory. On size scales similar to that of the bound state itself, $\sim 1 \text{ fm}$, however, the QCD coupling constant is large and the effects of the color fields cannot yet be calculated accurately, even in lattice QCD. In addition to valence quarks, e.g., uud for the proton, there is a sea of gluons and $q\bar{q}$ pairs that plays an important role at these distance scales. From

a series of experiments measuring the neutral weak scattering of electrons from protons and neutrons, we can extract the contributions of strange quarks to the ground state charge and magnetization distributions (e.g., magnetic moment) of the nucleon. These strange quark contributions must originate in fluctuations of gluons to $s\bar{s}$ pairs because there are no strange valence quarks in the nucleon. There have been numerous estimates of strange quark contributions to nucleon properties within various

phenomenological models and also in state-of-the-art lattice calculations [1, 2]; many focus on the contribution to the magnetic moment. In this paper, we report on a new measurement sensitive to strange quark contributions over a range of distance scales.

Separation of the strange quark contributions to nucleon currents in the context of the neutral weak interaction dates back to Cahn and Gilman [3] and was developed by Kaplan and Manohar [4]. Because the coupling of both photons and Z bosons to point-like quarks is well defined, it is possible, by comparing the corresponding currents, to separate the contributions of the various flavors [5, 6, 7]. The charge and magnetic form factors of the proton can be written ($i = \gamma, Z$)

$$G_{E,M}^{p,i} = e^{i,u} G_{E,M}^u + e^{i,d} (G_{E,M}^d + G_{E,M}^s), \quad (1)$$

neglecting the very small contribution from heavier flavors. For the ordinary electromagnetic form factors the charges are $e^\gamma = +2/3, -1/3$ for u and d/s quarks, respectively. Assuming that the proton and neutron are re-

lated by a simple exchange of u and d quarks [8] (and the corresponding anti-quarks), the ordinary neutron form factors can be written in terms of these same contributions

$$G_{E,M}^{n,\gamma} = \frac{2}{3} G_{E,M}^d - \frac{1}{3} (G_{E,M}^u + G_{E,M}^s). \quad (2)$$

A complete separation of the $G_{E,M}^q$, and, in particular, isolation of $G_{E,M}^s$, requires a third combination. In this paper, new measurements of the weak interaction form factors of the proton are presented which allow us to determine the strange quark contributions. These form factors are written (Eqn. 1) in terms of the weak charges, $e^Z = 1 - 8/3 \sin^2 \theta_W, -1 + 4/3 \sin^2 \theta_W$ for the u and d/s quarks, respectively, where θ_W is the weak mixing angle.

In order to isolate the small contribution to elastic electron-proton scattering from the neutral weak current, we measure the parity-violating asymmetry for longitudinally polarized (R and L) electrons [7]

$$A = \frac{d\sigma_R - d\sigma_L}{d\sigma_R + d\sigma_L} = -\frac{G_F Q^2}{4\sqrt{2}\pi\alpha} \frac{\varepsilon G_E^\gamma G_E^Z + \tau G_M^\gamma G_M^Z - (1 - 4 \sin^2 \theta_W) \varepsilon' G_M^\gamma G_A^e}{\mathcal{D}} \quad (3)$$

where

$$\tau = \frac{Q^2}{4M_p^2}, \quad \varepsilon = \left(1 + 2(1 + \tau) \tan^2 \frac{\theta}{2}\right)^{-1},$$

$$\mathcal{D} = \varepsilon(G_E^\gamma)^2 + \tau(G_M^\gamma)^2, \quad \text{and } \varepsilon' = \sqrt{\tau(1 + \tau)(1 - \varepsilon^2)},$$

Q^2 is the squared four-momentum transfer ($Q^2 > 0$), G_F and α the usual weak and electromagnetic couplings, M_p the proton mass and θ the laboratory electron scattering angle. The three new form factors in this asymmetry, G_E^Z , G_M^Z and G_A^e may be separated by measuring elastic scattering from the proton at forward and backward angles, and quasi-elastic scattering from the deuteron at backward angles [7].

The G0 experiment [9] was performed in Hall C at Jefferson Lab. We used a 40 μA polarized electron beam with an energy of 3.031 ± 0.001 GeV over the measurement period of 700 h. It was generated with a strained GaAs polarized source [10] with 32 ns pulse timing (rather than the standard 2 ns) to allow for time-of-flight (t.o.f.) measurements. The average beam polarization, measured with a Møller polarimeter [11] in interleaved runs, was $73.7 \pm 1.0\%$. Helicity-correlated current and position changes were corrected with active feedback to levels of about 0.3 parts-per-million (ppm) and 10 nm, respectively. Corrections to the measured asymmetry were applied via linear regression for residual

helicity-correlated beam current, position, angle and energy variations and amounted to a negligible total of 0.02 ppm; the largest correction was 0.01 ppm for helicity-correlated current variation. We made one further correction of, on average, $+0.71 \pm 0.14$ ppm to the asymmetries in all detectors ($\sim 5\%$ variation from detector to detector). It was associated with a small ($\sim 10^{-3}$) fraction of the beam current with a 2 ns structure (“leakage beam”: tails of beams from other operating halls) and a large charge asymmetry (~ 570 ppm); it was measured in otherwise ‘forbidden’ regions of the t.o.f. spectra.

The polarized electrons scattered from a 20 cm liquid hydrogen target [12]; the recoiling elastic protons were detected to allow simultaneous measurement of the wide range of momentum transfer, $0.12 \leq Q^2 \leq 1.0$ GeV². This was effected using a novel toroidal spectrometer designed to measure the entire range with a single field setting and with precision comparable to previous experiments. The spectrometer included an eight-coil superconducting magnet and eight sets of scintillator detectors. Each set consisted of 16 scintillator pairs used in coincidence to cover the range of momentum transfers (smallest detector number corresponding to the lowest momentum transfer). Because of the correlation between the momentum and scattering angle of the elastic protons (higher momentum corresponds to more forward proton scattering angles), detector 15 covered the range of mo-

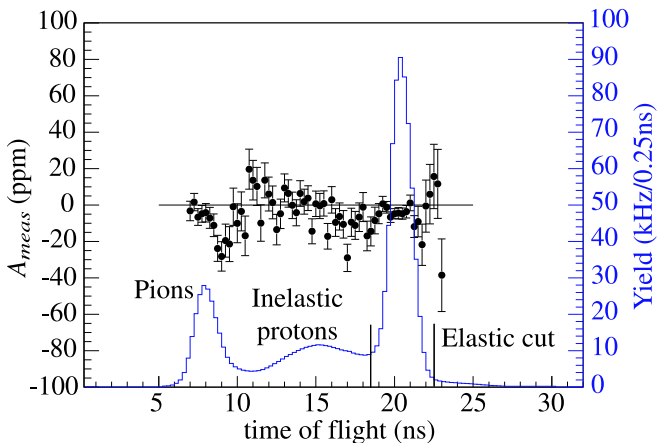


FIG. 1: Example of the raw asymmetry, A_{meas} , (data points) and yield (histogram) as a function of t.o.f. for detector 8.

momentum transfers between 0.44 and 0.88 GeV^2 which we divided into three t.o.f. bins with average momentum transfers of 0.51, 0.63 and 0.79 GeV^2 . For the same reason detector 14 had two elastic peaks separated in t.o.f. with momentum transfers of 0.41 and 1.0 GeV^2 ; detector 16, used to determine backgrounds, had no elastic acceptance. Custom time-encoding electronics sorted detector events by t.o.f.; elastic protons arrived about 20 ns after the passage of the electron bunch through the target (see Fig. 1). The spectrometer field integral and ultimately the Q^2 calibration ($\Delta Q^2/Q^2 = 1\%$) was fine-tuned using the measured t.o.f. difference between pions and elastic protons for each detector. All rates were corrected for dead-times of 10–15% on the basis of the measured yield dependence on beam current; the corresponding uncertainty in the asymmetry is ~ 0.05 ppm. Standard radiative corrections [13] in the range of 1 - 3%, determined by comparing simulations with and without radiation, were also applied to the asymmetries. Lastly, there is an uncertainty of 0.01 ppm due to a small component of transverse polarization in the beam.

As shown in Fig. 1, a background extends on both sides of the elastic proton peak at a t.o.f. ~ 20 ns. This background is essentially all protons (as determined from energy loss measurements in a sampled data set): quasi-elastic protons from the aluminum target windows and inelastic protons from both the hydrogen and the aluminum. The measured asymmetry has two components

$$A_{meas} = (1 - f) A_{el} + f A_{back} \quad (4)$$

where A_{el} is the raw elastic asymmetry and f is the background fraction; in the actual analysis t.o.f. fits to the yield and asymmetry in the region of the elastic peak are used. The yield is typically modeled with a Gaussian elastic peak and a polynomial background. The asymmetry model comprises a quadratic background and a constant for the elastic. For higher numbered detectors

TABLE I: Asymmetries and uncertainties measured in the present experiment [14]. The contributions to the systematic uncertainties are summarized in Table II.

Q^2 (GeV^2)	A_{phys} (ppm)	ΔA_{stat} (ppm)	ΔA_{pt-pt} (ppm)	ΔA_{glob} (ppm)	f	A_{meas} (ppm)
0.122	-1.51	0.44	0.22	0.18	0.061	-1.38
0.128	-0.97	0.41	0.20	0.17	0.084	-1.07
0.136	-1.30	0.42	0.17	0.17	0.085	-1.34
0.144	-2.71	0.43	0.18	0.18	0.077	-2.67
0.153	-2.22	0.43	0.28	0.21	0.096	-2.46
0.164	-2.88	0.43	0.32	0.23	0.100	-3.13
0.177	-3.95	0.43	0.25	0.20	0.110	-4.47
0.192	-3.85	0.48	0.22	0.19	0.110	-5.01
0.210	-4.68	0.47	0.26	0.21	0.116	-5.73
0.232	-5.27	0.51	0.30	0.23	0.136	-6.08
0.262	-5.26	0.52	0.11	0.17	0.154	-5.55
0.299	-7.72	0.60	0.53	0.35	0.174	-5.40
0.344	-8.40	0.68	0.85	0.52	0.182	-3.65
0.410	-10.25	0.67	0.89	0.55	0.180	-1.70
0.511	-16.81	0.89	1.48	1.50	0.190	-5.80
0.631	-19.96	1.11	1.28	1.31	0.20	-9.74
0.788	-30.8	1.9	2.6	2.59	0.40	-12.66
0.997	-37.9	7.2	9.0	0.52	0.78	4.21

TABLE II: Systematic uncertainties for measured asymmetries. The first six uncertainties are global, deadtime is point-to-point and the background is a combination (see text).

Source	Uncertainty
Helicity-correlated beam parameters	0.01 ppm
Leakage beam	0.14 ppm
Beam polarization	1.0%
Ordinary radiative corrections	0.3%
Transverse polarization	0.01 ppm
Q^2	1%
Background correction	0.2 - 9 ppm
Deadtime	0.05 ppm

the background asymmetry is positive. In particular, for detector 15 the background asymmetry has a maximum value of about 45 ppm in the region of the elastic peak. As substantiated by a Monte Carlo simulation, this positive asymmetry is caused by a small number of Λ and Σ weak-decay protons scattered inside the spectrometer magnet. The smooth variation of the region of positive asymmetries is tracked from detectors 12-14 through to detector 16; the background asymmetry for the large acceptance of detector 15 is then corrected by interpolating these measured background asymmetries. As a check, the same fitting procedure described above is also used for detector 15 and gives consistent results.

The elastic asymmetries for the experiment, A_{phys} (A_{el} corrected for all effects described earlier) are presented in Table I. The statistical uncertainties include those from the measured and the background asymmetries. The systematic uncertainties (Table II) are dominated by those from the background correction. This uncertainty is es-

timated from the range of elastic asymmetries generated from a variety of different background yield and asymmetry models. These models are bounded by the measured slopes of background yields and asymmetries on either side of the elastic peak and varied continuously between these limits. The uncertainty in the background asymmetry for detector 15 is conservatively taken to be the difference between interpolated background asymmetries in successive detectors as described above. We have also estimated the global and point-to-point contributions to these uncertainties from the extent to which a change in, e.g., the background asymmetry functional form, consistently changes the asymmetries in all the affected detectors.

The results of the experiment are shown as a function of momentum transfer in Fig. 2. The quantity

$$G_E^s + \eta G_M^s = \frac{4\sqrt{2}\pi\alpha}{G_F Q^2} \frac{\mathcal{D}}{\varepsilon G_E^\gamma} (A_{phys} - A_{NVS}), \quad (5)$$

(where $\eta(Q^2) = \tau G_M^p / \varepsilon G_E^p$) is determined from the difference between the experimental asymmetry and the “no-vector-strange” asymmetry, A_{NVS} . A_{NVS} is calculated from Eqn. 3 with $G_E^s = G_M^s = 0$ for all values of Q^2 , and using the electromagnetic form factors of Kelly [15]. Also shown is the excellent agreement with the HAPPEX measurements [16, 17] made at nearly the same kinematic points (with small corrections to the asymmetries, < 0.2 ppm, to adjust them to the G0 beam energy). The error bars include the statistical uncertainty (inner) and statistical plus point-to-point systematic uncertainties added in quadrature (outer). The error bands represent, for the G0 experiment, the global systematic uncertainties: from the measurement (upper) and from the uncertainties in the quantities entering A_{NVS} (lower). These quantities are: the calculated value of the axial-vector form factor normalization [18] (differing from g_A/g_V by electroweak radiative corrections), the same dipole momentum transfer dependence for $G_A^e(Q^2)$ as is deduced for $G_A(Q^2)$ [19], the axial vector strangeness contribution Δ_s [20], and the electroweak radiative corrections [21]. The sensitivity of the result to electromagnetic form factors is shown separately by the lines on the plot. For the alternative form factor parameterizations of Friedrich and Walcher (FW) [22] (dashed) and the combination (dotted): Arrington “Rosenbluth” [23] - proton, and Kelly [15] - neutron, the effective A_{NVS} is shown (e.g., for the FW parameterization, the value of $G_E^s + \eta G_M^s$ at $Q^2 = 0.63$ GeV² increases from 0.059 to 0.072). Alternately, the uncertainties in the Kelly form factor fits would increase the width of the uncertainty band (lower) for A_{NVS} at each Q^2 by about 25% if included there.

The $G_E^s + \eta G_M^s$ data shown in Fig. 2 have a systematic and intriguing Q^2 dependence. For reference we note that $G_E^s + \eta G_M^s = 0$ at $Q^2 = 0$ and that $\eta \sim 0.94Q^2$ (Kelly form factors) for our kinematics. First, to charac-

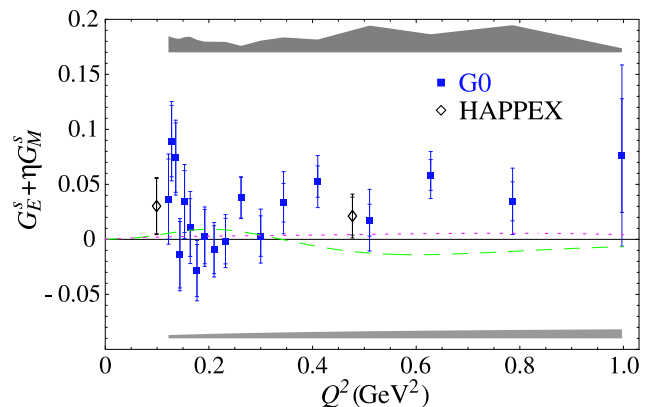


FIG. 2: The combination $G_E^s + \eta G_M^s$ for the present measurement. The gray bands indicate systematic uncertainties (to be added in quadrature); the lines correspond to different electromagnetic nucleon form factor models (see text).

terize our result with a single number, we tested the hypothesis $G_E^s + \eta G_M^s = 0$ by generating randomized data sets with this constraint, distributed according to our statistical and systematic uncertainties (including correlated uncertainties). The fraction of these with χ^2 larger than that of our data set was 11%, so we conclude that the non-strange hypothesis is disfavored with 89% confidence. More important is the Q^2 dependence of the data. The initial rise from zero to about 0.05 is consistent with the finding that $G_M^s(Q^2 = 0.1 \text{ GeV}^2) \sim +0.5$ from the SAMPLE [24], PVA4 [25] and HAPPEX [17] measurements. Because η increases linearly throughout, the apparent decline of the data in the intermediate region up to $Q^2 \sim 0.3$ indicates that G_E^s may be *negative* in this range. There is also some support for this conclusion from the combination of G0 and PVA4 [26] results at $Q^2 = 0.23 \text{ GeV}^2$. There is a significant trend, consistent with HAPPEX [16], to positive values of $G_E^s + \eta G_M^s$ at higher Q^2 . Experiments planned for Jefferson Lab, including G0 measurements at backward angles, and MAMI (Mainz) will provide precise separations of G_E^s and G_M^s over a range of Q^2 to address this situation.

In summary, we have measured forward angle parity-violating asymmetries in elastic electron-proton scattering over a range of momentum transfers from 0.12 to 1.0 GeV². These asymmetries determine the neutral weak interaction analogs of the ordinary charge and magnetization form factors of the proton. From the asymmetries we have determined combinations of the strange quark contributions to these form factors, $G_E^s + \eta G_M^s$, which, together with other experiments, indicate that both G_M^s and G_E^s are non-zero.

We gratefully acknowledge the strong technical contributions to this experiment from many groups: Caltech, Illinois, LPSC-Grenoble, IPN-Orsay, TRIUMF and particularly the Accelerator and Hall C groups at Jefferson Lab. This work is supported in part by CNRS (France),

DOE (U.S.), NSERC (Canada) and NSF (U.S.).

-
- [1] For a recent review, see D. H. Beck and B. R. Holstein, *Int. J. Mod. Phys. E* **10**, 1 (2001).
- [2] See, for example, D. B. Leinweber et al., *Phys. Rev. Lett.* **94**, 212001 (2005).
- [3] R. N. Cahn and F. J. Gilman, *Phys. Rev. D* **17**, 1313 (1978).
- [4] D. Kaplan and A. V. Manohar, *Nucl. Phys.* **B310**, 527 (1988).
- [5] R. D. McKeown, *Phys. Lett. B* **219**, 140 (1989).
- [6] D. H. Beck, *Phys. Rev. D* **39**, 3248 (1989).
- [7] D. H. Beck and R. D. McKeown, *Ann. Rev. Nucl. Sci.* **51**, 189 (2001); K. S. Kumar and P. A. Souder, *Prog. Part. Nucl. Phys.* **45**, S333 (2000).
- [8] G. A. Miller, *Phys. Rev. C* **57**, 1492 (1998).
- [9] P. Roos, *Eur. Phys. J. A* **24**, s2.59 (2005); and in preparation for *Nucl. Instrum. Meth.*
- [10] M. Poelker et al. *AIP Conf. Proc.* **570**, 943 (2001).
- [11] M. Hauger et al., *Nucl. Instrum. Meth. A* **462**, 382 (2001).
- [12] S. Covrig et al., submitted to *Nucl. Instrum. Meth.* (2005), nucl-ex/0502019.
- [13] A. V. Afanasev, I. Akushevich, A. Ilyichev, and N. P. Merenkov, *Phys. Lett. B* **514**, 269 (2001); H. Guler, Thesis, Université Paris-Sud, 2003.
- [14] <http://www.npl.uiuc.edu/exp/G0/Forward>.
- [15] J. J. Kelly, *Phys. Rev. C* **70**, 068202 (2004).
- [16] K. A. Aniol et al. (HAPPEX), *Phys. Rev. C* **69**, 065501 (2004).
- [17] K. A. Aniol et al. (HAPPEX), nucl-ex/0506011; K. A. Aniol et al. (HAPPEX), nucl-ex/0506010.
- [18] S.-L. Zhu, S. J. Puglia, B. R. Holstein, and M. J. Ramsey-Musolf, *Phys. Rev. D* **62**, 033008 (2000).
- [19] V. Bernard, L. Elouadrhiri, and U. G. Meissner, *J. Phys. G* **28**, R1 (2002).
- [20] E. Leader, A. V. Sidorov, and D. B. Stamenov, *Phys. Rev. D* **67**, 074017 (2003).
- [21] M. J. Musolf et al., *Phys. Rept.* **239**, 1 (1994).
- [22] J. Friedrich and T. Walcher, *Eur. Phys. J. A* **17**, 607 (2003).
- [23] J. Arrington, *Phys. Rev. C* **69**, 022201 (2004).
- [24] D. T. Spayde et al. (SAMPLE), *Phys. Lett. B* **583**, 79 (2004).
- [25] F. E. Maas et al. (PVA4), *Phys. Rev. Lett.* **94**, 152001 (2005).
- [26] F. E. Maas et al. (PVA4), *Phys. Rev. Lett.* **93**, 022002 (2004).

8 Appendix B: G0 Forward Angle Run Summary

In this Appendix we present additional details to augment the description of the G0 forward angle measurement in the article submitted to Phys. Rev. Lett. and included as Appendix A above.

The G0 forward angle run took place in the first half of 2004. We accumulated about 101 C of parity-quality beam on target, corresponding to 701 h at the design current of $40\mu A$. This is equivalent to nearly 8×10^7 pulses from which we formed asymmetries in groups of four (“quartets”). Parity-quality beam is defined to be pulses whose beam charge, position, angle, etc. were within 4σ of the beam for the run, where the relevant width is that of the normal distribution for that run (e.g. $\sigma_Q/Q \sim 6 \times 10^{(-4)}$ for typical runs, $\sigma_x \sim 10 \mu m$ for the x beam position).

Helicity-correlated effects in the beam were controlled very well during the measurement; all specifications were achieved (with considerable effort on the part of the Accelerator Division and the collaboration). For the good runs (parity-quality as defined above), the average helicity-correlated beam properties are shown in Table 8.1. Simulation of the

Beam Parameter	Achieved	Spec
Charge asymmetry	-0.14 ± 0.32 ppm	1 ppm
x position differences	3 ± 4 nm	20 nm
y position differences	4 ± 4 nm	20 nm
x angle differences	1 ± 1 nrad	2 nrad
y angle differences	1.5 ± 1 nrad	2 nrad
Energy differences	29 ± 4 eV	75 eV

Table 8.1: Helicity-correlated beam parameter results for the forward angle G0 run. The averages and specs listed are for the entire run.

response of the beam to motions in the x and y directions were consistent with the slopes measured both with small induced motions of the beam and those derived in the linear regression analysis from the natural motion of the beam itself. The total corrections to the data for these helicity-correlated effects totaled a maximum of 0.02 ppm with the largest correction for the charge asymmetry. The leakage beam correction (by measuring the leakage rate and asymmetry in “forbidden” regions of the time-of-flight spectrum) was successfully made on all the data taken with Halls A and B running. The overall correction to the data was $+0.71 \pm 0.14$ ppm. Using the Hall C Møller polarimeter, the beam polarization was measured more than 50 times during the run. The data were corrected for polarization group by group (as various injector and accelerator settings changed); the average polarization was 73.7%.

The target performance during the run was excellent with very little down time due to technical problems. One of the important features of the target is the level of boiling measured to contribute a statistical uncertainty of about 260 ppm to the typical width in a single detector of about 1200 ppm with the standard 2x2 mm beam raster size. The boiling effect was measured with our luminosity detectors situated at scattering angles of 1.2 - 2 degrees and whose widths due to counting statistics were about 170 ppm. The other hardware in the spectrometer, including the magnet, detectors, electronics and DAQ systems all operated satisfactorily at their originally specified levels.

The deadtime of the electronics (10-15%) was measured from the slope of the response of the yield to small induced variations (~ 1000 ppm) in the beam current. This deadtime was accounted for by separate measurements at the discriminator, mean timer and coincidence stages to the level of a few %. The residual effects on the measured asymmetries were accounted for from the slope measurements (see above) and from the linear regression corrections for beam charge. An example of the distribution of asymmetries is shown in Fig. 8.1; after corrections for the deadtime effects, the asymmetry widths agree very well with the measured count rates (Fig. 8.2).

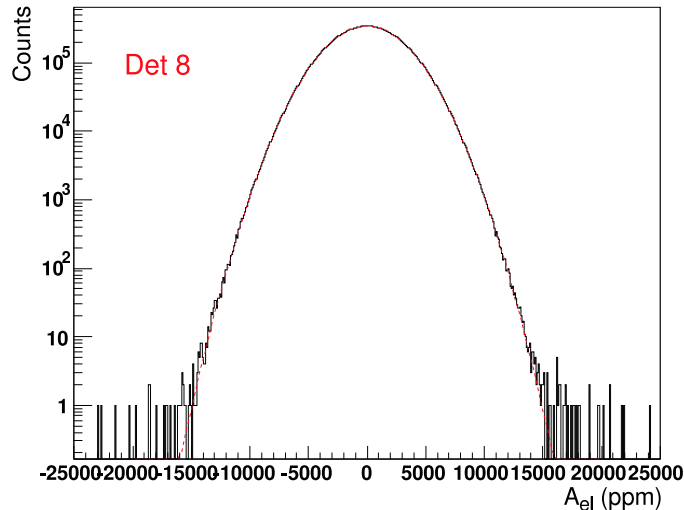


Figure 8.1: Example distribution of elastic asymmetries for detector 8.

We reported asymmetries for each detector in the experiment as follows. For detectors 1-13, corresponding to central Q^2 values of 0.12 to 0.34 GeV^2 we reported a single asymmetry. Because of the correlation between proton recoil momentum and angle (angle decreases as momentum increases) and because of the spectrometer optics, protons corresponding to momentum transfers greater than about 0.45 GeV^2 move back toward lower numbered detectors. In detector 15, the coverage in Q^2 extends from about 0.44 to 0.88 GeV^2 and the time-of-flight (t.o.f.) distribution from about 16.5 to 23 ns. We divided this acceptance into three bins with central Q^2 values of 0.51, 0.63 and 0.79 GeV^2 . Detector 14 had a standard low Q^2 peak (0.41 GeV^2), but also a small peak at $Q^2 = 1.0 \text{ GeV}^2$ which we were also able to analyze. There are, therefore, a total of 18 measurements are reported in the article.

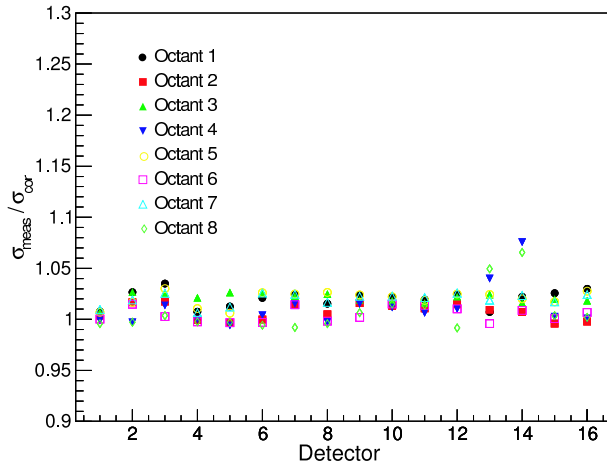


Figure 8.2: Comparison of detector asymmetry widths with those expected from counting statistics.

The data were analyzed after applying a multiplicative blinding factor in the range of 0.75 - 1.25. The background corrections were the most important part of the analysis sequence. Detectors 1-14 and 15 were treated somewhat differently in this regard because of the large Q^2 acceptance of detector 15. On a time-bin-by-time-bin basis we corrected the measured asymmetries according to

$$A_{meas} = (1 - f(t)) A_{el} + f(t) A_{back}. \quad (8.1)$$

The average background dilution factors, f and the background asymmetries are shown in Fig. 8.3. The uncertainties for detectors 1-14 were determined by allowing the background yields and asymmetries to vary continuously over ranges fixed by their magnitudes and slopes outside the region of the elastic yield as shown in Fig. 8.4. The systematic uncertainty in A_{el} was taken to be the average of the dispersions of the ranges of the resulting values A_{el} for the cases where the results were either unweighted or weighted by the χ^2 of the background fits (polynomials as described in the article).

For detector 15 the background yields and asymmetries were determined by interpolating across detectors 12-14 to detector 16 which has no elastic acceptance. The interpolation is effective in part because, particularly in the t.o.f. range below about 18-19 ns, the yields in detectors 12-14 were purely due to inelastic processes. As seen in Fig. 8.3, the background asymmetries became positive in these detectors. Using our standard Geant-based Monte Carlo simulation, we determined that these asymmetries were due to a relatively few protons from Λ and Σ decay that scattered inside the spectrometer and were detected. A comparison of the Monte Carlo results and the measured asymmetries is shown in Fig. 8.5. We did not use this simulation in the analysis (only for the purpose of establishing the source of the positive asymmetries), preferring to use the data itself, interpolated as described above. The yield and asymmetry uncertainties for detector 15 are shown in Fig. 8.6 and amount to \pm “1/2 of one detector” for the yield and “one detector + 0.5 ns” for the

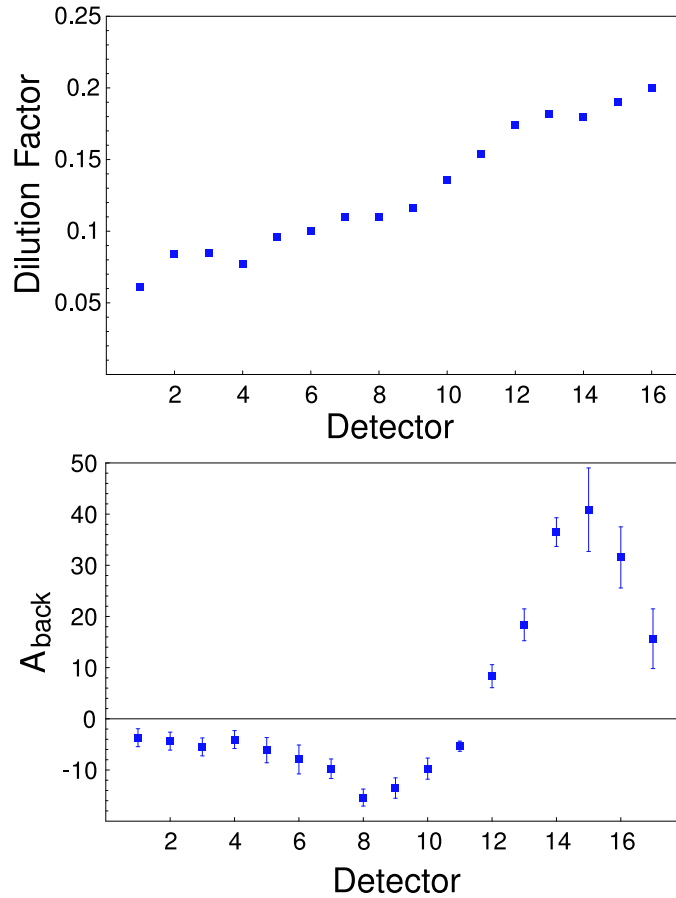


Figure 8.3: Average dilution factors and background asymmetries

asymmetry. For example, the systematic uncertainty for the detector 15 asymmetry extended from the measured detector 14 asymmetry to that measured in detector 16 with an additional component determined by the maximum of the envelope generated when the detector 14 and 16 asymmetries were shifted by ± 0.5 ns. We believe these assessments of systematic uncertainty are conservative.

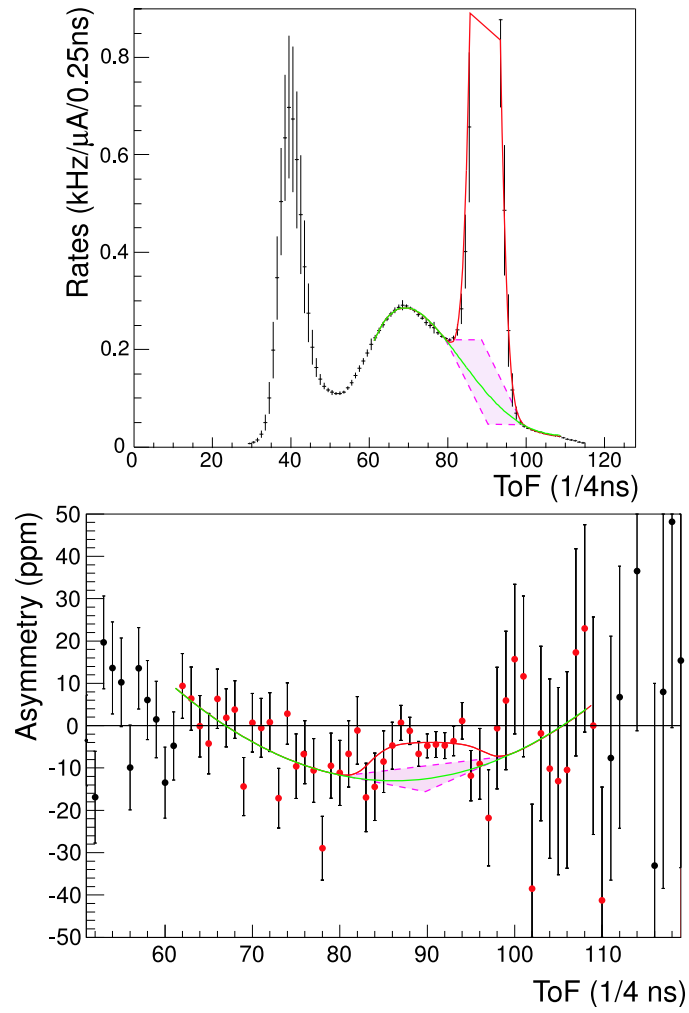


Figure 8.4: Examples of ranges for background fields and asymmetries used to determine systematic uncertainties in A_{el} for detector 1-14.

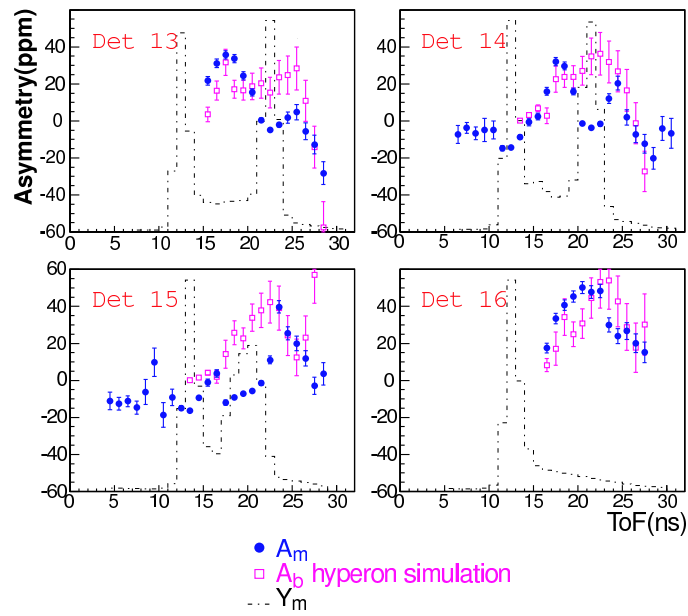


Figure 8.5: Comparison of measured asymmetry and Monte Carlo calculation of background asymmetry. Note that the calculation does not include the elastic asymmetry – this is the reason for the disagreement in the region of the elastic peak.

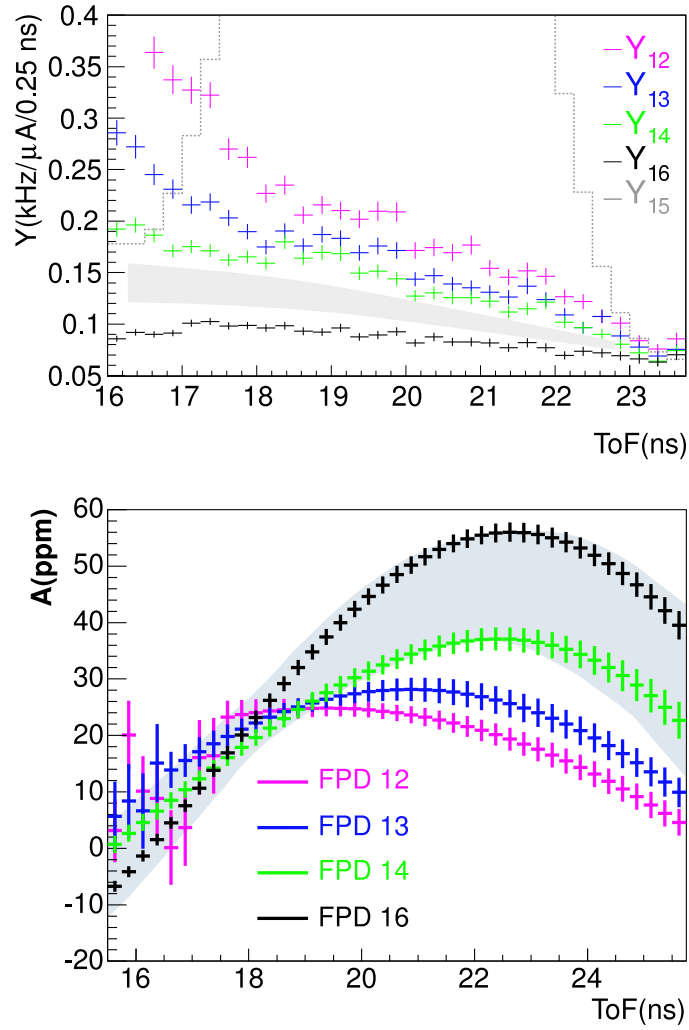


Figure 8.6: Uncertainties assumed for the detector 15 background yield and asymmetry along with the measured data from detectors 12-14 and 16.